e-JSNM

e-JURNAL SAINS NUKLEAR MALAYSIA
e-NUCLEAR SCIENCE JOURNAL OF MALAYSIA

Volume 36 (No.1) 2024
A scientific journal by Malaysian Nuclear Agency
eISSN 2232-0946

eJURNAL
SAINS NUKLEAR MALAYSIA

VOL 36 NO. 1 (2024)
eISSN: 2232-0946

Jurnal Sains Nuklear Malaysia (JSNM, Nuclear Science Journal of Malaysia) is published in the months of June and December annually since 1982 by the Malaysian Nuclear Agency (formerly known as PUSPATI, UTN and MINT). This journal provides a platform for researchers, scientists and engineers (RSEs) to publish their research findings and reviews related to nuclear science and technology so that they can be shared with colleagues throughout the world.

As a means to internationalise JSNM, the Board of Editors welcomes scientific, technical and review articles written by members of the scientific community from home and abroad.

Previously a purely traditional printed journal, JSNM is now adapted and available in electronic form, in keeping with demands and rapid development of ICT. This adaptation also translates to ease of accessibility of JSNM for scientific communities as well as to facilitate knowledge sharing among RSEs.

On behalf of the Editorial Board of JSNM, we would like to acknowledge and thank the authors and referees for their significant contributions to the success of this journal and for embracing this new publication format.

Every effort has been made to trace and acknowledge all copyright holders, but if any have been inadvertently overlooked, the publishers would please to make the necessary arrangements at the first opportunity.

Publishing Office
Malaysian Nuclear Agency, Bangi,
43000 Kajang,
Selangor Darul Ehsan,
MALAYSIA
Tel : +6 03 8911 2000
Fax : +6 03 8911 2154

Website
http://jsnm.nuclearmalaysia.gov.my

TABLE OF CONTENTS

Jurnal Sains Nuklear Malaysia, 2024, 36(No. 1): 1 – 10
ISSN: 2232-0946

THE EFFECT OF PC88A SOLVENT EXTRACTION PARAMETERS AND ITS STRIPPING BEHAVIOR TO THE RECOVERY OF YTTRIUM

Roshasnorlyza Hazan*, Muhammad Haikal Ashraf Ahmad Rosdi, Nuraqilah Sapiee, Khaironie Mohamed Takip, Norhazirah Azhar, Wilfred Paulus and Jacqueline Kones

Materials Technology Group (MTEG), Industrial Technology Division (BTI), Malaysian Nuclear Agency, Bangi, 43000 KAJANG, MALAYSIA
*Correspondence author: roshasnorlyza@nm.gov.my

ABSTRACT

Yttrium (Y) is one of the elements major in heavy rare earth elements (HREE) used in various industries such as metallurgy, steel, laser, electronics, optics, superconductors, magnets, color television (TV) tubes and others applications. In nature, the rare earth elements (REE) are associates in fairly multifaceted combination and because of chemical properties likeness and difficult to isolate REE into single elements. These could be the biggest hurdle in the recovery and extraction of yttrium from xenotime minerals. Therefore, solvent extraction of yttrium from chloride solution using organic extractant 2-ethylhexyl phosphonic acid mono-2-ethylhexyl ester (PC88A) diluted in kerosene and modified with isodecanol was investigated in this study. Based to a solvent extraction study, the best conditions for recovering yttrium using an organic combination consisting of 34% PC88A, 6% isodecanol, and 60% kerosene were 1.0 g of yttrium chloric hexahydrate in 0.2 M hydrochloric acid (HCl) with a ratio organic to aqueous of 1:3 and 30 minutes contact time. Additional research on the behavior of stripping was also differentiated and considered. It was discovered that nitride acid (HNO_3) were more effective in yttrium stripping than HCl and sulfuric acids (H_2SO_4).

Keywords: PC88A, Solvent Extraction, Stripping, Yttrium

INTRODUCTION

Although yttrium was discovered in the late 1800s (Voncken, 2018), it wasn't commercially available until the last few decades (Singh et al., 2015) in the fields of chemistry, physics, computer technology, energy, medicine, and other fields (Grate et al., 2020). Tin-tailing, or xenotime sand, comes from the tin mining sector in peninsular Malaysia, primarily in the state of Perak, Selangor, Pahang and Negeri Sembilan (Meor Sulaiman, M. Y., 2010). This sand contains yttrium. Yttrium is a metal that is very valuable for the advancement of new materials, since yttrium has very unique properties and profitable. To acquire yttrium with high purity, the mineral needs to be purified with few steps of process, namely cracking/digestion of xenotime, leaching, selective precipitation, crystallization, chemical treatment, heat treatment and extraction (Biyantoro et al., 2002).

Solvent extraction is a well-known separation method in which a solute is transported from aqueous phase to another immiscible or partially miscible fluid (solvent) which is in interaction with the initial phase. Basically, there are three solvent extraction stages that is extraction, scrubbing and stripping. In hydrometallurgy, the aqueous phase comprises element of interest to be extract into the organic phase. Solvent extraction is a part of analytical chemistry techniques that able to concentrate elements by an extractant reagent in the organic phase from diluted aqueous solutions. Industrial solvent extraction is a technique that was pioneered by the nuclear industry and utilized for the purification and separation of metals, including plutonium preparation in 1942. Diethylether,

a solvent, and diluted uranyl nitrate were utilized in this extraction process. This was a significant advance in solvent extraction applications, leading the way not just in the nuclear sector but also in the extraction of other elements (Hudson et al., 1982). Currently, solvent extraction is commercially practice for a varied of minerals to obtained valuable elements.

The need of splitting REE from mineral after the cracking or digestion process led to the advancement in solvent extraction with selective complexion. Solvent extraction methods are normally need good extraction kinetics. Regarding its chemical stability, optimum loading and stripping characteristics, low solubility in the aqueous phase, versatility in the extraction of various metal ions, and availability for use in industrial settings. Previously, numerous fundamental researches on the yttrium extraction with di-(2-ethylhexyl) phosphoric acid (D2EHPA) (Biyantoro et al., 2002, Mohammadi et al., 2015, Perwira et al., 2018 and Sapiee et. al., 2019) and Tributyl Phosphate (TBP) (Azhar et al., 2020) have been studied. In 1957, Peppard et al., detailed the use of D2EHPA as a capable extractant for REE. In that study the lanthanides distribution coefficient were showed. D2EHPA as extractant was dependent on the influence of D2EHPA concentration in the equilibrated organic phase, however contradicting to H^+ concentration in the aqueous phase. Additionally, if the solute concentration in the organic phase was too concentrated, a third phase emulsion was forming leading to incomplete extraction process (Anticó et al., 1996). These studies collectively highlight effective methods for high yttrium recovery through solvent extraction processes. Additionally, factors such as extraction time (Nicol et al., 2022), solvent choice based on physicochemical properties and dissolution capabilities (Chandaliya et al., 2012), and operating parameters like agitation rate and settling time (Poole, 2020) significantly impact the yield and quality of the extracted product.

In the extraction process, it was intentionally to separate yttrium from other REE. In order to acquire high yttrium content, thorough study in yttrium extraction and purification from xenotime mineral is necessary. To our knowledge, there hasn't been any published research on the extraction of yttrium using PC88A solvent, despite the fact that there have been several studies on the extraction of REE using various extractants. Therefore, it is essential to define best conditions for yttrium extraction such as of hydrochloride acid concentration, organic to aqueous ratio, contact time, loaded amount of yttrium (III) chloride Hexahydrate (g/l), speed and solvent content. Besides, stripping process parameters (acid suitability, acid concentration, and stripping duration) also been studied in this research.

METHODOLOGY

Experimental

Stock solutions (aqueous) of yttrium chloride were prepared by dissolving the respective yttrium (III) chloride Hexahydrate (99.9%) supplied by Aldrich in diluted HCl (37%, Merck). The organic extractant 2-ethylhexyl phosphonic acid mono-2-ethylhexyl ester (PC88A) (Laurice Labs, Maharashtra, India) was diluted in 30% kerosene (R&M Chemicals) to desire concentration and modify with isodecanol (Laurice Labs, Maharashtra, India). All reagents used were analytical grade. The two stages of the experimental work that were done were solvent extraction and stripping. Solvent extraction experiments were carried out in a glass beaker positioned on a magnetic stirrer plate at room temperature. Mixture of aqueous and organic solvent were vigorously stirred. After 30 minutes, the mixture was transferred into a separatory funnel and waited until a stable, two-layer immiscible solution formed. Then, the aqueous raffinate and extracted organic phase were flushed out into different sample bottle. Different solvent extraction batches were done to study different

extraction parameter such as HCl concentration, organic to aqueous ratio, contact time, loaded amount of yttrium (III) chloride Hexahydrate (g/l), speed, and solvent content.

In stage two, extracted yttrium in organic phase from previously solvent extraction experiment were used for stripping steps. The extracted organic phase was stripped with different molarity of HCl, HNO_3 (65%, R&M Chemicals) and H_2SO_4 (95%, R&M Chemicals) for 30 minutes at room temperature. Then, it was allowed to form two phases: the aqueous phase and the organic phase. Then the best condition for acid concentration was selected to study the effect of stripping duration. Figure 1 shows experimental flow chart.

Characterization

In order to identify the yttrium contained in organic and aqueous solution from solvent extraction and stripping process, the EDXRF Spectroscopy was used to analyse the samples by EDX7000, Shimadzhu. This analytical instrument also able to determine the composition of the elements in the sample solution by measuring the fluorescence intensity converted into yttrium concentration in part per million (ppm).

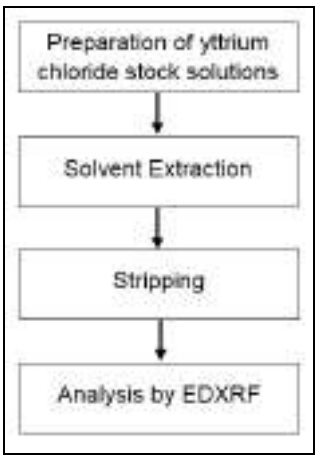

Figure 1. Experimental flow chart

RESULTS AND DISCUSSION

Effect acid molarity on yttrium extraction

HCl with concentration of 0.1 M, 0.2 M, 0.5 M, 1.0 M, 1.5 M and 2.0 M were selected to study the effect the HCl molarity on yttrium extraction and the results were shown in Figure 2. Molarity acid was believed to influence the coefficient distribution, efficiency, and separation factor of yttrium extraction. Higher acid molarity (> 0.2 M HCl) showed a decrease in the percent of yttrium recovery from 80% to 0%. This is due to the PC88A solvent preferring H^+ ion exchange in the low acid molarity of HCI to bind complex organic mixtures to the Y^{3+} ion. Basuki and colleagues also reported that even by increasing acid concentration in solvent extraction process can increase the reactivity of the H^+ ion formation but the extraction could be lowered as high acidity will reduce the ability of solvent (Basuki et al., 2019). The optimum concentration to gain the highest extraction of yttrium was 0.2 M HCl.

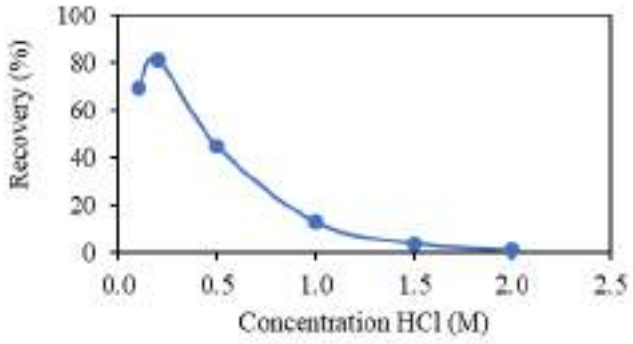

Figure 2. Effect HCl molarity on yttrium extraction.

Effect of solvent amount on yttrium extraction

The solvent amounts of the extraction mixture used to study its effect on the extraction of yttrium under constant conditions were 25%, 33%, 40%, 50%, and 67%. The results are shown in Figure 3. The optimum organic to aqueous ratio to get higher percent recovery of yttrium was 1:3. 25% solvent yielded a high percentage of yttrium extraction, probably because the concentration of H^+ ion in the mixture was higher to enhance the ability of yttrium to form the Y^{3+} ion. Thus, the interaction between the Y^{3+} ion and the PC88A organic ligand will form a complex organic mixture.

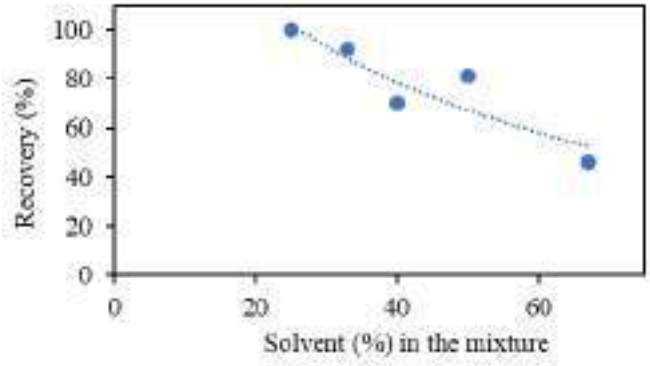

Figure 3. Effect of organic to aqueous ratio to recover yttrium.

Effect of contact time between aqueous and organic phase to extract yttrium

From the data in Figure 4, we can see the effect of the extraction time between the aqueous phase feed and solvent on the distribution of yttrium into the organic phase. The longer the contact between phases during extraction, the higher the concentration of yttrium bound to PC88A. The yttrium solutes extracted into the organic phase will increase by prolonging the stirring duration, which will also increase the mass transfer from the aqueous phase to the organic phase. Thus, the extraction efficiency increases as a result. The amount of yttrium solute extracted will remain constant after attaining the ideal value, and additional stirring time has no further significance. Also, prolong the stirring time will decreased the extraction due to the solvent's optimum ability. However, if the reaction continue for more than 30 minutes, the extraction of yttrium lesser may be due to back-extraction process of yttrium into aqueous phase. Therefore, the optimum separation time to obtain relatively high purity yttrium was obtained at 30 minutes.

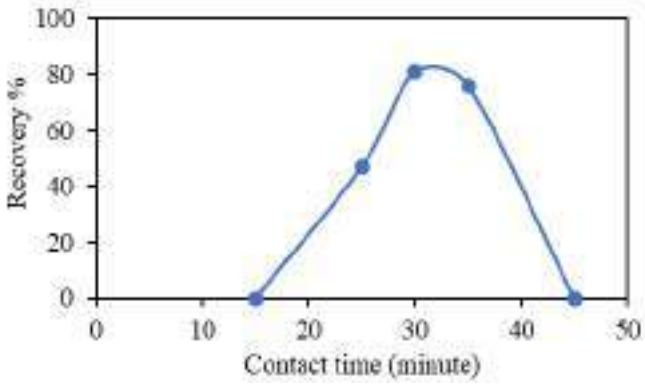

Figure 4. Effect contact time between aqueous and organic phase on yttrium extraction.

Effect of initial Y (III) ion concentration

In order to achieve high efficiency in yttrium extraction, different loads of yttrium (III) chloride hexahydride were introduced to the feed stock solution (aqueous). The yttrium extraction decreased with increasing feed concentration (Figure 5). It is because the organic phase was saturated, which decreased the amount of yttrium that diffused into the organic phase. This finding was in line with Basuki et al.'s (2020). From the data below (Figure 5), 0.3 g yttrium (III) chloride hexahydride in 25 ml solution or 12 g/L is the optimum value to get higher percent recovery of yttrium. A high concentration of yttrium in an aqueous solution would hinder the extraction of yttrium because it's surrounded and encapsulated by organic solvent. Thus, the organic solvent could not hold the Y^{3+} ion and developed an emulsion. Therefore it can be said that the separation of the solute (yttrium) is relative to their solubility in the two phases (Li, et al., 2021).

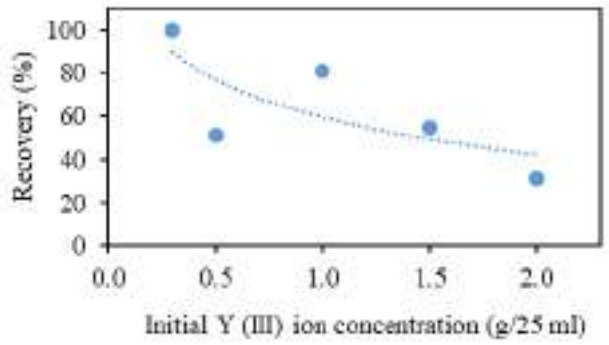

Figure 5. Effect of loaded organic amount in the pregnant solution.

Effect of stirring speed on yttrium extraction

From the data shown in Figure 6, the extraction of yttrium can only be done after vigorously stirring the mixture. However, the Y^{3+} ion extraction was reduced as the stirring speed was too high and the mixture tends to produce a third-layer phase, or emulsion. This phenomenon should prevail in order to extract most of the desired element of interest. Also, high stirring rates would produce excessive turbulence and air bubbles which could affect extraction precision. Hence, stirring speed of 6 units on scale is the optimum value to get higher percent recovery of yttrium.

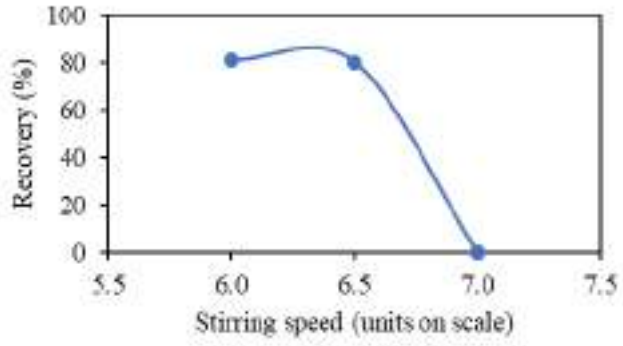

Figure 6. Effect of stirring speed on yttrium extraction

Effect of different compossition PC88A and Isodecanol in solvent mixture on yttrium extraction

From Figure 7, the effect of extractant PC88A concentration and isodecanol in kerosene as an extraction factor in yttrium extraction. PC88A was used as extractant to pull out the REE in aquoeus solution (in this case yttrium). Where as isodecanol was used as modifier in solvent extraction process to prevent the formation of third phase while during solvent extraction process. The result of the effect isodecanol content in yttrium extraction is shown in Figure 8. From the experiment, it was noticed that 35% PC88A and 6% isodecanol diluted in kerosene were the optimum compositions to extract yttrium from the aquoeus phase.

Effect of acid concentration on yttrium stripping

The organic phase extracted from a 0.2 M HCl aqueous solution was used for the stripping process. Different concentrations of H_2SO_4, HNO_3, and HCl were studied. From the data in Table 1, the recovery of yttrium is very low (just 1.7%) upon 4 M H_2SO_4 stripping. As per record, stripping with higher than 4 M H_2SO_4, the emulsion tends to exist thus affect the stripping results. The emulsion occurs when 3 phases were exist in the solution. Therefore, H_2SO_4 is not suitable for yttrium stripping process.

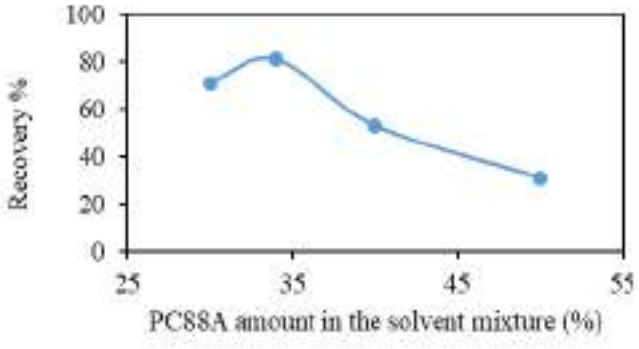

Figure 7. Effect of solvent different composition (PC88A) on yttrium extraction

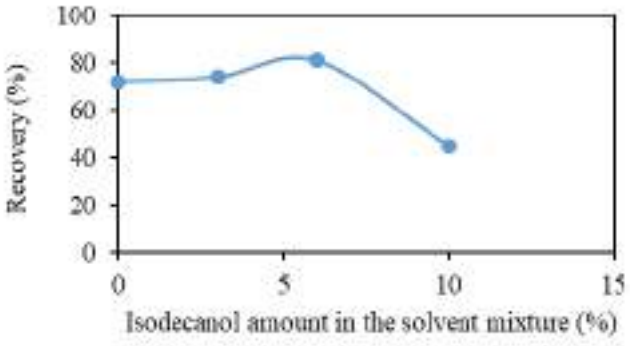

Figure 8. Effect of different composition Isodecanol in the organic mixture to extract yttrium

Table 1. Effect of H_2SO_4 molarity on yttrium stripping from organic mixture

Concentration of H_2SO_4 (M)	Yttrium recovery (%)
0.5	0.0
1.0	0.0
2.0	0.0
3.0	0.0
4.0	1.7

Figure 9 shows the effect of acid (HCl and HNO_3) concentration on yttrium stripping. From the graph, HNO_3 with concentration of 2 M was the optimum concentration to get high recovery of yttrium. The stripping efficiency start to decrease at 5 M because it is hard to break down the complex mixture organic solvent that form from extraction process. 2 M HNO_3 was capable to break down the bonding between Y^{3+} and organic complex and its ability to capture and thus pull yttrium from the organic extractant. In this research, H_2SO_4 and HCl have low efficiency to strip yttrium from organic phase and it can be conclude that the best stripping agents were HNO_3> HCI> H_2SO_4 accordingly.

Effect of stripping duration to recover yttrium

Figure 10 showed the effect of stripping duration on yttrium into the aqueous phase. The longer the contact time between phases during extraction, the higher the concentration of yttrium bound to NO^{3-} . However, if the reaction prolong more than 45 minutes, the recovery become less showing that the yttrium reverse back to organic phase.

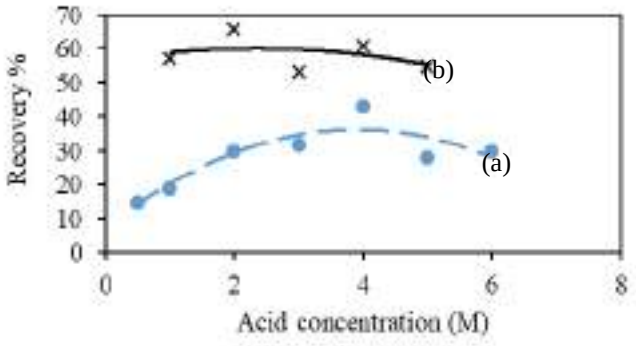

Figure 9. Effect acid concentration (a) HCl and (b) HNO_3 on yttrium stripping

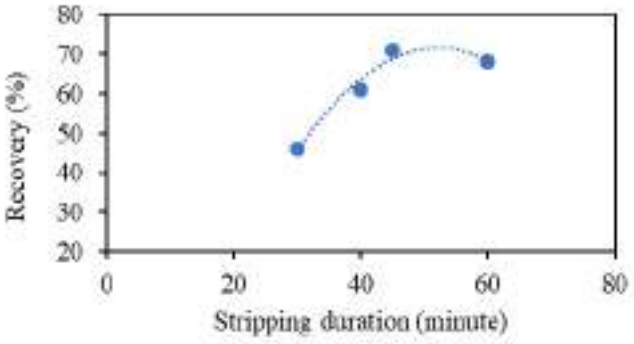

Figure 10. Effect of stripping duration using HNO_3 to strip yttrium.

In order to minimise the error during experiment, it is recommend to properly weighed the yttrium (III) chloride hexahydrate and ensure the cleanliness of all the apparatus used to measure the samples as it will affect the concentration of the sample during acid dilution. Also, noted to use same magnetic stirring plate and stir bar size for all experiments for results reliability.

CONCLUSIONS

Solvent extraction of yttrium from yttrium (III) chloride hexahydrate using extractant PC88A in kerosene was obtained in this study. It was found that the optimum condition to extract yttrium was 0.2 M HCl with a 30-minute contact time. Whereas 12 g/L of loaded yttrium (III) chloride hexahydrate in 34% PC88A and 6% isodecanol as a modifier in kerosene were used as solvents to extract the Y^{3+} ion. Complete extraction of yttrium was achieved from the 25% solvent phase contained in the extraction mixture. In addition, in the stripping study, it is suggested that yttrium stripping was preferred to occur with 2 M HNO_3 as the stripping agent for 45 minutes of contact time.

ACKNOWLEDGEMENTS

The authors really appreciate the supported from Agensi Nuklear Malaysia through Projek R&D Dana Dalaman Nuklear Malaysia (NM-R&D-20-29) and (NM-R&D-20-48).

REFERENCES

Anticó, E.Masana, A.Hidalgo, M.Salvadó, V.Iglesias, M.Valiente, M. (1996). Solvent extraction of yttrium from chloride media by di (2- ethylhexyl) phosphoric acid in kerosene. *Speciation Studies and Gel Formation* 267-276.

Azhar, N., Mohamed Takip, K., Hazan, R., Paulus, W. S., Sapiee, N. A. and Kones, J. (2020). Solvent Extraction of Thorium from Malaysian Xenotime using Tributyl Phosphate (TBP), *IOP Conference Proceeding Series: Materials Science and Engineering* 785; 012015.

Basuki, K. T., Arifudin, R., Pusparini, W. R. and Saputra, A. (2019). Dysprosium (Dy) Separation from Yttrium Concentrate in Nitric Acid Solution Using Aliquat 336 Solvent, *Key Engineering Materials* 840; 573-579.

Basuki, K. T., Rohmaniyyah, A., Pusparini, W. R. and Saputra, A. (2020). Extraction Development for the Separation of Gadolinium from Yttrium and Dysprosium Concentrate in Nitric Acid using Cyanex 572, *International Journal of Technology* 11(3); 450-460.

Biyantoro, D., Subagiono, R. and Soemarsono, M. (2002). Pemurnian Itrium Dengan Cara Ekstraksi, Prosiding Pertemuan and Presentasi Ilmiah Penelitian Dasar Ilmu Pengetahuan dan Teknologi Nuklir P3TM-BATAN, Jogyakarta, *ISSN 0216-3128*.

Chandaliya, V. K., Banerjee, P. K. and Biswas, P. (2012). Optimization of Solvent Extraction Process Parameters of Indian Coal, *Mineral Processing and Extractive Metallurgy Review* 33; 246-259.

Grate, J. W., O'Hara, M. J. and Egorov, O. B. (2020). Automated radiochemical separation, analysis, and sensing, in: L'Annunziata, M. (eds), Handbook of Radioactivity Analysis: Volume 2, *Radioanalytical Applications*, pg. 821-872.

Hudson, M. J. (1982). An introduction to some aspects of solvent extraction chemistry in hydrometallurgy, *Hydrometallurgy* 9:149-168.

Li, Z., Dewulf, B. and Binnemans, K. (2021). Nonaqueous Solvent Extraction for Enhanced Metal Separations: Concept, Systems, and Mechanisms, *Industrial & Engineering Chemistry Research* 60; 17285-17302.

Meor Sulaiman, M. Y. (2010). Recovery of Uranium from Malaysian Non-Conventional Sources, *Journal of Nuclear and Related Technologies* 7; 55-65.

Mohammadi, M., Forsberg, K., Kloo, L., De La Cruz, J. M. and Rasmuson, A. (2015). Separation of ND(III), DY(III) and Y(III) by Solvent Extraction using D2EHPA and EHEHPA, *Hydrometallurgy* 156; 215-224.

Nicol, M., Welham, N. and Senanayake, G. (2022). Solvent extraction, *Hydrometallurgy Practice* 2; 117-170.

Perwira, N.I., Basuki, K. T., Biyantoro, D. and Effendy, N. (2018). Optimization Recovery of Yttrium Oxide in Precipitation, Extraction and Stripping Process, *IOP Conference Proceeding Series: Materials Science and Engineering* 349; 012044.

Poole, C. F. (2020). Solvent Selection for Liquid-Phase Extraction, in: *Handbooks in Separation Science, Liquid-Phase Extraction*, 45-89.

Sapiee, N. A., Mohamed Takip, K., Hazan, R., Zahari, A. K and Paulus, W. (2019). Extraction of Thorium from Malaysian Xenotime for Preparation of Nuclear Grade Thorium, *AIP Conference Proceeding* 2068.

Singh, L. K., Srinivasan, A., Pillai, U. T. S., Joseph, M. A. and Pai, B. C. (2015). The Effect of Yttrium Addition on the Microstructure and Mechanical Properties of Mg Alloys, *Trans. Indian Inst. Met.* 68:331–339.

Tickner, Ben J.Stasiuk, Graeme J.Duckett, Simon B. Angelovski, G. (2020). The use of yttrium in medical imaging and therapy: Historical background and future perspectives, *Chemical Society Reviews* 49: 6169--6185

Voncken, J.H.L. (2018). Yttrium. In: White, W.M. (eds) Encyclopedia of Geochemistry. *Encyclopedia of Earth Sciences Series. Springer, Cham*., pg 1518.

Jurnal Sains Nuklear Malaysia, 2024, 36(No.1): 11 – 18
ISSN: 2232-0946

CALIBRATION OF THERMOLUMINESCENCE OPTICALLY STIMULATED LUMINESCENCE READER USING QUARTZ IN DATING LABORATORY, MALAYSIAN NUCLEAR AGENCY

Mohd Zuhair Mohd Sanusi*, Nooradilah Abdullah, Norfaizal Mohamed, Salahuddin Muhammad, Mohamad Noh Sawon, Mohd Tarmizi Ishak, Muhammad Izzat Muamar Ramli, Nur Rahizatul Atiqah Norhisam and Siti Noor Hayani Mohd Noor

Radiochemistry and Environmental Laboratory, Malaysian Nuclear Agency,
*Correspondence author: zuhair@nm.gov.my

ABSTRACT

The TL OSL reader is a tool for dating applications in a variety of fields. One of the main components of an TL OSL reader is the irradiation source. Calibration of irradiation sources for readers can be carried out using quartz. It is important to calibrate the reader before performing the dating method to ensure equivalent dose (De) within the acceptance range. Quartz was measured using the Single Aliquot Regeneration (SAR) protocol. Measurements obtained an average dose rate of 28.87 ± 0.43 Gy (n = 10) with a ratio in the range <5%. In addition, the measurement also found that the value of 2θ is equivalent to 70%. The central point for dose distribution was at 28.30 Gy, with only 3 quartz samples getting dose readings outside the dispersion bar. The overdispersion measured doses were 26.62, 27.68 and 31.56 Gy. The ratio of received dose/measured dose is in the range of 0.887-1.052, which showed that there was no significant signal loss. Therefore, we conclude that this reader is acceptable for carrying out the dating method and it is recommended to use different doses as well as more detailed SAR protocols for further study.

Keywords: thermoluminescence, optically stimulated luminescence, quartz, calibration

INTRODUCTION

A Thermoluminescence Optically Stimulated Luminescence (TL OSL) reader is a tool to carry out the dating method based on the luminescence signal in sample minerals such as quartz or feldspar (Preusser et al., 2008). Studies using this reader are concentrated in many fields such as archaeology (Afouxenidis et al., 2007), geochronology (Sanderson & Murphy, 2010) and geomorphology (Muñoz-Salinas et al., 2011). One of the important components in the reader is the irradiation source. It is used to provide homogeneous irradiation in ensuring detection and stimulation on a wide range for dating methods (Richter et al., 2013). Calibration of the irradiation source for the reader was performed using quartz that had been exposed to known radiation.

Quartz is one of the minerals found in nature that can be used in the dating method which aims to identify its properties on radiation and annealing (Koul et al., 2016). The quartz is an aliquot that contains natural paleodoses which can receive laboratory-made dose radiation that has a known dose strength (Kadereit & Kreutzer, 2013). Calibration using quartz is an important step to ensure that the equivalent dose (*De*) values obtained are reliable, accurate and unbiased (Guérin & Valladas, 2014). Through the use of this quartz, the reader provides information regarding the equivalent dose of this

reference material. This equivalent dose is obtained by comparing the luminescence signal that responds to the radiation dose and the luminescence signal that responds to different irradiation times by using the radiation source to be calibrated (Richter et al., 2020). Therefore, this study aims to calibrate the radiation source of the TL OSL reader by using quartz that has been validated to ensure that the equivalent dose is within the accepted range before performing the dating method

MATERIALS, METHODS AND EXPERIMENTAL SETTING

We have received approximately 5 grams of quartz (a verified reference material) that has been prepared according to a study by (Richter et al., 2020) for which sediment samples were taken from the Holocene desert in Schletau, Germany.

Coarse grains (100–300 µm) of the sediment were extracted and heated at 500ºC for 5 hours to zeroing the luminescence signal on the sample. Thereafter, the samples were treated with 30% HCl to remove carbonates. Then, the samples were treated using 30% H_2O_2 to remove organic matter. For the purpose of quartz enrichment, the samples undergo a process using a heavy liquid mineral separation with sodium polytungstate at densities of 2.62 and 2.67
gcm^{-3}. Etching was performed using 40% HF and washing in 30% HCl and then washed in a dispersion material to dissolve the fine-grain particles attached. The dried samples were then sieved at grain sizes between 90–160 µm. Thereafter, the sample was exposed to a daylight lamp (OSRAM Ultra Vitalux 300W with cooling) for 8 hours.

The quartz received had an equivalent dose of 30 Gy, similar to the quartz in study (Richter et al., 2020). The next procedure is carried out in a dark room aimed at preventing the quartz from being exposed to daylight which could cause zeroing of the luminescence signal on the sample (Osunkwor & DeWitt, 2021). The grains of the quartz were placed in 10 stainless steel discs measuring 10 mm in diameter that had been put with silicon oil. After that, all the discs are placed on sample wheels to be loaded into the reader.

Measurements were carried out using the LEXSYG SMART System from Freiberg Instruments (Richter et al., 2015). The reader was equipped with a Sr-90 beta radiation with a radioactivity of 1.85 GBq. Use of blue LED (458 nm) for the purpose of optical stimulation with a maximum rate of 100 mW/cm^{-2}. The detection window used is a combination of BSL/TL, which includes 2.5 mm thick Hoya U340, 5 mm thick BP 365/50 and Schott NG4. Thermal stimulation is carried out through a metal ceramic plate capable of reaching a maximum of 700 ºC to allow the sample to be heated accurately and can be repeated in a homogeneous (Lomax et al., 2014).

Calibration using quartz in this study is based on Single Aliquot Regeneration (SAR) protocol (Murray & Wintle, 2000), whose setting can be seen in TABLE 1. All aliquots (n = 10) undergo a complete SAR protocol cycle for each quartz. The beta irradiation time is framed based on the irradiation time capable of inducing the OSL signal and is carried out in a dark room to ensure that all aliquots have the same bleaching history (Guérin & Valladas, 2014). In this study, 10 s was the test dose. Therefore, each increase in the irradiation time of 50, 100 and 150 s should be followed by 10 s of irradiation. The main purpose of each aliquot obtaining the test dose was to ensure the consistency of the measurements at the beginning and end of the study. In this protocol, preheat is carried out after irradiation and before OSL measurements to allow the transfer of electrons from the trapped (Frouin

et al., 2017). An overview of the SAR cycle for this study is shown in FIGURE 1. Each aliquot was preheated at 200 ºC for 10 s while heating at 160ºC. The OSL signal for the blue signal stimulus was stimulated for 50 s at a temperature of 125 ºC.

TABLE 1 shows the SAR protocol cycle settings for each quartz sample. The experimental dose is 10 s, where each increase in irradiation dose 50, 100 and 150 s will be followed with 10 s to ensure consistency of irradiation.

Setting	Temperature (ºC)	Time (s)
Irradiation	-	10, 50, 100, 150
Test	-	10
Preheat	200	10
Preheat	160	0
OSL	125	50

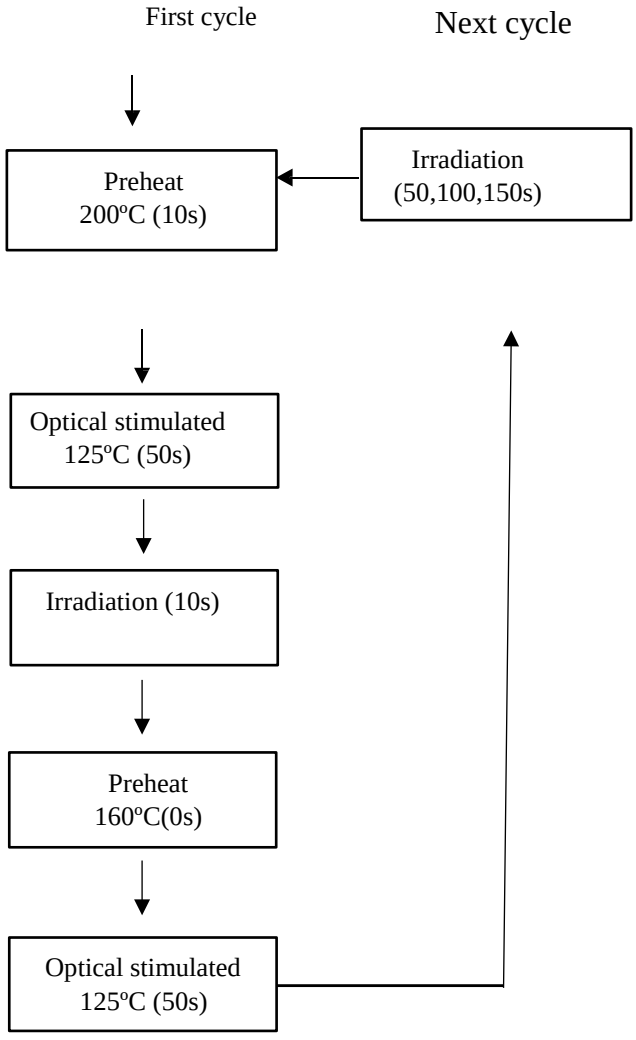

FIG 1 shows an overview of the SAR cycle for each sample. The cycle includes preheating, optic stimulation and irradiation.

RESULTS AND DISCUSSION

The results of the luminescence signal for quartz samples are shown in TABLE 2. According to studies conducted by (Richter et al., 2020), the most accurate and simple calibration using OSL can be obtained by interpolating the OLS-Beta normalisation response from gamma dose quartz to a single dose growth curve beta arising from the OSL-Beta normalisation response at several beta doses. The interpolation of the normalised signal OSL is conducted with three or more points using square linear fit (Guérin & Valladas, 2014). Therefore, we applied this interpolation to each quartz. An example of interpolation can be seen as the curve in FIGURE 2.

The mean of the interpolated dose was 28.87 ± 0.43 Gy (n = 10), as in FIGURE 3, using the SAR procedure. The ratio of dose is consistent and unity in the range of 5%. This leads to an assumption that the SAR protocol and the stability of the reader guarantee the signal obtained during this study (Tribolo et al., 2019). In addition, the standard deviation for all quartz samples (n=10) was approximately 4%. This gives the impression that there is no significant change in the optically stimulated luminescence signal produced by the reader experiencing uncertainty (fluctuation) either in the short or long term (Hansen et al., 2015). Furthermore, the use of the SAR protocol should reach a unity value, but a range within ± 10% is acceptable in the application of the dating method (Richter et al., 2020).

The central point for the dose distribution was at 28.30 Gy, as in FIGURE 4 obtained via the abanico plot (Dietze et al., 2016). The value of 2θ is equivalent to 70%, which indicates only 3 quartz samples got dose readings located outside the dispersion bar as marked in a grey area in FIGURE 4. The three overdispersion equivalent doses were 26.62, 27.68 and 31.56 Gy. These three doses are acceptable because they are still in the range of ± 10%. Meanwhile, 10 samples were insufficient to produce a useful abanico plot curve for the study (Dietze et al., 2016). Thus, the curve is only to give a conclusion in general without considering the polarity as similar to the study conducted by (Douglass et al., 2006).

TABLE 2 shows the results of luminescence signals for 10 quartz samples.

Quartz Sample, n	Given dose, Gy	Measured dose, Gy	Measured dose/Given dose	Error
1	30	27.97±0.57	0.932	0.33
2	30	31.56±0.63	1.052	0.42
3	30	28.85±0.75	0.962	0.6
4	30	28.69±0.63	0.956	0.6
5	30	28.6±1.02	0.953	0.75
6	30	29.24±0.81	0.975	0.8
7	30	29.85±0.64	0.995	0.72
8	30	29.67±0.58	0.989	0.66
9	30	27.68±0.41	0.923	0.73
10	30	26.62±0.40	0.887	0.53

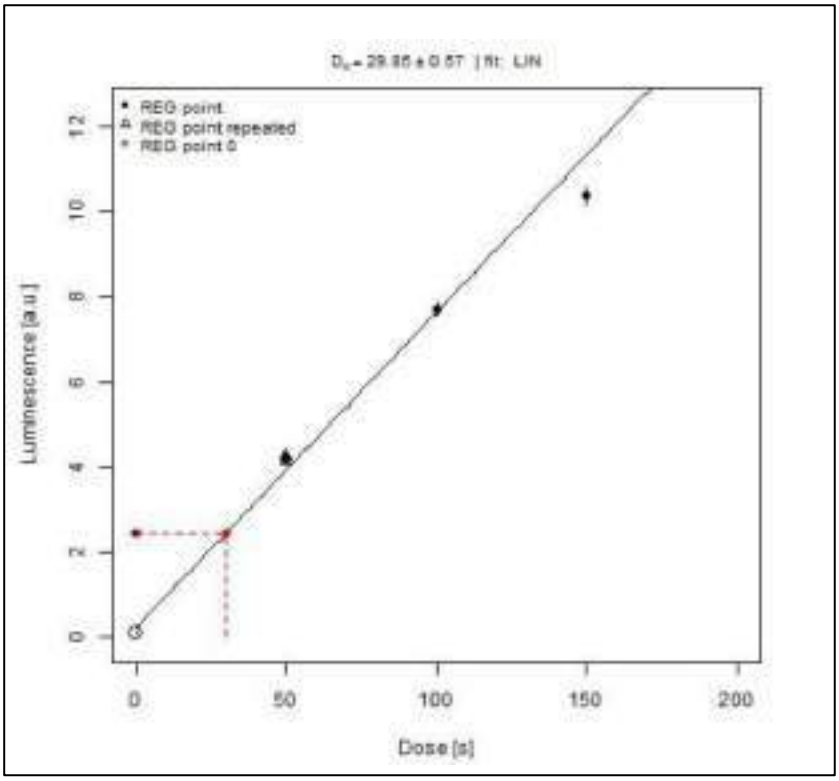

FIG 2 shows an example of interpolation of the dose growth curve that obtains an equivalent dose of 29.85 Gy. The interpolation of the normalised signal OSL is conducted using square linear fit at points 50,100,150 Gy.

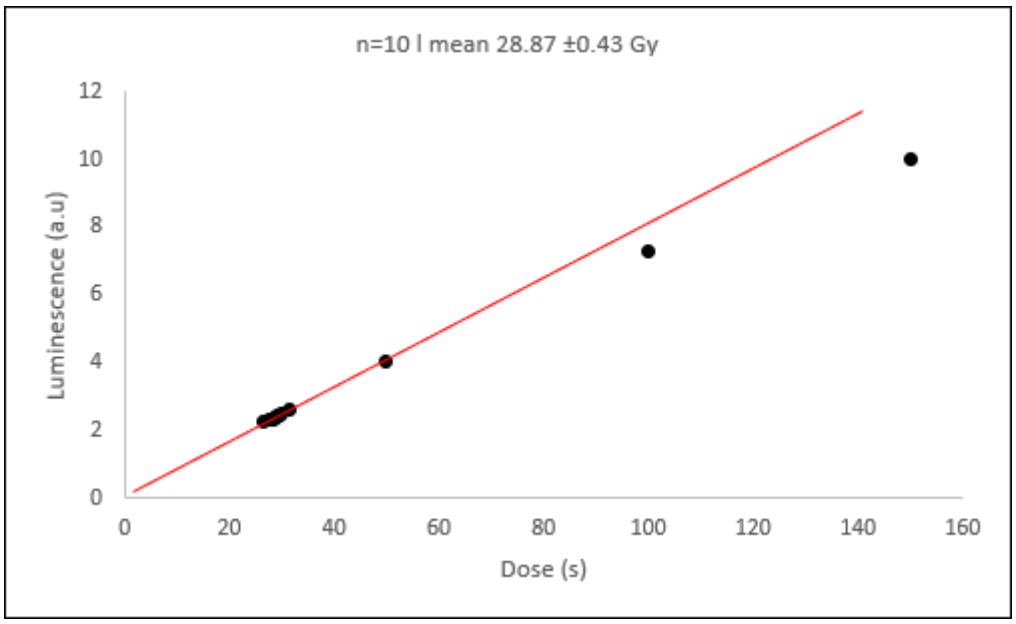

FIG 3 shows the average interpolation dose for all 10 quartz samples was 28.87 ± 0.43 Gy using the SAR protocol.

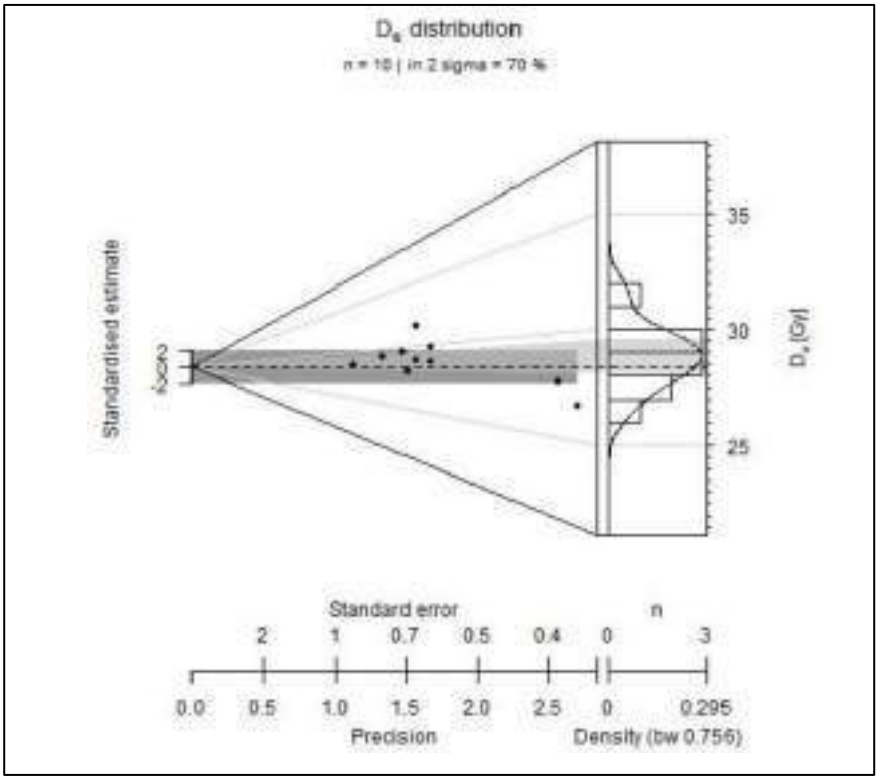

FIG 4 is an abanico plot showing the central point of the dose distribution at 28.30 Gy and value of 2θ equivalent to 70%. The overdispersion doses are 26.62, 27.68 and 31.56 Gy.

CONCLUSION

The TL OSL readers is a tool for dating applications in various fields. The approach of using quartz for the calibration of radiation sources for TL OSL readers is an alternative approach. It is an important step to understand all forms of variability and accuracy for equivalent dose readings. The mean measured dose in this study was average 28.87 ± 0.43 Gy with a ratio in the range <5% using SAR protocol. Abanico plot shows that the central point of dose distribution is 28.30 Gy, with a 2 θ value equal to 70%. It is indicating that 7 quartz sample readings lie on under dispersion region. Quartz samples were measured and produced a ratio measured dose/given dose between 0.887-1.052, which showed that there was no significant signal loss and was almost in line with the results of the study conducted by (Richter et al., 2020) whose ratio between 0.992 - 1.017. Therefore, we concluded the equivalent dose reading produced by the reader in this study was acceptable because it was within range. Indeed, the use of quartz for the calibration of TL OSL readers in the Dating Laboratory, Malaysian Nuclear Agency is to ensure the reliability and accuracy of the dose equivalent reading before using it for the dating method of any sample. Thus, further studies can be performed using a variety of quartz and more detailed SAR protocols such as the study (Hansen et al., 2015).

ACKNOWLEDGEMENT

The authors are highly appreciative and thankful to the Malaysian Nuclear Agency for granting the budget to purchase this TL OSL reader in order to upgrade from the previous TL reader. Thanks also to all project and laboratory members for their constant assistant throughout the period of work. Lastly, the authors are highly indebted to our top management for their constant support and encouragement in each and every stage of the manuscript preparation.

REFERENCES

Afouxenidis, D., Stefanaki, E. C., Polymeris, G. S., Sakalis, A., Tsirliganis, N. C., & Kitis, G. (2007). TL/OSL properties of natural schist for archaeological dating and retrospective dosimetry. *Nuclear Instruments and Methods in Physics Research Section A: Accelerators, Spectrometers, Detectors and Associated Equipment*, *580*(1), 705-709.

Dietze, M., Kreutzer, S., Burow, C., Fuchs, M. C., Fischer, M., & Schmidt, C. (2016). The abanico plot: Visualising chronometric data with individual standard errors. *Quaternary Geochronology*, *31*, 12-18.

Douglass, D. C., Singer, B. S., Kaplan, M. R., Mickelson, D. M., & Caffee, M. W. (2006). Cosmogenic nuclide surface exposure dating of boulders on last-glacial and late-glacial moraines, Lago Buenos Aires, Argentina: Interpretive strategies and paleoclimate implications. *Quaternary Geochronology*, *1*(1), 43-58.

Frouin, M., Huot, S., Kreutzer, S., Lahaye, C., Lamothe, M., Philippe, A., & Mercier, N. (2017). An improved radiofluorescence single-aliquot regenerative dose protocol for K-feldspars. *Quaternary Geochronology*, *38*, 13-24.

Guérin, G., & Valladas, H. (2014). Cross-calibration between beta and gamma sources using quartz OSL: Consequences of the use of the SAR protocol in optical dating. *Radiation Measurements*, *68*, 31-37.

Hansen, V., Murray, A., Buylaert, J.-P., Yeo, E.-Y., & Thomsen, K. (2015). A new irradiated quartz for beta source calibration. *Radiation Measurements*, *81*, 123-127.

Kadereit, A., & Kreutzer, S. (2013). Risø calibration quartz – A challenge for β-source calibration. An applied study with relevance for luminescence dating. *Measurement*, *46*(7), 2238-2250.

Koul, D. K., Polymeris, G. S., Soni, A., & Kulkarni, M. S. (2016). Impact of firing on the OSL luminescence properties of natural quartz: A case study. *Nuclear Instruments and Methods in Physics Research Section B: Beam Interactions with Materials and Atoms*, *370*, 86-93.

Lomax, J., Kreutzer, S., & Fuchs, M. (2014). Performance tests using the Lexsyg luminescence reader. *Geochronometria*, *41*(4), 327-333.

Muñoz-Salinas, E., Bishop, P., Sanderson, D. C., & Zamorano, J.-J. (2011). Interpreting luminescence data from a portable OSL reader: three case studies in fluvial settings. *Earth Surface Processes and Landforms*, *36*(5), 651-660.

Murray, A. S., & Wintle, A. G. (2000). Luminescence dating of quartz using an improved single- aliquot regenerative-dose protocol. *Radiation Measurements*, *32*(1), 57-73.

Osunkwor, E., & DeWitt, R. (2021). Beta dose rate reduction for the built-in 90 Sr/90 Y sources of Risø TL/OSL automated readers. *Ancient TL*, *39*(2), 18-27.

Preusser, F., Degering, D., Fuchs, M., Hilgers, A., Kadereit, A., Klasen, N., Krbetschek, M., Richter, D., & Spencer, J. (2008). Luminescence dating: Basics, methods and applications. *E&G Quaternary Science Journal*, *57*, 95-149.

Richter, D., Richter, A., & Dornich, K. (2013). Lexsyg — A new system for luminescence research. *Geochronometria*, *40*(4), 220-228.

Richter, D., Richter, A., & Dornich, K. (2015). Lexsyg smart - A luminescence detection system for dosimetry, material research and dating application. *Geochronometria*, *42*, 202-209.

Richter, D., Woda, C., & Dornich, K. (2020). A new quartz for? -transfer calibration of radiation sources. *Geochronometria*, *47*(1), 23-34.

Sanderson, D. C. W., & Murphy, S. (2010). Using simple portable OSL measurements and laboratory characterisation to help understand complex and heterogeneous sediment sequences for luminescence dating. *Quaternary Geochronology*, *5*(2), 299-305.

Tribolo, C., Kreutzer, S., & Mercier, N. (2019). How reliable are our beta-source calibrations? *Ancient TL, 37(1),* 1-10.

Jurnal Sains Nuklear Malaysia, 2024, 36(No. 1): 19 – 30
ISSN: 2232-0946

DETERMINATION OF ELEMENT CONTENTS IN COMMERCIAL TEAS MARKETED IN MALAYSIA & ITS INFUSION RESIDUE USING NEUTRON ACTIVATION ANALYSIS (NAA)

Siti Aminah Omar*, Nazaratul Ashifa Abdullah Salim, Md Suhaimi Elias and Zalina Laili

Analytical Chemistry Application Group (ACA)
Department of Waste Technology & Environmental (BAS)
Malaysian Nuclear Agency, 43000 Kajang, Selangor
*Correspondence author: sitiaminah@nm.gov.my

ABSTRACT

Fifteen elements in black tea, rose flavoured tea and fruit tea commercially sold in Malaysian market were determined using neutron activation analysis (NAA). The elements analyzed include Al, Ba, Br, Ce, Cl, Eu, Fe, K, La, Mg, Mn, Na, Rb, Sc, and Zn. The concentration of these elements varied according to the tea types in the range of 2.2% K to 0.04 mg/kg Sc. The quality of analysis was assured using certified standard reference material. Infusion study of the tea residue was also performed to analyse the possible consumption of these elements by the population. Ce, Cl, Eu, K and Rb were found to be easily infused in all three types of teas. Kruskal-Wallis test found significant differences ($p < 0.05$) between elemental composition and types of teas. Principal component analysis (PCA) showed clustering based on types of teas.

Keywords: infusion, elemental, neutron activation analysis, principal component analysis, tea

INTRODUCTION

Tea (*Camellia sinensis*) is a very popular beverage in the world due to its pleasant aroma and refreshing taste (Zhao et al., 2017a). Many cultures around the world have their own practice of drinking tea which relates to its customs and rituals (Martin, 2011). Moreover, drinking tea is associated with its therapeutic and beneficial anti-inflammatory and antioxidant properties (Peluso & Serafini, 2017). There are several types of tea available in the market which can be categorized by the fermentation level. Black tea is fully fermented, green tea is unfermented while oolong tea is partially fermented (Lin et al., 1996). In Malaysia, tea plantation area covers 2271 hectares which is predominantly cultivated in Pahang and Sabah. It is estimated that 7523 tons of tea products come from that area (Jabatan Pertanian Semenanjung Malaysia, 2022). Many of these tea products are sold as loose powder or in bags. Black tea is widely consumed in Malaysia, apart from green tea and flavoured tea.

Tea contains proteins, amino acids, lipids, sugars, vitamins, fiber and minerals (Ramdani et al., 2013; Lim et al., 2021). The availability of minerals in tea leaves varies depending on the origin of tea, tea variety, geochemistry of the soil and the use of pesticides and fertilisers (Lagad et al., 2011; Islam & Ebihara, 2017; Lim et al., 2021). Tea is known to contain essential minerals such as manganese. Manganese is known to be involved in many physiological functions of the human body such as the metabolism of glucose and lipids as well as aids in protection against metabolic diseases such as obesity and diabetes mellitus (Li & Yang, 2018). Nonetheless, the consumption of minerals upon drinking teas is related to the solubility of the elements and the infusion times taken.

Due to the health benefits offered by drinking tea, various studies have been carried out to study the elemental compositions of tea as well as its infusion. Many of this elemental analysis of tea was done using spectroscopic techniques such as inductively coupled plasma mass spectrometry (Han et al., 2014), atomic absorption spectrometry (Brzezicha-Cirocka et al., 2016) and X-ray fluorescence spectroscopy (Lim et al., 2021). The use of neutron activation analysis (NAA) for elemental characterization of food products including tea has been growing increasingly in recent years (Chajduk, 2009; Zhang et al., 2011; Lagad et al., 2011; Mahani & Maragheh, 2011; Jonah & Williams, 2000; Islam & Ebihara, 2017). NAA is an analytical instrument capable of analysing various elements simultaneously with high precision and accuracy. As a non-destructive technique, it also offers other advantages such as much simpler preparation, does not require complex chemical digestion and therefore free of contamination from acid digestion.

This study aims to investigate the concentration of multi-element in tea leaves sold in Malaysian market using NAA and its leaching efficiency upon brewing. Statistical and classification technique are also used to find the relationship between elemental profile and type of teas.

MATERIALS AND METHODS

10 different tea samples in loose form and tea bags were purchased from local markets around Bangi, Selangor. The characteristics of tea samples used in this study are summarized in Table 1. The origin of the tea samples was determined solely from the packaging. The procedure described by Islam & Ebihara (2017) was followed for the preparation of the samples for elemental concentration determination. Each sample was dried in the oven at 50^{o}C overnight and then ground to a small size using a household blender.

Table 1 Characteristics of analysed teas

Tea samples	Type of Tea	Origin	Confection
BT 1	Black tea	Ranau, Malaysia	Bags
BT 2	Black tea	Indefinite origin	Bags
BT 3	Black tea	Cameron, Malaysia	Loose
BT 4	Black tea	Cameron, Malaysia	Bags
RT 1	Rose flavoured tea	Malaysia	Loose
RT 2	Rose flavoured tea	Indefinite origin	Loose
FT 1	Fruit tea	East Africa	Bags
FT 2	Fruit tea	East Africa	Bags
FT 3	Fruit tea	East Africa	Bags
FT 4	Fruit tea	East Africa	Bags

Irradiation and counting

Samples were transferred into a polyethylene tube and heat-sealed. The weight of the samples used varies according to the intended radionuclides. For short-lived radionuclides approximately 0.07g of samples were weighed in, while for long-lived radionuclides, around 0.1g of samples were used. Samples and standard reference materials (SRMs) were co-irradiated in the same batch performed at the TRIGA Mark II reactor at Malaysian Nuclear Agency with thermal neutron flux approximately at $6.8 \times 10^{12} n \cdot cm^{-2} s^{-1}$. For short-lived radionuclides (Al, Cl, K, Mg, Mn, Na) samples and standard reference materials were irradiated for 1 minute using a pneumatic transfer system followed by

cooling (decay period) for 8 minutes and then counted for 5 minutes using HPGe Gamma Spectrometer (EG&ORTEC, USA) and GammaVission software. As for long-lived radionuclides (Ba, Br, Ce, Eu, Fe, La, Rb, Sc, Zn) samples were irradiated for 4 hours followed by cooling (decay period) for 3 days for first counting and 21 days for second counting. Samples were then counted for 1 hour each. Standard reference material from the National Institute of Standards and Technology (NIST) 1515-Apple Leaves was chosen as quality control materials due to its similarity in matrix as tea leaves. The concentration of the tea samples as well as the SRM was calculated using Eq. (1) (Joel et al., 2018; Elias et al., 2018):

$$C_{EL} = \frac{A_{smp}}{A_{std}} \times \frac{W_{std}}{W_{smp}} \times C_{std} \quad (1)$$

Where
A_{smp} = net count of the selected peak area of an interested element in a sample
A_{std} = net count of the selected peak area of an interested element in a standard
W_{smp} = Weight of sample used (g)
W_{std} = Weight of standard used (g)
C_{std} = Concentration of interested element in standard (mg/kg)
C_{EL} = Concentration of interested element in sample (mg/kg)

As for the infusion study, the following method by Islam & Ebihara (2017) is used. Around 2.0g of tea samples were infused in 200 ml boiling DI water for 6 minutes and then filtered. The residual tea leaves were then collected and underwent the same procedure as the non-infused tea leaves.

Statistical Analysis

Statistical analysis was performed using PAST3 (Hammer, Harper, & Ryan, 2001) software. Normality test was done using the Shapiro-Wilk test followed by a non-parametric test as the data appeared to be a non-normal distribution. Kruskal-Wallis test was performed to find a significant difference followed by Dunn's post-hoc test. Principal component analysis (PCA) was also employed for the visualisation purpose.

RESULT & DISCUSSION

Quality of analysis

The quality of the data obtained was evaluated by measuring the elemental contents of standard reference material NIST 1515 Apple Leaves which act as the quality control material in this study. The energies of the gamma-ray used, mean concentration results, recovery percentage, percentage of RSD and *Z*-score are given in Table 2. This method shows good accuracy with a relatively high recovery percentage ranging between 89% to 118%. The obtained results were in good agreement with the certified values. Majority of the data shows high precision with %RSD < 10% except for K and Fe with slightly higher %RSD at 10.25 and 11.20% respectively. All of the data are within the 95% confidence limit as suggested by the *Z*-score below 3 (Lagad et al., 2011).

Table 2 Analytical results of elemental contents of the standard reference material NIST 1515 Apple Leaves

Element	Energy (keV)	Certified value (mg/kg)	This work (mg/kg)	Recovery (%)	%RSD	*Z*-Score
Al	1779	284.5 ± 5.8	278.8 ± 15	96.6	5.46	0.61
Ba	496	48.8 ± 2.3	46.3 ± 1.3	94.8	2.78	0.96
Br	554	(1.8)	1.70 ± 0.07	94.3	4.41	-
Ce	145	(3)	3.01 ± 0.25	100.3	8.33	-
Cl	2168	582 ± 15	567 ± 28	97.4	5.00	0.46
Eu	1408	(0.2)	0.23 ± 0.003	112.5	1.35	-
Fe	1099	82.7 ± 2.6	85.4 ± 9.7	103.3	11.20	-0.27
K	1524	16080 ± 210	15125 ± 155	94.1	10.25	0.61
La	1596	(20)	18.61 ± 1.59	93.0	8.57	-
Mg	1014	2710 ± 120	2965 ± 204	109.4	6.90	-1.08
Mn	1811	54.1 ± 1.1	56.2 ± 4.0	103.9	7.05	-0.51
Na	2754	24.4 ± 2.1	22.0 ± 1.3	89.9	6.02	0.99
Rb	1077	10.2 ± 1.6	9.2 ± 0.35	90.4	3.80	0.60
Sc	889	(0.03)	0.03 ± 0.001	101.7	0.21	-
Zn	1116	12.45 ± 0.43	14.74 ± 0.91	118.4	6.19	-2.27

Concentrations are mentioned as mean ± SD
Values given in parentheses ( ) are information values
Z-score = $\frac{x-\mu}{\sigma}$ where x = observed mean value, μ = certified value and σ = standard deviation of certified value

Elemental composition of tea leaves

The analytical result of the elemental contents in tea samples is shown in Table 3. A total of 15 elements can be determined from this analysis. Generally, K, Mg, Al, Mn, Cl, and Fe are the primary elements that can be found in tea leaves. Black tea leaves from Ranau, Sabah have the most abundant amount of K (20873 mg/kg) as compared with the other Malaysian-grown black tea leaves. High concentration of K in tea leaves sold in other Asian countries was also reported (Lagad et al., 2011; Huang et al., 2016; Lim et al., 2021). Comparison of elemental levels in tea leaves from various origins is shown in Table 4. Mg concentration is the highest in black tea leaves (3030 – 3572 mg/kg). It is twofold higher than Mg concentration in black tea leaves from selected region in China (Ma et al., 2019). Interestingly, high concentration of Al is observed in all tea samples at around 1224 - 1932 mg/kg. Alzheimer's disease (AD) is reportedly linked to over-exposure to heavy metals such as aluminium (Deng et al., 2000; de Oliveira et al., 2018). Being a popular drink worldwide, tea is known as a major dietary source of Al, hence, heavy consumption of tea might increase risk of the disease. Mn concentration reported here is between 460 – 1748 mg/kg with fruit teas has considerably higher Mn content than black teas and rose flavoured teas. The average Mn concentration of tea leaves in this study is considerably higher than Mn concentration of European black tea and green tea (8 – 709 mg/kg) (Girolametti et al., 2023). Cl concentration is relatively high in all tea samples (653 – 1175 mg/kg). The value reported here is slightly higher than Cl concentration of tea leaves sold in Nigeria (Jonah & Williams, 2000) but relatively similar to black tea leaves sold in Poland (Chajduk, 2009) as well as Japanese green tea leaves (Islam & Ebihara, 2017) (Table 4). Fe concentration is between 126 – 290 mg/kg. Generally, fruit tea has the highest concentration of Fe among the tea samples.

Table 3 Elemental concentration of tea samples sold in Malaysian market (mg/kg)

Element	BT 1	BT 2	BT 3	BT 4	RT 1	RT 2	FT 1	FT 2	FT 3	FT 4
Al	1690 ± 33	1444 ± 134	1684 ± 85	1809 ± 6	1932± 130	1589 ± 44	1328 ± 42	1365 ± 18	1224 ± 27	1371 ± 47
Ba	105 ± 12.8	42.2 ± 2.9	53.9 ± 0.9	30.7 ± 1.8	88.3 ± 1.9	78.3 ± 6.6	47.7 ± 6.4	29.9 ± 3.7	43.1 ± 0.5	42.8 ± 0.8
Br	2.82 ± 0.20	4.37 ± 0.15	2.49 ± 0.02	3.11 ± 0.08	2.38 ± 0.07	2.42 ± 0.01	5.43 ± 0.43	4.93 ± 0.10	4.68 ± 0.13	4.61 ± 0.03
Ce	0.29 ± 0.05	0.19 ± 0.24	0.13 ± 0.17	0.11 ± 0.15	0.27 ± 0.09	0.17 ± 0.06	0.40 ± 0.51	0.39 ± 0.05	0.39 ± 0.01	0.42 ± 0.05
Cl	1075 ± 16.7	761 ± 35.5	954 ± 55.1	1047± 18.1	1175 ± 7.0	1013 ± 76.9	857 ± 115	860 ± 13.8	728 ± 7.4	653 ± 8.6
Eu	0.07 ± 0.008	0.06 ± 0.001	0.06 ± 0.009	0.04 ± 0.004	0.06 ± 0.001	0.07 ± 0.002	0.09 ± 0.04	0.06 ± 0.009	0.07 ± 0.002	0.07 ± 0.006
Fe	126 ± 0.7	243 ± 16.5	132 ± 5.1	224 ± 26.8	290 ± 8.7	190 ± 8.0	233 ± 13.7	267 ± 12.7	242 ± 2.7	223 ± 35.2
K	20828 ± 366	20090 ± 767	16513 ± 248	17458 ± 222	13569 ± 535	22331 ± 242	20750 ± 222	22001 ± 86	20873 ± 84	19865 ± 474
La	0.67 ± 0.06	1.24 ± 0.05	0.49 ± 0.05	0.28 ± 0.05	0.77 ± 0.18	0.54 ± 0.08	1.56 ± 0.01	1.72 ± 0.02	1.51 ± 0.01	1.74 ± 0.03
Mg	3176 ± 328	3572 ± 816	3030 ± 707	3326 ± 292	3037 ± 304	2718 ± 204	2877 ± 764	2392 ± 392	3353 ± 514	2885 ± 650
Mn	1133 ± 12.5	1570 ± 90.9	553 ± 18.4	460 ± 23.8	903 ± 54.9	951 ± 33.5	1644 ± 63.6	1748 ± 48.0	1574 ± 9.4	1694 ± 25.8
Na	22.2 ± 0.74	35.24 ± 3.07	21.41 ± 1.05	34.75 ± 0.73	36.55 ± 1.96	35.12 ± 2.52	52.65 ± 0.56	61.06 ± 3.85	49.58 ± 1.66	52.56 ± 6.47
Rb	107 ± 0.9	122 ± 3.2	62.5± 3.0	57.3 ± 1.2	66.9 ± 0.8	81.5 ± 5.6	101 ± 0.2	99.6 ± 1.5	95.4 ± 1.8	101 ± 4.0
Sc	0.05 ± 0.002	0.07 ± 0.001	0.05 ± 0.005	0.05 ± 0.002	0.08 ± 0.01	0.05 ± 0.001	0.04 ± 0.004	0.04 ± 0.001	0.04 ± 0.002	0.04 ± 0.001
Zn	25.77 ± 2.49	25.92 ± 1.62	26.65 ± 2.93	37.27 ± 4.02	32.20 ± 7.96	25.25 ± 3.61	20.36 ± 0.86	20.33 ± 1.30	21.43 ± 0.97	19.76 ± 0.36

Table 4 Comparison of concentration value of elements in tea leaves from various origins

Origin	Iran	India	China	China	Europe	China	Nigeria	Japan	Poland	This study
Type of tea	Black tea	Black tea	Various	Puerh, green & black tea	Black & green tea	Various	Black tea	Green tea	Black tea	Black, fruit & rose flavoured tea
Al (mg/kg)			1397 – 1553	116 - 862	733 – 4865	217 – 607	47.8 – 1904	304 – 1100	622 – 1053	1224 – 1932
Ba (mg/kg)		11.9 - 144	3.1 – 3.4			14.7 – 37.9			10.4 – 33.4	29.9 – 105
Br (mg/kg)	4.20 – 7.07	0.9 – 1.3						2.78 – 4.44	2.02 – 9.81	2.38 – 5.43
Ce (mg/kg)		0.12 – 0.69							386 – 580	0.11 – 0.42
Cl (mg/kg)							422 – 921	560 - 1110	739 – 934	653 – 1175
Eu (mg/kg)									7.0 – 18.5	0.04 – 0.07
Fe (mg/kg)		71 – 397	114 – 150		77 – 99			57.8 – 105	82.8 – 207	126 – 290
K (wt. %)	1.20 – 2.10	0.98 – 1.96	1.56 – 1.57				1.54 – 2.08	1.54 – 2.19	1.87 – 2.17	1.36 – 2.23
La (mg/kg)		0.06 – 0.42						0.05 – 0.41	0.16 – 0.56	0.28 – 1.74
Mg (wt. %)			0.22 – 0.26	0.12 – 0.23		1.93 – 2.86	0.23 – 1.24	0.18 – 0.28	0.19 – 0.21	0.24 – 0.36
Mn (mg/kg)	150 – 500	163 - 1191	629 – 845	386 – 780	8 – 709		286 – 801	528 – 965	444 – 787	460 – 1748
Na (mg/kg)	18 – 120	11.9 – 95.2				252 – 551	15.1 – 492	5.16 – 53.6	30.8 – 93.8	21.4 – 61.1
Rb (mg/kg)		19.8 – 90.4	26.6 – 62.9			3.1 – 25.7		13.2 – 24.7	39.1 – 144	57.3 – 122
Sc (mg/kg)		0.01 – 0.02		0.04 – 0.24				0.004 – 0.02	0.05 – 0.08	0.04 – 0.08
Zn (mg/kg)		17.6 – 92.9	23.8 – 27.7	33.8 – 95.9	21.9 – 39.7			14.7 – 26.4	29.3 – 31.4	19.8 – 37.3
References	Mahani & Maragheh, 2011	Lagad et al., 2011	Lim et al., 2021	Ma et al., 2019	Girolamett i et al., 2023	Zhao et al., 2017b	Jonah & Williams, 2000	Islam & Ebihara, 2017	Chajduk, 2009	

Some elements in tea samples can be categorized as microelements which includes Ba, Na, Rb and Zn (19.76 – 122 mg/kg). Rose flavoured tea has a relatively higher concentration of Ba than black tea and fruit tea. Black tea from Ranau has the highest concentration of Ba in this study. Na concentration in fruit tea is higher than black tea and rose flavoured tea. The concentration of Na reported here is very much less than Na concentration of multiple varieties of tea leaves from China analysed over different seasons (Zhao et al., 2017b) (Table 4). Rb concentration is between 57.3 – 122 mg/kg. Fruit tea has considerably higher content of Rb than other types of teas. Zn concentration is between 19.76 – 37.27 mg/kg. It is lower compared to black tea from China (33.8 – 95.9) (Ma et al., 2019) but quite similar with black tea in Poland (20.7 – 37.3 mg/kg) (Polechońska et al., 2015). Some elements in tea leaves were present in trace amounts. These include Br, Ce, Eu, La and Sc (0.04 – 5.43 mg/kg). As for Br, its concentration in black tea is almost similar to rose flavoured tea but lower than fruit tea. The concentration of Br is higher than those reported of black tea leaves of Indian origin (Lagad et al., 2011) but quite similar to tea leaves sold in Iranian market (Mahani & Maragheh, 2011) (Table 4). As for the lanthanides, the concentration is roughly in the following order: La>Ce>Eu=Sc. Fruit tea has the highest concentration of the lanthanides followed by rose flavoured tea and black tea.

Multi-element analysis of infusion tea leaves residue

The extraction efficiencies of the elements by infusion were also evaluated to assess the potential consumption of elements studied from drinking the tea. In order to show a better representation of the leaching efficiencies of the tea samples, they were separated based on types of teas; black tea, rose flavoured tea and fruit tea and their mean extraction efficiencies are compared. Figure 1 below shows the extraction efficiencies of the tea leaves among the three types of teas. Extraction efficiencies are calculated as the ratio between infusion residue and its corresponding tea leaves.

According to Matsuura et al., (2001), extraction efficiencies of tea leaves can be categorized into three groups: highly extractable (>55%), moderately extractable (20 – 55%), and poorly extractable (<20%). Figure 1 indicates that elements Ce, Cl, Eu, K and Rb are easily leached from tea leaves upon brewing in all three types of teas whereas some elements are poorly leached which include Al, Mn and Zn. Highly extractable element is highly ionic as suggested by Islam & Ebihara (2017). Thus, it is expected that the amounts of elements extracted into tea infusion depend strongly on its solubility in the solution. It is also postulated that chelation of those elements with tannic acid and tannins might cause such variations to occur (Brzezicha-Cirocka et al., 2016).

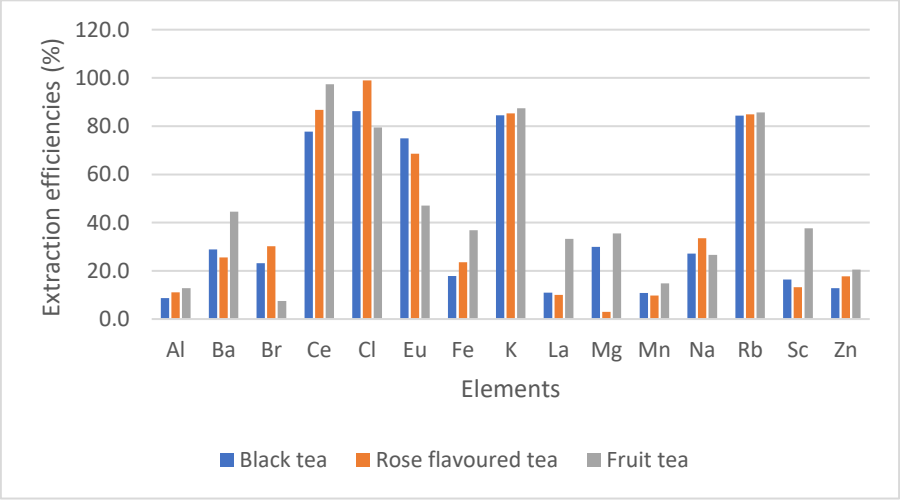

Figure 1 Extraction efficiencies between black tea, rose flavoured tea and fruit tea

Kruskal-Wallis test

Kruskal-Wallis test was performed to determine whether or not there were statistically significant differences between elemental levels of different types of teas. The result showed that there exists such interdependence. Result of the Kruskal-Wallis test is as follows: Al (H = 6.627; p = 0.036), Br (H = 7.855; p = 0.019), Ce (H = 6.627; p = 0.036), La (H = 6.627; p = 0.036), Mn (H = 6.545; p = 0.038), Na (H= 7.282; p = 0.024), Zn (H= 6.627; p = 0.036). The ensuing Dunn's post-hoc test identified elements that are contributing to the differences between black tea and fruit tea as well as rose flavoured tea and fruit tea ($p < 0.05$) as shown in Table 5 below. Previous researchers have used elemental data to differentiate between types of tea or their origin (Fernández-Cáceres et al., 2001; Kara, 2009; Brzezicha-Cirocka et al., 2016; Ma et al., 2019; Lim et al., 2021).

Table 5 Dunn's post-hoc test of the elemental data

	Black tea	Fruit tea
Black tea	-	Al, Ce, La, Mn, Na, Zn
Rose flavoured tea	-	Al, Br

Principal component analysis (PCA)

Principal component analysis (PCA) was attempted with elements that showed statistically significant differences ($p < 0.05$). PCA allows for simplification and provides with graphical visualisation of the data. The first five components with eigenvalue more than 1 were extracted which accounts for 98.9% variances of the data. The first component accounted for 85.9%, the second for 6.3%, the third for 3.9%, the fourth for 1.62% and the fifth for 1.1% of the total variation of the data. Figure 2 shows the PCA scatter plot of PC1 vs PC4 and its loading plot. It is obvious that there was a clear distinction of samples from different types of teas which supports our prior statistical finding. However, one of the black teas was clustered together with rose flavoured tea. Upon inspection, it was revealed that the black tea sample is BT2 which has an indefinite origin than the rest of Malaysian grown black tea. Hence, this might explain why such variation occurred. The first component was known to represent the maximum variation of the data set (Kara, 2009). Hence, from the loading plot Br, Ce, La, Mn and Na have the most discrimination power in the differentiation of types of tea.

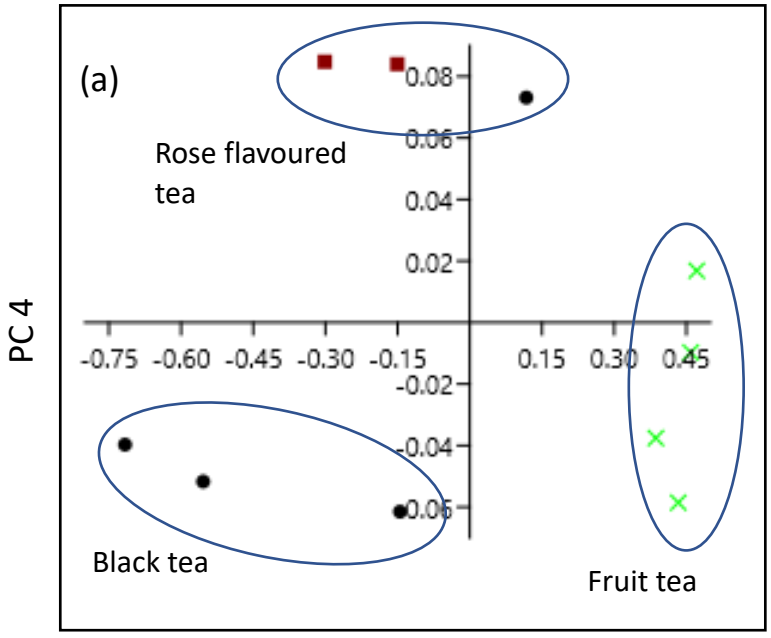

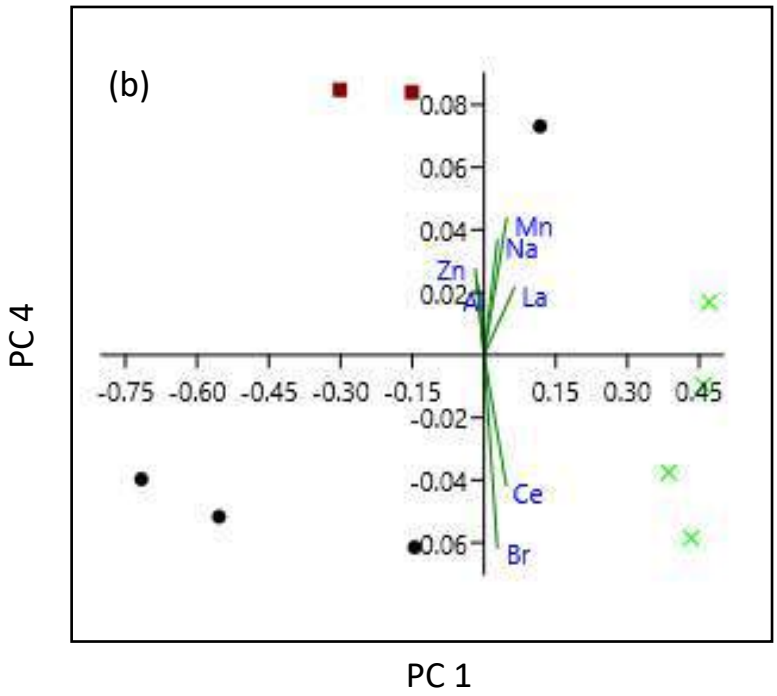

Figure 2 PCA scatter plot of PC1 vs PC4 (a) and its loading plot (b)

CONCLUSION

Analysis results indicate that black tea, rose flavoured tea and fruit tea sold in Malaysian market contain various essential and trace elements which vary according to the tea types. Data analysis showed that tea samples are a good source of essential elements such as K, Na, Mg and Mn. The infusion study showed that these elements might be transferred out into the solution at different rates upon brewing. In general, Ce, Cl, Eu, K and Rb are mostly leached out and can be consumed by the human body. Significant differences were found between black tea and fruit tea, as well as rose flavoured tea and fruit tea based on their elemental levels. The PCA showed that differentiation of types of teas is possible using its mineral profile. This study demonstrates that NAA is a useful tool to assess the quality and safety of teas.

COMPETING INTERESTS

The authors declare that they have no potential competing interests.

ACKNOWLEDGEMENT

The authors express their sincere thanks to personnel from the Analytical Chemistry Application group (ACA) for their help in preparation and irradiation of the samples.

REFERENCES

Brzezicha-Cirocka, J., Grembecka, M. & Szefer, P. (2016). Monitoring of essential and heavy metals in green tea from different geographical origins. *Environ. Monit. Assess.* 188(3):183.

Chajduk, E. (2009). Elemental Analysis of Black and Green Tea Leaves by Instrumental Neutron Activation Analysis. *Chem. Anal. (Warsaw)* 54:841-855.

De Oliveira, L.M., Das, S., da Silva, E.V., Gao, P., Gress, J., Liu, Y. & Ma, L.Q. (2018). Metal concentrations in traditional and herbal teas and their potential risks to human health. *Science of the Total Environment* 633: 649–657.

Deng, Z., Coudray, C., Gouzoux, L., Mazur, A., Rayssiguier, Y. & Pépin, D. (2020). Effects of Acute and Chronic Coingestion of $AlCl_3$ with Citrate or Polyphenolic Acids on Tissue Retention and Distribution of Aluminum in Rats. *Biological Trace Element Research* 76: 245-256.

Elias, M.S., Ibrahim, S., Samuding, K., Ab Rahman, S. & Wo, Y.M. (2018). Assessment of Toxic Elements in Sediments of Linggi River Using NAA and ICP-MS Techniques. *MethodsX* 5: 454–465.

Fernandez-Caceres, P.L., Martin, M.J., Pablos, F. & Gonzalez, A.G. (2001). Differentiation of Tea (Camellia sinensis) Varieties and Their Geographical Origin According to their Metal Content. *J. Agric. Food Chem.* 49: 4775−4779.

Girolametti, F., Annibaldi, A., Illuminati, S., Damiani, E., Carloni, P. & Truzzi, C. (2023). Essential and Potentially Toxic Elements (PTEs) Content in European Tea (Camellia sinensis) Leaves: Risk Assessment for Consumers. *Molecules* 28: 3802.

Han, Q., Mihara, S. & Fujino, T. (2014). Multi-Element Detection in Green, Black, Oolong, and Pu-Erh Teas by ICP-MS. *Biochem Physiol* 3(2): 1000132.

Huang, M., Yang, X., Liu, Z., Mao, Q., Qin, C. & Lv, B. (2016). Determination of Multiple Elemental Concentrations in Tea from China by Inductively Coupled Plasma Optical Emission Spectrometry. *Journal of Food and Nutrition Research* 4(7): 471-477.

Islam, M.A. & Ebihara, M. (2017). Elemental characterization of Japanese green tea leaves and tea infusion residue by neutron-induced prompt and delayed gamma-ray analysis. *Arabian Journal of Chemistry* 10(1): S677-S682.

Jabatan Pertanian Semenanjung Malaysia (2022). Booklet Statistik Tanaman (Sub-Sektor Tanaman Makanan) 2022. Unit Perangkaan Pertanian Bahagian Perancangan Strategik.

Joel, E.S., Maxwell, O., Adewoyina, O.O., Ehi-Eromoseleb, C.O., Embongc, Z. & Oyawoyed, F. (2018). Assessment of natural radioactivity in various commercial tiles used for building purposes in Nigeria. *MethodsX* 5: 8–19.

Jonah, S.A. & Williams, I.S. (2000). Nutrient elements of commercial tea from Nigeria by an instrumental neutron activation analysis technique. *The Science of the Total Environment* 258: 205-208.

Kara, D. (2009). Evaluation of trace metal concentrations in some herbs and herbal teas by principal component analysis. *Food Chemistry* 114: 347–354.

Lagad, R.A., Alamelu, D., Acharya, R. & Aggarwal, S.K. (2011). Instrumental neutron activation analysis for multi-elemental determination in Indian tea samples. *J Radioanal Nucl Chem* 288: 613–620.

Li, L. & Yang, X. (2018). The Essential Element Manganese, Oxidative Stress, and Metabolic Diseases: Links and Interactions. *Oxid Med Cell Longev.* 7580707.

Lin, Y.L., Juan, I.M., Chen, Y.L., Liang, Y.C. & Lin, J.K. (1996). Composition of Polyphenols in Fresh Tea Leaves and Associations of Their Oxygen-Radical-Absorbing Capacity with Antiproliferative Actions in Fibroblast Cells. *J. Agric. Food Chem.* 44: 1387−1394.

Lim, C. M., Carey, M., Williams, P. N. & Koidis, A. (2021). Rapid classification of commercial teas according to their origin and type using elemental content with X-ray fluorescence (XRF) spectroscopy. *Current Research in Food Science* 4: 45–52.

Ma, G., Zhanga, J., Zhang, L., Huang, C., Chen, L., Wang, G., Liu, X. & Lu, C. (2019). Elements characterization of Chinese tea with different fermentation degrees and its use for geographical origins by liner discriminant analysis. *Journal of Food Composition and Analysis* 82: 103246.

Mahani, M.K. & Maragheh, M.G. (2011). Simultaneous Determination of Sodium, Potassium, Manganese and Bromine in Tea by Standard Addition Neutron Activation Analysis. *Food Anal. Methods* 4:73–76.

Martin, C.L. (2007). Tea: The Drink That Changed the World. Tuttle Publishing, North Clarendon, VT, USA.

Matsuura, M., Hokura, A., Katsuki, F., Itoh, A. & Haraguchi, H. (2001). Multielement Determination and Speciation of Major-to-Trace Elements in Black Tea Leaves by ICP-AES and ICP-MS with the Aid of Size Exclusion Chromatography. *Anal. Sci.,* 17: 391-398.

Peluso, I. & Serafini, M. (2017). Antioxidants from black and green tea: from dietary modulation of oxidative stress to pharmacological mechanisms. *British Journal of Pharmacology* 174: 1195–1208.

Polecho'nska, L., Dambiec, M., Klink, A. & Rudeck, A. (2015). Concentrations and solubility of selected trace metals in leaf and bagged black teas commercialized in Poland. *Journal of Food and Drug Analysis* 23(3): 486-492.

Ramdani, D., Chaudhry, A. S. & Seal, C. J. (2013). Chemical Composition, Plant Secondary Metabolites, and Minerals of Green and Black Teas and the Effect of Different Tea-to-Water Ratios during Their Extraction on the Composition of Their Spent Leaves as Potential Additives for Ruminants. *J. Agric. Food Chem.*, 61(20): 4961–4967.

Zhao, H., Zhang, S. & Zhang, Z. (2017a). Relationship between multi-element composition in tea leaves and in provenance soils for geographical traceability. *Food Control* 76: 82-87.

Zhao, H., Yu, C. & Li, M. (2017b). Effects of geographical origin, variety, season and their interactions on minerals in tea for traceability. *Journal of Food Composition and Analysis* 63: 15–20.

Zhang, H.Q., Ni, B.F., Tian, W.Z., Zhang, G.Y., Huang, D.H., Liu, C.X., Xiao, C.J., Sun, H.C. & Zhao, C.J. (2011). Study on essential and toxic elements intake from drinking of Chinese tea. *J Radioanal Nucl Chem* 287: 887–892.

Jurnal Sains Nuklear Malaysia, 2024, 36(No. 1): 31 – 41
ISSN: 2232-0946

SPATIAL TRENDS OF NITRATE LEVEL AND NITRATE STABLE ISOTOPES IN THE LINGGI RIVER

Munirah Abdul Zali[1,2,*], Hafizan Juahir[2], Ananthy Retnam[3], Azharruddin Abdul Aziz[3], Azrul Normi Idris[4], Anuar Sefie[4], Ismail Tawnie[4] and Masni Mohd Ali[5],

[1]Waste and Environmental Technology Division,
Malaysian Nuclear Agency, Bangi, 43000 Kajang, Selangor, Malaysia
[2] East Coast Environmental Research Institute (ESERI), Gong Badak Campus,
Universiti Sultan Zainal Abidin (UNiSZA), 21300, Kuala Nerus, Terengganu, Malaysia
[3] Department of Chemistry of Malaysia, Jalan Sultan, 46661 Petaling Jaya, Selangor, Malaysia
[4]National Hydraulic Research Institute of Malaysia (NAHRIM), Lot 5377,
Jalan Putra Permai, 43300, Seri Kembangan, Selangor, Malaysia
[5]Faculty of Science and Technology, Universiti Kebangsaan Malaysia,
43600, UKM Bangi, Selangor, Malaysia
*Corresponding author: munirahzali@nm.gov.my/munirahabdulzali@gmail.com

ABSTRACT

Determining the isotopic composition of nitrate ($\delta^{15}N\text{-}NO_3^-$ and $\delta^{18}O\text{-}NO_3^-$) in water can provide useful information to identify the sources of nitrate pollution and understand its dynamic behaviour in the aquatic ecosystem. In this study, six river water samples from the Linggi River, Malaysia were obtained to determine the nitrate level and understand possible sources of nitrate pollution using nitrate stable isotopes. The nitrate level and nitrate stable isotopes were measured using ion chromatography (IC) and Continuous Flow Elemental Analyzer Isotope Ratio Mass Spectrometer (CF-EA-IRMS) respectively. The nitrate in the river water samples ranged between 0.97± 0.01 mg L^{-1} and 36.08 ± 0.12 mg L^{-1}. The nitrate level in all river water stations was below than World Health Organization (WHO) and Malaysian Raw Drinking Water guideline level. For nitrate stable isotopes the $\delta^{15}N\text{-}NO_3^-$ values ranged from +1.4‰ to +15.6‰ and the $\delta^{18}O\text{-}NO_3^-$ values ranged from +13.8‰ to +27.4‰ in the river water samples. Based on the cross plot of nitrate stable isotopes, the Linggi River were influenced by the mixture of nitrate pollution sources process from ammonia in fertilizer, soil ammonia, sewage, manure, nitrate fertilizer and atmospheric nitrate. This study reports the signature of nitrate stable isotopes in potential nitrate pollution sources identification and these findings will help further pollution mitigation action for environmental protection.

Keywords: nitrate, nitrate stable isotopes, pollution, river water

INTRODUCTION

Worldwide, nitrates in the natural nitrogen cycle are being increasingly altered due to anthropogenic contributions, such as fossil fuel burning, sewage discharge, agricultural intensification, and intensive farming (DeVries & Zhang, 2016; Filoso, Martinelli, Howarth, & Boyer, 2006; Gutiérrez, Biagioni, Alarcón-Herrera, & Rivas-Lucero, 2018; Jiang et al., 2019; Zafirah et al., 2017; Zhang et al., 2018). In addition, since the beginning of the 20th century, the enormous impact of anthropogenic activities on the environment has altered the nitrogen cycle, doubling the amount the reactive nitrogen (Camargo and Alonso 2006; Gruber and Galloway 2008; Ver et al. 1999). Thus, precise and reliable estimation of nitrate pollution in the ecosystems is warranted.

Nitrate occurs naturally as part of the nitrogen cycle. Despite its natural occurrence, the rising concentrations of nitrate serve as ubiquitous water pollutants. The World Health Organization (WHO) and Malaysian National Raw Drinking Water Guideline have set a limit of 50 mg L^{-1} for nitrate in drinking water sources. Nitrate is a contaminant of concern because its presence is correlated to various environmental problems, such as eutrophication, and health hazards (Akinnawo 2023; Grout et al. 2023). Nitrate causes methemoglobinemia (blue baby syndrome) in children (WHO 2017). Furthermore, increased atmospheric loads of sulfuric and nitric acids from anthropogenic input lead to excess alkalinization and acidification of rivers, in addition to eutrophication (Camargo & Alonso, 2006; Gruber & Galloway, 2008; Wu, Luo, Luo, Ma, & Wang, 2018). These loads enter the river and groundwater via precipitation and may cause environmental harm.

Furthermore, the presence of nitrate in water may be considerably affected by temporal variations, precipitation, hydrogeological conditions, and land use activities (Nejatijahromi et al. 2019). Under many environmental circumstances, isotopes offer definitive source identification because different nitrate sources possess distinct nitrogen and oxygen isotopic signatures. The dual nitrogen and oxygen ratio of nitrate is a valuable fingerprinting tool to identify the predominant source of nitrate pollution in water (Kendall et al., 2007; Li et al., 2010; Michalski, Kolanowskit, & Riha, 2015; Qin, Zhang, & Wang, 2019; Venkiteswaran, Boeckx, & Gooddy, 2019; Zhang, Shi, Song, & Li, 2019). This study aims to determine nitrate levels and nitrate stable isotopes in the river water samples to understand the nitrate pollution sources in the Linggi River.

MATERIALS AND METHODOLOGY

Study Area

Linggi River is located in the Negeri Sembilan state and covers a distance of approximately 1,530 km^2. The river passes through urban areas, such as Seremban and Senawang, as well as rural areas, toward the Strait of Malacca. The Linggi catchment is dominated by residential and industrial areas in the upstream region, while major agricultural activities, small residential areas, and drinking water intake point are located from the middle stream toward the downstream areas. The coordinate points and the description of the sampling locations for this study are shown in Figure 1 and Table 1 respectively.

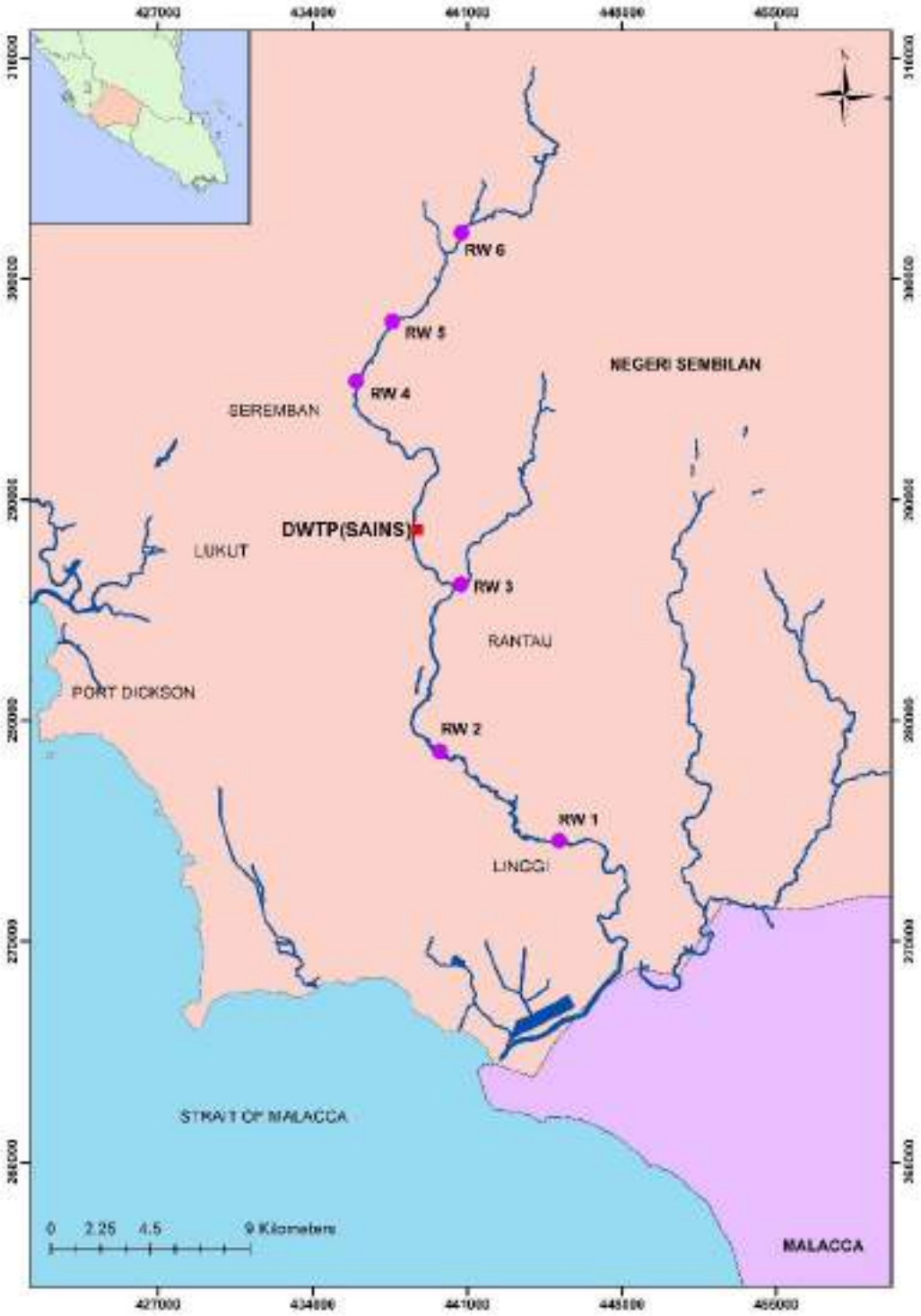

Figure 1. River water sampling location at Linggi River (DWTP= drinking water treatment plant; SAINS= *Syarikat Air Negeri Sembilan*)

Table 1: Description of sampling location

Station	Latitude	Longitude	Land Use
RW1	101.93°	2.68°	Small town, cow farm
RW2	101.91°	2.67°	Residential Areas, sewage treatment plant
RW3	101.96°	2.58°	Palm oil plantations, small towns, residential areas
RW4	101.96°	2.51°	Residential areas
RW5	102.01°	2.48°	Residential areas
RW6	101.96°	2.73°	Residential areas, animal farm

Sampling procedure

The sampling for nitrate and nitrate stable isotopes was conducted in April 2018 at Linggi, Negeri Sembilan, Malaysia. For nitrate level analysis, river water samples were collected using a clean bucket and passed through a 0.45-µm membrane filter. The samples were stored in 250-mL bottles in an icebox and kept in a refrigerator at ±4 °C in the laboratory. The water samples were analyzed within 48 hrs of collection.
For nitrate stable isotope analysis, 4 litres of river water samples were collected using a clean bucket and passed through a 0.45 µm membrane filter, followed by a 0.20 µm membrane filter. All samples for nitrate stable isotope analysis were stored in an icebox and kept in the freezer to prevent any significant chemical and biological changes till further analysis. All samples were analyzed within 48 hrs of collection.

Analysis of nitrate in the river water samples

Nitrate in the water samples was measured using ion chromatography (IC) (ICS 1000 Dionex, USA) following the American Public Health Association (APHA) 4110B standard method. Briefly, the water samples are injected into a stream of eluent in the IC system and passed through a series of ion exchangers. The target anions are separated based on their relative affinities for a low-capacity, strongly basic anion exchanger in the guard and analytical columns of the IC system. The separated anions are directed through suppressors, which continuously suppress eluent conductivity and promote analyte response which in this study in the nitrate ion. In the suppressor, the separated anions are converted to their highly conductive acid forms, while the conductivity of the eluent is greatly decreased. The separated nitrate ion in their acid forms is quantified based on their conductivity and identified based on their retention time (RT). Quantification was performed using the peak area of the ions. Five calibration points of 0.5 mg L^{-1}, 1.0 mg L^{-1}, 2.0 mg L^{-1}, 5.0 mg L^{-1} and 10.0 mg L^{-1} were established with the correlation of coefficient (R^2) of 0.997. Calibration verification (quality control standards) was done for every twenty samples that were analyzed; the values ranged between 90 and 110%. Method blanks and spiked samples were analyzed to ensure method performance with recovery between 70% and 130%. Details of the apparatus, reagent, chemicals, standards, and quality controls are described elsewhere (APHA 2017).

Analysis of nitrate stable isotopes in the river water samples

The nitrate stable isotopes ($\delta^{15}N\text{-}NO_3^-$ and $\delta^{18}O\text{-}NO_3^-$) analyses were carried out using the ion-exchange method based on the United States Geological Survey (USGS) guideline for the determination of $\delta^{15}N\text{-}NO_3^-$ and $\delta^{18}O\text{-}NO_3^-$ (USGS 2001) and literature (Minet et al., 2011; Silva et al., 2000; Xing & Liu, 2011). Briefly, the nitrate in the water samples was extracted using AG50-WX8 and AG1-X8 resins and eluted using 3M hydrochloric acid. After the elution, the neutralization process was performed using silver oxide salt to produce silver nitrate salt from the samples. The silver nitrate salt was freeze-dried and stored prior to analysis. The determination of $\delta^{15}N\text{-}NO_3^-$ and $\delta^{18}O\text{-}NO_3^-$ in the silver nitrate from the water samples was carried out using Continuous Flow Elemental Analyzer Isotope Ratio Mass Spectrometer (CF-EA-IRMS) (SERCON 20-22, UK).

The $\delta^{15}N$ values of samples were reported using conventional delta (δ) notations in per mil (‰) relative to the AIR standard ($\delta^{15}N$ = 0‰). Isotope signatures for $\delta^{15}N$ were calculated as $[R_{sample} - R_{standard}) / R_{standard}] \times 1000$, where R = $^{15}N/^{14}$ N. The $\delta^{18}O$ values of samples are reported using conventional delta (δ) notation in per mil (‰) relative to the Vienna Standard Mean Ocean Water (V-SMOW) ($\delta^{18}O$ = 0‰) and calculated as $[R_{sample} - R_{standard}) / R_{standard}] \times 1000$, where R = $^{18}O/^{16}$ O.

RESULTS AND DISCUSSION

The level of nitrate in the river water samples

Figure 2 presents the values of nitrates in river water samples at RW1-RW6 from the Linggi River. The nitrate level in RW1, RW2, RW3, RW4, RW5 and RW6 were 10.28 ± 0.12 mg L^{-1}, 17.51 ± 0.15 mg L^{-1}, 36.08 ± 0.12 mg L^{-1}, 0.98 ± 0.01 mg L^{-1}, 2.42 ± 0.02 mg L^{-1}, and 2.17 ± 0.06 mg L^{-1} respectively (Figure 2). The range of nitrate concentration in the river water samples was between 0.97± 0.01 mg L^{-1} and 36.08 ± 0.12 mg L^{-1}. The highest nitrate concentration was observed at the RW3 station. This station was surrounded by residential areas and palm oil plantations. The highest nitrate level in this station may be due to the potential of nitrate sources from fertilizer and also from the discharge of sewage effluent from residential areas (Abdul Zali et al. 2021; Zainuddin et al. 2020).

The nitrate levels in samples from RW1, RW2, and RW3 exceeded the base level (5 mg L^{-1}) based on literature by Wang et al. (2017) and Panno et al. (2006) and were lower than the WHO guideline (Figure 2). Based on the literature and the author's knowledge, till recent years, the study on the base level of nitrate concentration was unavailable and/or not reported in the Malaysian region. The RW1, RW2, and RW3 stations are in the downstream part of the river, and the abundance of nitrates in samples from these stations may be attributed to input from nearby point and non-point sources as well as cumulative loading of pollutants from the upstream region (Yang et al., 2016). The anthropogenic pollution from point and non-point sources was anticipated at RW1, RW2, and RW3, however, fertilizer waste may serve as the major contributor in these regions, as they are surrounded by massive rubber and palm oil plantations (Zainuddin et al. 2020). Although the nitrate levels in samples from RW4, RW5, and RW6 were slightly lower than the base level, their concentrations should not be overlooked given the potential risk of elevated nitrate from the surrounding areas and also contribute to cumulative loading of nitrate in the downstream regions.

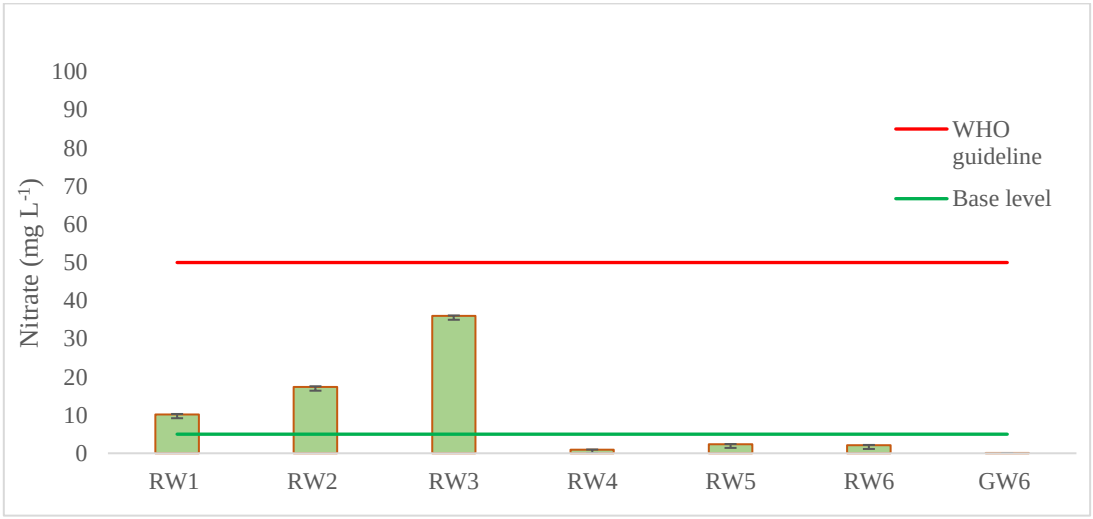

Figure 2. Nitrate concentrations in river water samples

Signature of nitrate stable isotopes in the river water samples

The determination of nitrate level in the river water samples delivers the distribution information of nitrate in the Linggi River. To understand the potential nitrate pollution sources and transformation processes of nitrates from anthropogenic activities, the $\delta^{15}N\text{-}NO_3^-$ and $\delta^{18}O\text{-}NO_3^-$ signatures of water samples were extracted and analyzed using CF-EA-IRMS. The $\delta^{15}N\text{-}NO_3^-$ and $\delta^{18}O\text{-}NO_3^-$ signatures of river water can be used for the evaluation of the potential sources of nitrate (Fenech et al. 2012; Kendall 1998). The $\delta^{15}N\text{-}NO_3^-$ and $\delta^{18}O\text{-}NO_3^-$ compositions of nitrate in the river water samples are plotted in Figures 3 (a) and (b) respectively. From the nitrate stable isotope analysis, the $\delta^{15}N\text{-}NO_3^-$ values ranged from +1.4‰ to +15.6‰ and the $\delta^{18}O\text{-}NO_3^-$ values ranged from +13.8‰ to +27.4‰ in the river water samples.

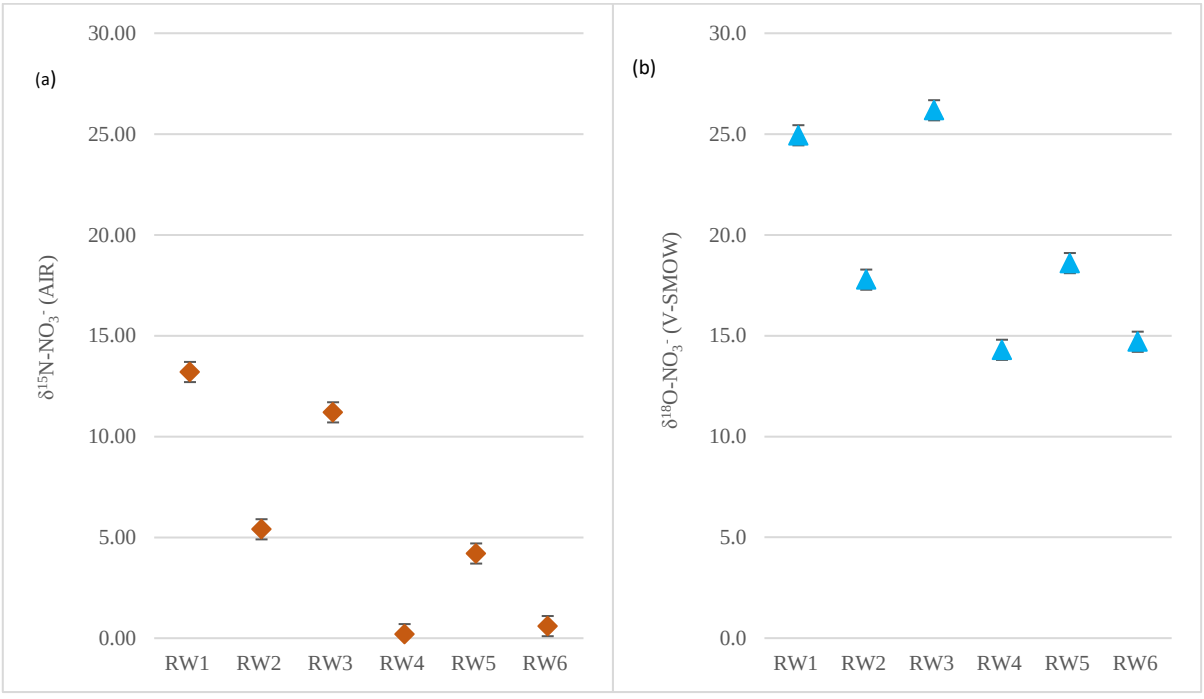

Figure 3. Spatial variations in $\delta^{15}N\text{-}NO_3^-$ (a) and $\delta^{18}O\text{-}NO_3^-$ (b) in river water samples

Sources of nitrate stable isotopes in the river water samples

In Figure 4, the measured δ^{15}N-NO_3^- and δ^{18}O-NO_3^- values are colour coded according to spatial variations and overlaid on the estimated nitrate isotopic ranges of common sources in literature (Kendall 1998; Kendall et al. 2007; Kendall and Aravena 2000). At RW1 and RW3, the δ^{15}N-NO_3^- values were between 11.3‰ and 15.6‰ and the δ^{18}O-NO_3^- values were between 23.0‰ and 27.4‰. The high δ^{15}N-NO_3^- and δ^{18}O-NO_3^- values at RW1 and RW3 during both seasons may be attributed to the atmospheric nitrate from fixation processes associated with the release of nitrogen oxide (NO_x) into the atmosphere from human activities (e.g., fossil fuel combustion) and natural processes (biogenic soil emission, biomass burning, and lightning) (Kendall et al., 2007; Li et al., 2020). Based on Figure 2, the high nitrate level at RW1 and RW3 stations (above base level) may due to the atmospheric nitrate sources.

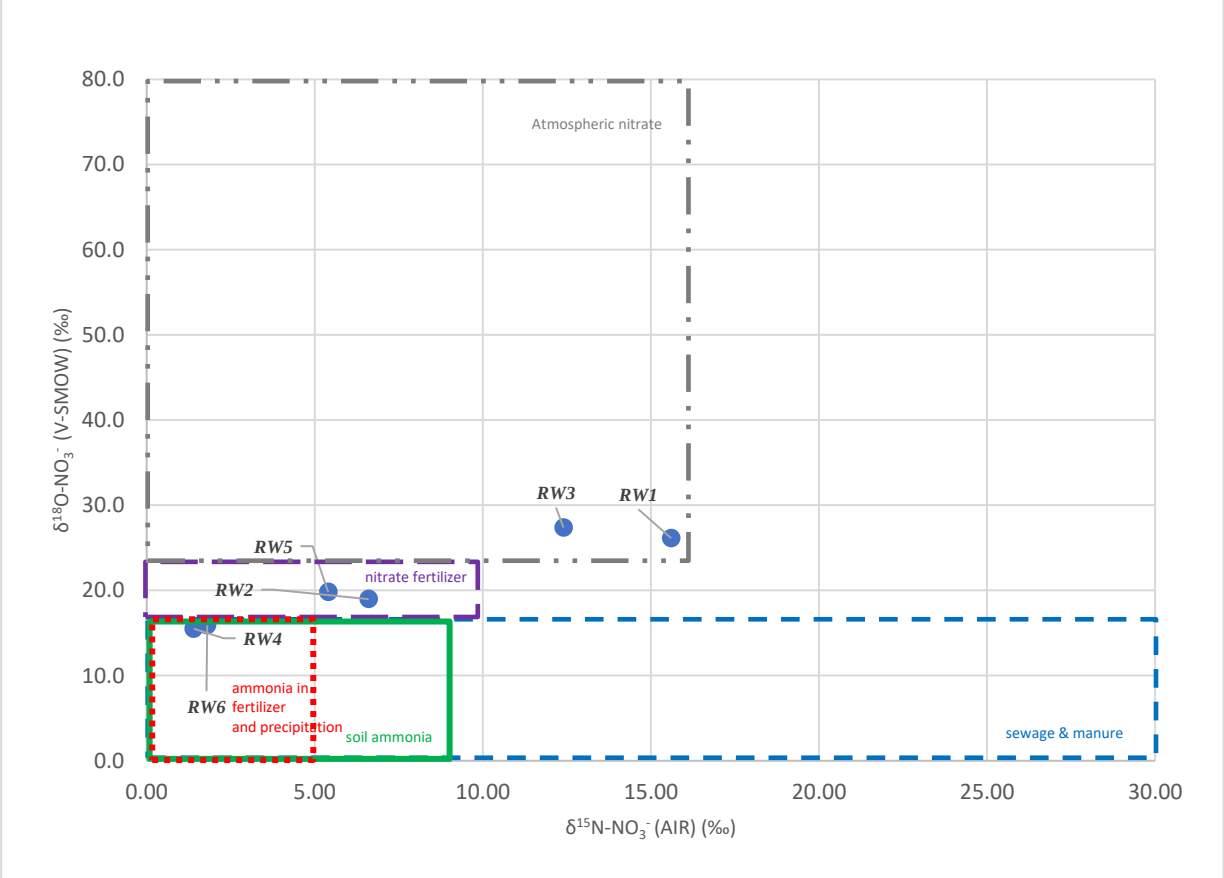

Figure 4. Cross plot of δ^{15}N-NO_3^- and δ^{18}O-NO_3^- values in river water samples. The isotopic composition of various sources in the diagram is derived from (Kendall 1998; Kendall et al. 2007)

At RW2 and RW5, nitrate-based fertilizers were the major source of nitrate, with δ^{15}N-NO_3^- values between 4.9‰ and 6.6‰ and δ^{18}O-NO_3^- values between 19.0‰ and 22.2‰. RW2 and RW5 are located near large palm oil and rubber plantations. The higher nitrate levels at RW2 (exceeding the base level) than at RW5 (below the base level) may be attributed to the larger plantation areas near RW2 (Rantau) than those near RW5 (Seremban), with a mixture of plantations and residential areas. The high and low nitrate concentration patterns from these stations were derived from similar nitrate fertilizer sources.

As shown in Figure 4, at RW4 and RW6, nitrification values were between -5‰ and 15‰ of $\delta^{18}O\text{-}NO_3^-$ values (Kendall et al. 2007). At RW4 and RW6, the $\delta^{15}N\text{-}NO_3^-$ values were between 1.4‰ and 2.3‰ and the $\delta^{18}O\text{-}NO_3^-$ values were between 13.8‰ and 15.9‰. RW4 and RW6 presented with the lowest $\delta^{15}N\text{-}NO_3^-$ values compared to other $\delta^{15}N\text{-}NO_3^-$ in other sampling stations. As shown in Figure 4, RW4 and RW6 were affected by ammonia in fertilizers, precipitation, sewage, and manure nitrate pollution sources (+0‰ to +25‰). Even though the nitrate concentration in RW4 and RW6 was below the base level, these stations were influenced by various types of potential nitrate pollution sources based on the crossplot of $\delta^{15}N\text{-}NO_3^-$ and $\delta^{18}O\text{-}NO_3^-$.

CONCLUSION

Nitrate concentration in river water samples exceeded the base level of nitrate and was lower than the WHO guideline. The elevated nitrate concentration at the downstream stations may be explained by the cumulative loading of nitrate from the upstream regions as well as anthropogenic activities in nearby areas as well as point sources from the nearby areas. The cross plot of $\delta^{15}N\text{-}NO_3^-$ and $\delta^{18}O\text{-}NO_3^-$ capables to identify the potential nitrate pollution sources in the sampling locations with higher and lower nitrate concentrations compared to the nitrate base level. From the cross plot of $\delta^{15}N\text{-}NO_3^-$ and $\delta^{18}O\text{-}NO_3^-$, the river water samples of Linggi were affected by mixture of nitrate pollution from atmospheric nitrate, nitrate fertilizer, ammonia in fertilizers, precipitation, soil ammonia, manure, and sewage.

ACKNOWLEDGEMENT

The authors would like to thank to the Ministry of Higher Education (MOHE) of Malaysia for supporting this research under the Fundamental Research Grant Scheme (FRGS) No: FRGS/1/2017/STG01/UNISZA/02/2 and Internal UNiSZA grant: UNiSZA/2017/SRGS/18. Research funding was also provided by the Centre of Hydrogeology, National Hydraulic Research Institute of Malaysia (NAHRIM) under the project *Integrated surface and groundwater physical-based model of Linggi, Muda and Langat River Basin*

REFERENCES

Abdul Zali, M., Juahir, H., Ismail, A., Retnam, A., Idris, A. N., Sefie, A., et al. (2021). Tracing sewage contamination based on sterols and stanols markers within the mainland aquatic ecosystem: a case study of Linggi catchment, Malaysia. *Environmental Science and Pollution Research*. https://doi.org/10.1007/s11356-020-11680-5

Akinnawo, S. O. (2023). Eutrophication: Causes, consequences, physical, chemical and biological techniques for mitigation strategies. *Environmental Challenges*, *12*(May). https://doi.org/10.1016/j.envc.2023.100733

APHA. (2017). Standard Method For the Examination of Water and Wastewater. In *American Journal of Public Health and Nations Health* (23rd ed.). USA. https://doi.org/https://doi.org/10.2105/SMWW.2882.070

Camargo, J. A., & Alonso, Á. (2006). Ecological and toxicological effects of inorganic nitrogen pollution in aquatic ecosystems : A global assessment. *Environment International*, *32*(6), 831–849. https://doi.org/10.1016/j.envint.2006.05.002

DeVries, S. L., & Zhang, P. (2016). Antibiotics and the Terrestrial Nitrogen Cycle: A Review. *Current Pollution Reports*, *2*(1), 51–67. https://doi.org/10.1007/s40726-016-0027-3

Fenech, C., Rock, L., Nolan, K., Tobin, J., & Morrissey, A. (2012). The potential for a suite of isotope and chemical markers to differentiate sources of nitrate contamination: A review. *Water Research*, *46*(7), 2023–2041. https://doi.org/10.1016/j.watres.2012.01.044

Filoso, S., Martinelli, L. A., Howarth, R. W., & Boyer, E. W. (2006). Nitrogen Cycling in the Americas: Natural and Anthropogenic Influences and Controls. *Nitrogen Cycling in the Americas: Natural and Anthropogenic Influences and Controls*, (January). https://doi.org/10.1007/978-1-4020-5517-1

Grout, L., Chambers, T., Hales, S., Prickett, M., Baker, M. G., & Wilson, N. (2023). The potential human health hazard of nitrates in drinking water: a media discourse analysis in a high-income country. *Environmental Health: A Global Access Science Source*, *22*(1), 1–11. https://doi.org/10.1186/s12940-023-00960-5

Gruber, N., & Galloway, J. N. (2008). An Earth-system perspective of the global nitrogen cycle. *Nature*, *451*(7176), 293–296. https://doi.org/10.1038/nature06592

Gutiérrez, M., Biagioni, R. N., Alarcón-Herrera, M. T., & Rivas-Lucero, B. A. (2018). An overview of nitrate sources and operating processes in arid and semiarid aquifer systems. *Science of the Total Environment*, *624*, 1513–1522. https://doi.org/10.1016/j.scitotenv.2017.12.252

Jiang, S., Müller, M., Jin, J., Wu, Y., Zhu, K., Zhang, G., et al. (2019). Dissolved inorganic nitrogen in a tropical estuary at Malaysia: transport and transformation. *Biogeosciences Discussions*, 1–27. https://doi.org/10.5194/bg-2019-7

Kendall, C. (1998). Tracing Nitrogen Sources and Cycling in Catchments. In *Isotope Tracers in Catchment Hydrology* (pp. 519–576).

Kendall, C., & Aravena, R. (2000). Nitrate isotopes in groundwater system. In P. Cook & A. ;. Herczeg (Eds.), *Environmental tracers in subsurface hydrology* (pp. 261–297). CSIRO Land and Water, Glen Osmond, Australia: Springer Science+ Business Media LLC. https://doi.org/10.1007/978-1-4615-4557-6

Kendall, C., Elliott, E. M., & Wankel, S. D. (2007). Tracing anthropogenic inputs of nitrogen to ecosystems. In R. Michener & K. Lajtha (Eds.), *Stable Isotopes in Ecology and Environmental Science* (pp. 375–445). Blackwell Publishing.

Li, C., Li, S. L., Yue, F. J., He, S. N., Shi, Z. B., Di, C. L., & Liu, C. Q. (2020). Nitrate sources and formation of rainwater constrained by dual isotopes in Southeast Asia: Example from Singapore. *Chemosphere*, *241*. https://doi.org/10.1016/j.chemosphere.2019.125024

Li, S.-L., Liu, C.-Q., Li, J., Liu, X., Chetelat, B., Wang, B., & Wang, F. (2010). Assessment of the sources of nitrate in the Changjiang River, China using a nitrogen and oxygen isotopic approach. *Environmental science & technology*, *44*(5), 1573–1578. https://doi.org/10.1021/es902670n

Michalski, G., Kolanowski, M., & Riha, K. M. (2015). Oxygen and nitrogen isotopic composition of nitrate in commercial fertilizers, nitric acid, and reagent salts. *Isotopes in environmental and health studies*, (July 2015), 1–10. https://doi.org/10.1080/10256016.2015.1054821

Minet, E., Goodhue, R., Coxon, C. E., Kalin, R. M., & Meier-Augenstein, W. (2011). Simplifying and improving the extraction of nitrate from freshwater for stable isotope analyses. *Journal of environmental monitoring : JEM*, *13*(7), 2062–6. https://doi.org/10.1039/c1em10289c

Nejatijahromi, Z., Nassery, H. R., Hosono, T., Nakhaei, M., Alijani, F., & Okumura, A. (2019). Groundwater nitrate contamination in an area using urban wastewaters for agricultural irrigation under arid climate condition, southeast of Tehran, Iran. *Agricultural Water Management*, *221*(April), 397–414. https://doi.org/10.1016/j.agwat.2019.04.015

Panno, S. V., Kelly, W. R., Martinsek, A. T., & Hackley, K. C. (2006). Estimating Background and Threshold Nitrate Concentrations Using Probability Graphs. *Ground Water*, *44*(5), 697–709. https://doi.org/10.1111/j.1745-6584.2006.00240.x

Qin, Y., Zhang, D., & Wang, F. (2019). Using nitrogen and oxygen isotopes to access sources and transformations of nitrogen in the Qinhe Basin, North China. *Environmental Science and Pollution Research*, *26*(1), 738–748. https://doi.org/10.1007/s11356-018-3660-0

Silva, S. R., Kendall, C., Wilkison, D. H., Ziegler, A. C., Chang, C. C. Y., & Avanzino, R. J. (2000). A new method for collection of nitrate from fresh water and the analysis of nitrogen and oxygen isotope ratios. *Journal of Hydrology*, *228*(1–2), 22–36. https://doi.org/10.1016/S0022-1694(99)00205-X

USGS. (2001). Instruction for Collection and Recovery of Nitrate for d15N and d18O Analysis. https://wwwrcamnl.wr.usgs.gov/isoig/guidelines/nitrate/index.html. Accessed 1 December 2016

Venkiteswaran, J. J., Boeckx, P., & Gooddy, D. C. (2019). Towards a global interpretation of dual nitrate isotopes in surface waters. *Journal of Hydrology X*. https://doi.org/10.1016/j.hydroa.2019.100037

Ver, L. M. B., Mackenzie, F. T., & Lerman, A. (1999). Carbon cycle in the coastal zone: Effects of global perturbations and change in the past three centuries. *Chemical Geology*, *159*(1–4), 283–304. https://doi.org/10.1016/S0009-2541(99)00042-X

Wang, S., Zheng, W., Curerell, M., Yang, Y., Zhao, H., & Lv, M. (2017). Relationship between land-use and sources and fate of nitrate in groundwater in a typical recharge area of the North China Plain. *Science of the Total Environment*, *609*, 607–620. https://doi.org/10.1016/j.scitotenv.2017.07.176

WHO. (2017). Guidelines for drinking-water quality, 4th edition, incorporating the 1st addendum.

Wu, Y., Luo, Z., Luo, W., Ma, T., & Wang, Y. (2018). Multiple isotope geochemistry and hydrochemical monitoring of karst water in a rapidly urbanized region. *Journal of Contaminant Hydrology*, *218*(March), 44–58. https://doi.org/10.1016/j.jconhyd.2018.10.009

Xing, M., & Liu, W. (2011). An improved method of ion exchange for nitrogen isotope analysis of water nitrate. *Analytica Chimica Acta*, *686*(1–2), 107–114. https://doi.org/10.1016/j.aca.2010.11.051

Yang, X., Liu, Q., Fu, G., He, Y., Luo, X., & Zheng, Z. (2016). Spatiotemporal patterns and source attribution of nitrogen load in a river basin with complex pollution sources. *Water Research*, *94*, 187–199. https://doi.org/10.1016/j.watres.2016.02.040

Zafirah, N., Ilham, J. I. J., R., M., A., M. S., Shaiful, Y., & Syakir, M. I. (2017). Isotopic (13C and 15N) Variation in Tropical RIver Sediments of Kelantan, Malaysia: A Reconnaissance Study of Land Use Impact to the Watershed. *Applied ecology and Environmental Research*, *15*(4), 1101–1119. https://doi.org/10.15666/aeer/1504

Zainuddin, A. H., Wee, S. Y., & Aris, A. Z. (2020). Occurrence and potential risk of organophosphorus pesticides in urbanised Linggi River, Negeri Sembilan, Malaysia. *Environmental Geochemistry and Health*, *42*(11), 3703–3715. https://doi.org/10.1007/s10653-020-00604-4

Zhang, Y., Shi, P., Li, F., Wei, A., Song, J., & Ma, J. (2018). Quantification of nitrate sources and fates in rivers in an irrigated agricultural area using environmental isotopes and a Bayesian isotope mixing model. *Chemosphere*, *208*, 493–501. https://doi.org/10.1016/j.chemosphere.2018.05.164

Zhang, Y., Shi, P., Song, J., & Li, Q. (2019). Application of nitrogen and oxygen isotopes for source and fate identification of nitrate pollution in surfacewater: A review. *Applied Sciences (Switzerland)*, *9*(1). https://doi.org/10.3390/app9010018

Jurnal Sains Nuklear Malaysia, 2024, 36(No. 1): 42 – 61
ISSN: 2232-0946

IMPROVEMENT IN RADIATION PROTECTION INFRASTRUCTURE FOR X-RAY FACILITIES IN BANGLADESH: THE ROLE OF THE EXECUTIVE REGULATORY AUTHORITY

Md. Kabir Ahamed*, Meherun Nahar, Md. Akramuzzaman, and Nadia Akter Mokta

Bangladesh Atomic Energy Regulatory Authority, Dhaka-1207, Bangladesh
*Corresponding author: fbkabir@gmail.com

ABSTRACT

The national regulatory body in the state regulates the source of ionizing radiation, to optimize exposure for occupational radiation workers and public. The Bangladesh Atomic Energy Regulatory Authority covers all radiological regulatory aspects of ionizing radiation, such as diagnostic X-ray facilities for all practices and intervention requirements. The study presents an assessment and analyses the degree of technical radiation protection requirements and the status of improvement in the national regulatory standards for 230 different facilities in the four particular districts in Bangladesh. The methods used included comprehensive on-site inspections, visual assessments of equipment, operational observations, staff interviews, and technical evaluations. Safety system tests were conducted, and compliance records, licensing, and training programs were reviewed. The main objective is to ensure all the regulatory requirements are being fulfilled by analyzing data on radiation protection matters. In the cases of public and radiation workers, approximately 77% and 56% of dose rates in the examined facilities, respectively, were following the radiological protection technical regulation. However, significant progress has been observed in the facilities in the last few years since the authority initiated the regulatory program.

Keywords: Ionizing Radiation, X-ray Facility, Regulatory Authority, Radiation Protection, Occupational Worker.

1. INTRODUCTION

Radiation may have a significant impact on health and disease, possibly with proper use and prevention of misuse or overuse. It has many beneficial applications, but, as in every single activity of human life, when risks are associated with its use, specific actions need to be put in place to protect the people and environment. Although ionizing radiation has many benefits, it can also be detrimental (1). It can come from various sources, including cosmic rays and natural radionuclides in air, food, and water (2). The rationale for using radiation for diagnosis and treatment is developing, and hence the need that this practice be promoted and perfected (3). Protection from radiation risks needs to be improved (4). Therefore, appropriate justification is needed before using radiation.

The Basic Safety Standard (BSS 115) of International Atomic Energy Agency (IAEA) has outlined basic steps for creating a legislative and regulatory framework to guarantee a secure and safe working environment in radiation installations (5). First of all, BSS 115 categorizes the radiation exposure into the three categories such as occupational, medical and public exposures. Occupational exposure is defined as the exposure that is incurred while at work and mostly as a

result of work. The public exposures include all other exposures, while the medical exposures, which are mostly exposures of patients, are obtained during diagnosis or treatment.

Moreover, this medical exposure is the largest man-made source of radiation exposure, accounting for more than 95% of total radiation exposure (6). According to IAEA and national standard, the requirements of fundamental radiation protection principle are desired to be followed during working with any sort of radioactive materials or radiation generating equipment (such as X-ray machines, CT scanners, Dental, Mammography, C-arms etc.) (7).

In order to reduce radiation destructive impacts, the International Committee on Radiological Protection (ICRP) developed dose limits for usage in the workplace and by the general public in 1960. Nevertheless, there is still no exposure limit for patients; instead, advisory levels are offered for them (8). Therefore, it is very important to know about radiation mechanisms, the dose from regularly used radiation generating equipment, the magnitude or limit, and type of risks (9,10). Generally, society accepts radiation risk on the conditional basis as benefit to be gained from the use of radiation generating equipment or radioactive sources. However, the risks should be limited and complied against the application of radiation safety standards developed by national and international organizations (11).

In Bangladesh, radiological diagnostic facilities having radiation generating X-ray units are consistently increasing day by day from city to rural areas, for establishing the public health demand. It has been determined that in order to ensure effective, efficient, and uniform regulatory control in medical X-ray equipment and installations, the radiation protection infrastructure of every X-ray unit in the nation needs to be specifically analyzed. Since the late 1990s, Bangladesh has prioritized radiation safety and protection. The national regulatory body has implemented a program to evaluate the infrastructure by conducting regular inspections and radiation surveys of all radiation-generating machinery. The objective is to improve the regulatory framework, update the inventory of equipment, and enhance awareness about radiation safety among stakeholders. The situation gradually started improving and regulatory inspections were performed from time to time in order to update the inventory and make the concerned people alert towards the radiation safety, which has been reflected in the post regulated scenarios of the radiation protection infrastructure of the facilities.

In this report some inspections were carried out to collect and investigate the regulatory data on such radiation generating equipment in four different districts in Bangladesh (Feni, Jhalokati, Rajshahi, and Cox`s Bazar) as a part of the regulatory program. This study's outcomes are expected to guide future regulatory efforts, helping to strengthen radiation safety and protection infrastructure in the surveyed districts and potentially across the entire country.

2. STATUS OF RADIATION SAFETY AND PROTECTION INFRASTRUCTURE DEVELOPMENT

2.1 Legislative framework and international legal instruments

People have the fundamental right to get health treatment, and the government shall regard the improvement of public health as among its primary duties, as stated in the constitution of Bangladesh. In the 1990s, the Bangladesh Atomic Energy Commission (BAEC) took the initiative to develop a legal framework for controlling radiation-related activities. On the basis of this effort Bangladesh government promulgated Nuclear Safety and Radiation Control (NSRC) act in 1993 and the corresponding NSRC rules in 1997 where the basic radiation safety requirements of BSS 115 have been incorporated (12,13). For betterment of peaceful atomic activity and to ensure nuclear and radiation safety in a superior way as well as to establish an independent regulatory authority, named as Bangladesh Atomic Energy Regulatory Authority (BAERA) (11). The nuclear and radiation safety legislation and regulation are shown in Fig. 1 in a hierarchical order. BAER Act-2012 is the comprehensive legal framework for the regulation and monitoring of peaceful applications of atomic energy and radiation, which covers the issues of safety and radiation protection, environmental protection, control of the operation, emergency preparedness, and response, transport of nuclear and radioactive material etc. It can be mentioned here that the 'NSRC Act-1993' is repealed now, as BAER Act-2012 is promulgated. Bangladesh does not have a distinct legislation pertaining to radiation safety aside from these Acts.

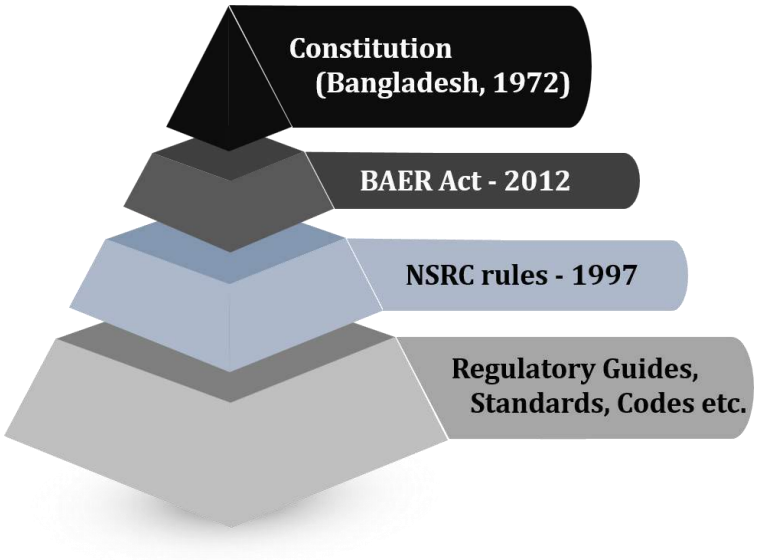

Fig. 1 Hierarchy of legislative framework for radiation safety

2.2 Regulatory framework

The regulatory framework is based on the BAER Act-2012 and the subordinate legislation i.e. bylaw-the NSRC rules-1997, which is still enforced (13). As shown in Fig. 1, radiation safety regulations, safety guides, standards, and codes for design, construction, inspections, licensing reviews, and enforcement activities are yet to be developed. Establishment of the regulatory authority, office premises, constitution, tenure of chairman and members, and responsibilities and

functions of the authority is stated in Section 4, 5, 6, 7, and 11 of the BAER Act-2012. The prime responsibility of the regulatory authority is to regulate the radiation safety through authorization, inspection, and enforcement under the provision of Section 11 of the BAER Act-2012 and the nuclear safety and radiation control (NSRC) rules-1997. Within the existing structure of the government, as shown in Fig. 2, BAERA operates as an autonomous body under the MoST. BAERA has five divisions. Among them, the nuclear safety, security & safeguard division is responsible for safety of nuclear activities while the radiation, transport & waste safety division is overseeing the safety of nuclear and radiological activities. The decision-making body of the regulatory authority consists of four members and a chairman. The chairman is the chief executive who works under the secretary and minister of the Ministry of Science and Technology (MoST). To create any regulatory documents such as regulations, rules, standards, guides, codes, etc., the regulatory authority has to take the proper initiative following the BAER Act-2012 and BAERA's administrative MoST is the responsible organization to approve them.

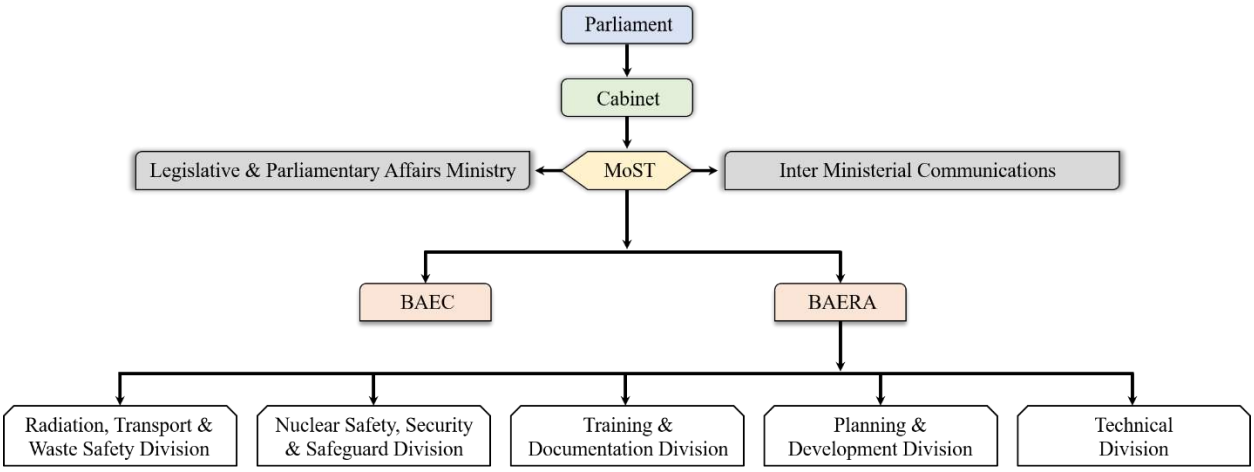

Fig. 2 Structure of national framework of regulatory for radiation safety

If a new Act/law is to be developed or the amendment of BAER Act-2012 or NSRC rules-1997 is required, it will go to the concerned law ministry, cabinet, and then to the parliament for final approval. To acquire a license, the licensee should apply to the regulatory authority in filling out all prescribed forms by the regulatory requirements.

2.3 Regulatory body inspection and responsibilities

The inspection checklist is one of the most crucial inspection tools for the regulatory body to properly conduct the inspection procedure. The prime activity of the regulatory body is the so-called planned inspections. The inspection may take place either announced or unannounced. Unannounced inspections force the regulatory agency to investigate the facility's actual condition. This makes this kind of inspection the preferable one over the others. The other type of inspection is the announced inspection, which enables the inspectors to actively interview users or RCOs (Radiation Control Officers) and cover a wide range of topics with them. For computed tomography (CT), interventional radiology (IR), fluoroscopy, and mammography X-ray facilities, the recommended minimum range of inspection frequencies is 3 years, but the corresponding number for conventional X-ray is 5 years (14,15). The ability to regularly apply for the quality control program, as outlined in the international guideline; the positioning of the X-ray machine

and the layout of the X-ray room with regard to occupancy and neighboring room. The inspector should choose radiation measurement instruments at random, such as portable survey equipment or stationary monitoring equipment, and assess them to ensure their effectiveness (15).

The following items will be examined by the regulator: (i) The managing organization's users are equipped with a system to guarantee that medical exposures are covered by an approved method and handled by occupational radiation workers in accordance with the ALARA concept (as low as reasonably achievable). (ii) The duty of protecting patients was delegated in a way that is appropriate for a trained medical expert, such as a radiologist. (iii) The calibration of the user equipment, such as clinical dosimetry, imaging tools, and quality control, was created for a skilled specialist, like a medical physicist. (iv) All radiation workers possess valid credentials and enough training in radiation protection and legal requirements. (v) The absorbed dose provided to the patient must be optimized, and a program for quality control test procedures for X-ray machines, including dose measurements, must be frequently carried out at the facility (15, 16).

3. METHODOLOGY

A comprehensive inspection/re-inspection was carried out and a detail radiation safety assessment has been performed in the 230 private and government diagnostic facilities containing with X-ray units, which are located in at four different districts in Bangladesh. For this current investigation, we choose Feni (South-eastern), Jhalokati (Southern), Rajshahi (Mid-western), and Cox`s Bazar (South-eastern) district in Bangladesh. The selection of the specific districts for this study based on a combination of factors aimed at providing a representative assessment of radiation protection standards across diverse regions in Bangladesh.

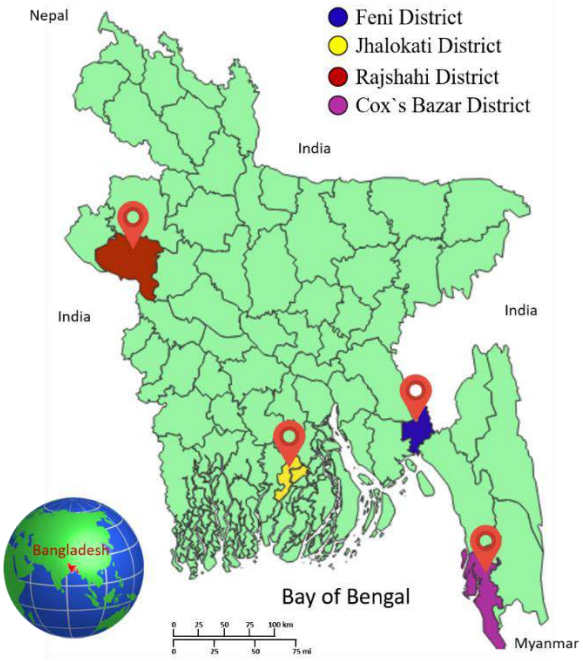

The above map shows the locations of the medical or diagnostic facilities in Bangladesh where the inspections and re-inspections were ethically performed.

3.1 Inspection parameters and instruments

This study used a quantitative, non-experimental, descriptive method to gather data on radiation protection and safety measures. At first, a full fledge regulatory inspection checklist/questionnaire was prepared including various regulatory information from the construction design and layout of the X-ray facility for the field survey. The checklist consisted of a combination of 17 closed and open-ended regulatory requirements. The dimensions of the room, including its length and width, wall thickness, door and control panel shielding condition, and thickness, were used to design the layout of the radiation-generating X-ray machine room. The layout also included the locations of the X-ray machine, chest stand, control panel, dark room, computed radiography room, and surrounding areas.

In this inspection the radiation exposure levels were measured using two portable Geiger Muller (GM) and scintillation micro-Roentgen survey meter (LUDLUM, Model: 3 and 26) and pressurized ion-chamber (LUDLUM, Model: 9DP) type of radiation dose rate meters. For GM or scintillation based micro-Roentgen survey meter, the reading in μR/h were converted to μSv/h using the conversion factor (from the definition of Roentgen). The dose rate was then assessed at various points within the X-ray room, including the control panel (CP), entrance door (ED), dark room (DR), computed radiography (CR) room, as well as any extra doors. Year of putting in of the X-ray machine, type of the X-ray machine, including model, serial number, manufacturer, maximum tube potential (kV), maximum tube current (mA), light beam diaphragm, and total tube filtration, as well as the number of radiation workers involved, including the technologist and technician, were also noted during the inspection. The investigation found that personal monitoring data are kept and retained, adequate personal protective equipment is available, and occupational worker wear personal dosimetry devices on the proper part of their bodies. It was determined whether or not the persons around and the general public were exposed to radiation by observing the areas around the X-ray room. Also, it is evaluated to determine whether facility staff members are abiding by the rules and effectively carrying out their normal duties. The existence of a radiation sign and a warning signal at the X-ray room's appearance point was also evaluated.

An inspection report was created after compiling a variety of regulatory data, and it contained recommendations for enhancing the radiation safety status. Subsequently, a re-inspection was carried out to determine whether any changes had been made to the facilities with regard to the radiation protection issue. In this study, findings also include an analysis of the current regulatory data in comparison to previous inspection data which have been presented in the different tables.

3.2 Statistical analysis

The regulatory data where cumulatively collected and analyzed using tables, charts, and graphs to determine the safety culture that deal with radiation in the above X-ray facilities where the equipment and the checklist was used. All the results are reported as an arithmetic mean value and the spread of the data is given by standard error. Data were processed and visualized using Microsoft Excel (Microsoft Office 2019, Ver. 16.0.10730.20102) and OriginPro 2019b (OriginLab Corporation, Ver. 9.6.5.169).

4. RESULTS

The investigation was done for X-ray units and their corresponding radiation workers in the field of medical or diagnostic radiography. A total of 230 facilities out of 350 were analyzed in four different districts in several region of Bangladesh, where almost 281 radiation generating machines were carefully inspected. Among all the machines, the most fixed type X-ray machines were found. In Table 1, the number of monitored medical or diagnostic facilities in the corresponding year is depicted, and an increasing tendency is observed in the number of facilities as well as X-ray units, whether they are authorized or not.

Jurnal Sains Nuklear Malaysia, 2024, 36(No. 1): 42 – 61
ISSN: 2232-0946

Table 1. Comparison of radiological infrastructure before and after regulatory inspections across four districts in Bangladesh

District`s Name	Location in Bangladesh	Total Facility, *N*		Authorized X-ray Facility, *N* (%)		Duration of Both Inspection (New Licenced), *N* (%)	Facility Not Licenced (At 2018), *N* (%)	New Issue (After Last Inspection), *N* (%)	Before 2023 Not Licenced, *N* (%)
		Before 2018	At 2022	Before 2018	At 2022				
Feni	South-eastern	43	77	35 (81%)	47 (61%)	12 (29%)	08 (19%)	06 (20%)	24 (80%)
Jhalokati	Southern	13	27	11 (85%)	16 (59%)	05 (31%)	02 (15%)	04 (36%)	07 (64%)
Rajshahi	Mid-western	14	58	12 (86%)	21 (36%)	08 (17%)	02 (14%)	06 (16%)	32 (84%)
Cox`s Bazar	South-eastern	30	68	22 (73%)	39 (57%)	17 (37%)	08 (27%)	07 (24%)	22 (76%)

Table 2. Summary of facility`s radiation-monitoring findings by dosage levels for public and occupational workers

District`s Name	Total Facility, *N*	Total Machin, *N*	X-ray Facility Considering Dose Level for Public				X-ray Facility Considering Dose Level for Worker			
			Normal Dose Rate (≤5 µSv/h)		Unsatisfactory Dose Rate (>5 µSv/h)		Normal Dose Rate (≤5 µSv/h)		Unsatisfactory Dose Rate (>5 µSv/h)	
			N (%)	Mean ± SE	*N* (%)	Mean ± SE	*N* (%)	Mean ± SE	*N* (%)	Mean ± SE
Feni	77	93	68 (88%)	(73 ± 7) %	9 (12%)	(27 ± 7) %	56 (73%)	(56 ± 10) %	21 (27%)	(44 ± 10) %
Jhalokati	27	30	16 (59%)		11 (41%)		16 (59%)		11 (41%)	
Rajshahi	58	69	41 (71%)		17 (29%)		18 (31%)		40 (69%)	
Cox`s Bazar	68	89	50 (74%)		18 (26%)		42 (62%)		26 (38%)	

**N* is the number of counts, '%' is the percentage, and 'SE' is the standard error.

Table 1 illustrates the impact of regulatory interventions on facility licensing and compliance over time. Less than half of all radiological facilities for each district were found in the areas where re-inspection was performed. After statistically normalizing the data, the majority of the column in Table 1 shows the value of the count and percentage. During the midterm period of both inspections, more than 73% to 86% of the registered (data from the previous inspection done in 2017-2018) radiological facilities in four distinct districts in Bangladesh were authorized by the competent regulatory authority. On the other hand, we discovered that, 6–10 months after the last surveys, which were conducted in 2022, almost 36% to 61% of facilities had already received their authorizations. Actually, the total number of X-ray facilities is increasing from 100 to 230, which is more than double the number reported in both inspections. Numerous radiological facilities have attempted to obtain licenses following the inspections in 2017–2018 and 2022; in this instance, we calculated that 17% to 37% and 16% to 36% of new facilities, respectively, had applied for authorization. The results indicate a significant issue regarding unauthorized radiological facilities operating without regulatory approval. Specifically, we found that between 14% to 27% of the assessed facilities had not yet submitted licensing applications, highlighting the presence of facilities potentially operating without regulatory oversight. In actuality, the majority of unlicensed radiological facility operators were ignorant of regulatory authorization because of a lack of knowledge or purposefully postponed obtaining licenses. This situation underscores the need for continued and enhanced regulatory efforts to ensure all radiological facilities comply with safety standards and obtain the necessary approvals to operate legally.

Table 2 demonstrates the facilities (count and percentage) in accordance with their radiation-monitoring findings. Regarding the dosage levels, we separated the public dose (maximum value) for radiation at the X-ray room's entrance door or other external areas and the dose (maximum value) for occupational workers who are in close proximity to radiation-generating equipment, which is a major concern from the regulatory point of view. We also distinguished the radiation dose level as normal (less than equal 5 µSv/hr for public) and unsatisfactory because the dose rate exceeded the regulatory limit (greater than 5 µSv/hr for occupational worker) and the shielding in the entrance door and control panel was inadequate. This level is based on the graded approach taken by regulatory bodies, which aim to limit radiation exposure to a level that is considered negligible in terms of health risks over extended periods of exposure. We found that the average normal dose rate for public is about (73 ± 7) % facilities of the four districts while (27 ± 7) % facilities hold the average unsatisfactory dose rate. Where, the Feni and Jhalokati district are engendered the maximum average dose rate for public with normal and unsatisfactory cases, respectively. Furthermore, we discovered that the average normal dose rate for occupational workers in the four districts is approximately (56 ± 10) %, while the average unsatisfactory dose rate is (44 ± 10) %. Thus, the Feni and Rajshahi districts have the highest average daily dose rates for occupational workers with normal and unsatisfactory cases, respectively.

We measured and analyzed the dose rate at different location and recorded the instant highest radiation exposure dose rate in the medical or diagnostic facility. The histograms of maximum values of measured dose rate for both, public and occupational worker with corresponding number of facilities are presented in Fig. 3. The peak of the histogram shifted in the right direction with dose rate (Fig. 3 (A-D)), which can be clearly shown by comparing Fig. 3(A) and Fig. 3(B). The histograms were fitted by the well-known lognormal distribution (17,18). The probability density function for dose rate is as follows:

$$f(D_r) = \frac{1}{D_r}\frac{1}{\sigma\sqrt{2\pi}}\exp\left[-\frac{\{\ln(D_r)-\mu\}^2}{2\sigma^2}\right] \quad (1)$$

where, D_r is the value of the dose rate for each facility, μ is mean and σ is standard deviation. The values of μ and σ were obtained from the fitted curve. The lognormal distribution of the given equation is a skew distribution in which the mean is usually larger than the mode. It is typically used in the description of the distribution along with other phenomena having large data range. So, the lognormal distribution is important in this study because it accurately models the skewed, non-negative, and multiplicative nature of radiation dose rate data, providing a more realistic representation and better statistical handling of the data.

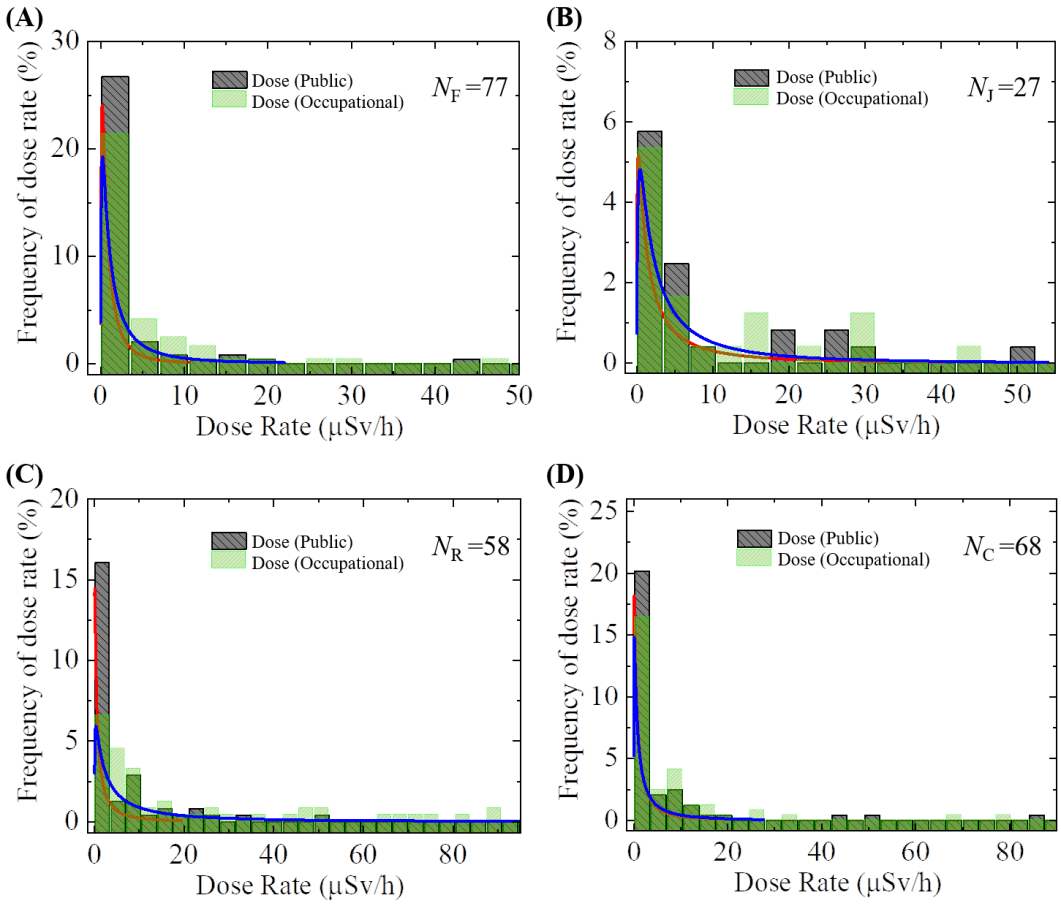

Fig. 3 Dose rate distribution histograms for public (■) and occupational workers (■) of all the inspected facilities in the four districts. (A) Feni (B) Jhalokati (C) Rajshahi, and (D) Cox`s Bazar. *N* indicates the number of facilities in the four distinguished districts, where $N_F$, $N_J$, $N_R$, and $N_C$ refer the total facility number investigated in Feni, Jhalokati, Rajshahi, and Cox`s Bazar, respectively. The best fitting theoretical curves (blue and red lines) for measured dose rate of both, public and occupational worker corresponding to Eq (1).

From the fitted curves (blue and red solid lines), we got the values of μ and σ. Using these values, it was calculated the mean values of dose rate for normal and unsatisfactory radiation exposure of the distribution. As we mentioned above, the mean values with standard error of radiation exposure from the X-ray generating equipment for district wise medical or diagnostic facilities are shown in Fig. 4. For both, public and occupation worker`s mean dose date is illustrated in Fig. 4(A) and Fig.4(B), respectively. We investigated that the normal dose rate for both public and occupational workers of all districts are very much similar to each other. The mean radiation dose rate for public at Cox`s Bazar is higher than other three districts. Again, we measured that the mean radiation dose rate for occupational worker at Rajshahi district more than others. With regards to the dose levels, the patient entrance door and waiting place areas are major source of concern from the regulatory perspective. All the values of mean dose rate with standard error for both public and radiation workers of all facilities in each district are provided in SM1.

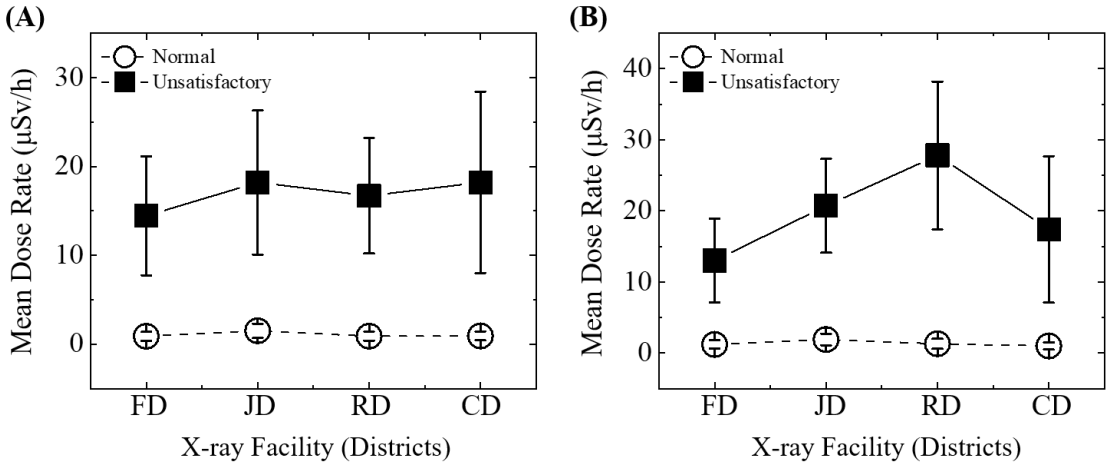

Fig. 4 Mean dose rate for normal (○) and unsatisfactory (■) radiation exposure from all the corresponding inspected facilities in the four districts. (A) Public dose record (B) Occupational worker`s dose record. FD, JD, RD, and CD indicate the district of Feni, Jhalokati, Rajshahi, and Cox`s Bazar, respectively.

Fig. 5 shows the assessment of radiation safety equipment available in all the observed facilities of the four districts. According to the figure, some progress has been made in respect to the availability of accessories especially lead apron, lead thyroid collar, and lead equivalent eye goggles in case of radiation protective equipment, lead hand gloves are not available in any of the facilities. As per national act or regulations and international safety standards these tools are obligatory for the medical and diagnostic practices.

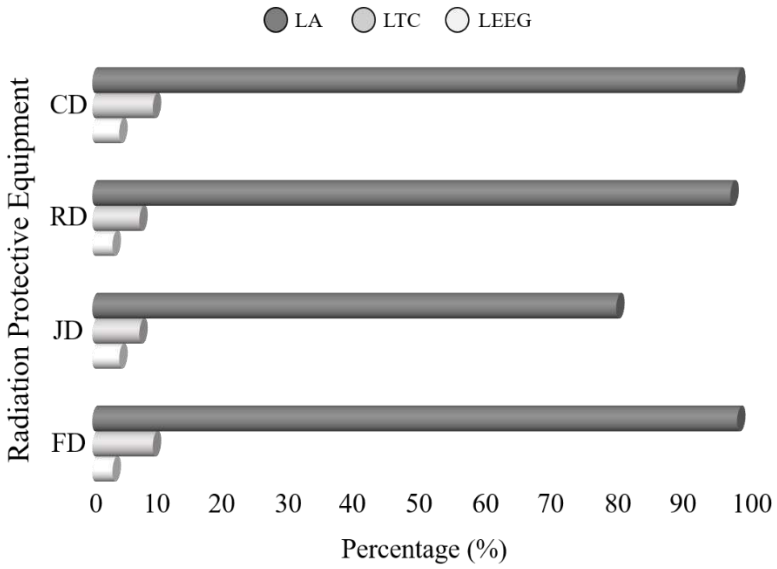

Fig. 5 Assessment of radiation protective equipment in the four districts (FD, JD, RD, and CD indicate the district of Feni, Jhalokati, Rajshahi, and Cox`s Bazar, respectively). LA, LTC, and LEEG indicate Lead Apron, Lead Thyroid Collar, and Lead Equivalent Eye Goggles, respectively. We calculated that almost 96% of facilities, excluding Jhalokati district, have the lead apron, whether they use it or not. However, the findings in the case of lead thyroid collar and lead equivalent eye goggles availability are diametrically opposed. All the data that belongs to radiation safety equipment are provided in SM2.

Now, Fig. 6 illustrates the assessment of radiation shielding availability in all the observed facilities of the four districts. Among the shielding systems for radiation protection, the availability of entrance door shielding, control panel: lead equivalent barriers/mobile lead shields, window shielding, etc. are carefully evaluated. So far, we found that most of the facilities in the four districts have a good percentage of entrance door shielding availability, with Feni showing the highest recognition. However, the medical or diagnostic facilities in the Jhalokati district have a very low number of the entrance door shielding for radiation protection.

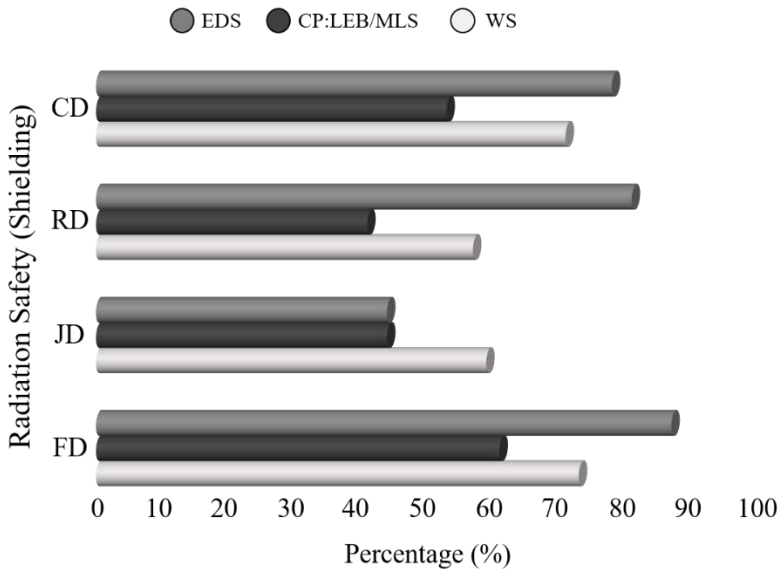

Fig. 6 Radiation shielding assessment in the four districts (FD, JD, RD, and CD indicate the district of Feni, Jhalokati, Rajshahi, and Cox`s Bazar, respectively). EDS, CP: LEB/MILS, and WS indicate Entrance Door Shielding, Control Panel: Lead Equivalent Barrier/Mobile Lead Shield, and Window Shielding, respectively.

We also observed that the shielding scheme for the control panel and window of the X-ray units for radiation safety, the facilities in Feni districts carried higher numbers than others. All the data related to the shielding system for radiation protection are provided in SM2.

In the present study, the availability of some essential radiation safety parameters, such as X-ray room size, warning signal, and wall condition, is inspected. Fig. 7 demonstrates the assessment of the radiation safety parameters. Most of the facilities in all the targeted districts contained a very low number of standard-sized rooms (225 ft^2). Approximately, 75% facilities are below standard, indicating that a significant improvement is required to meet regulatory demands (19). Almost 90% of all X-ray rooms feature a 10-inch brick wall that achieves regulatory requirements and effectually protects against radiation. In Fig. 7, a significant advance is observed in area classification by putting up radiation warning signs, which was not convincing at all before the start of the regulatory process. All the data related to the radiation safety parameters are provided in SM3.

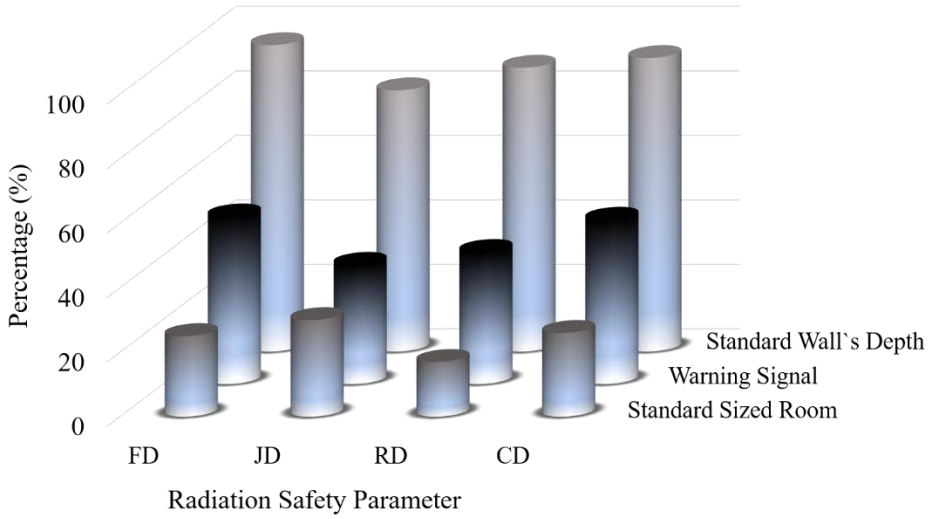

Fig. 7 Indispensable parameters for radiation safety in the four districts (FD, JD, RD, and CD indicate the district of Feni, Jhalokati, Rajshahi, and Cox`s Bazar, respectively).

The status of the radiation monitoring dosimeter and individuals with knowledge of radiation control activities are shown in Fig. 8. TLD badge is a radiation dose measuring device, that enables us to know whether we are working within the safe dose limits prescribed in NSRC rules-1997. We found that about 52 facilities had the TLD badge out of 77 in the Feni district, which was the maximum percentage (33%) of availability of all the other three districts, where Rajshahi exhibits a very low quantity, as shown in Fig. 8(A).

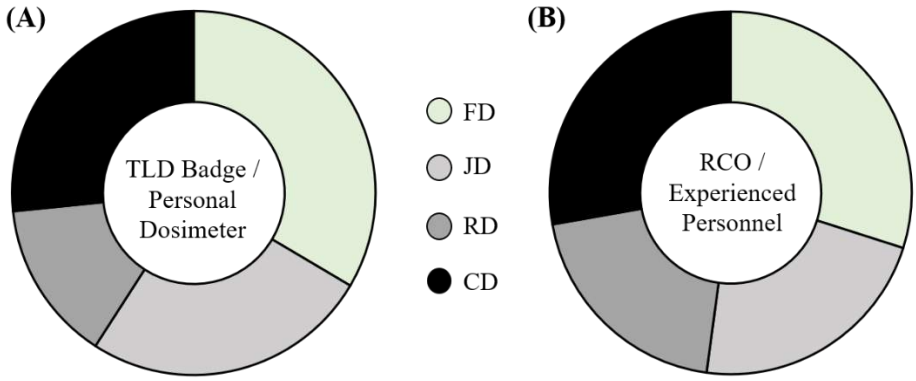

Fig. 8 Status of radiation monitoring equipment and personnel in the four districts (FD, JD, RD, and CD indicate the district of Feni, Jhalokati, Rajshahi, and Cox`s Bazar, respectively). (A) Availability of thermoluminescent dosimeter badge (TLD) or any personal radiation dosimeter (B) Availability of radiation controlling personnel.

We also calculated the availability of the radiation control officer (RCO), who is the central point of reference for radiation protection matters within a medical or diagnostic facility (20), as shown in Fig. 8(B). Feni and Cox`s Bazar districts accounted for 70% and 65% of the availability of such experienced radiation control personnel, respectively. All the data related to the radiation dose storing equipment (TLD) and experienced executive personnel are provided in SM3.

5. DISCUSSIONS

More than 73% of the list of the examined facilities in the four districts were authorized by state`s regulatory authority and accepted based on the national regulations and matched with the standards regulations. The operator of each facility should be familiar with the guidance and documents related to the radiation protection program. The shielding design for the walls and the areas around the entrance to the X-ray room were found to be around 80%, except for Jhalokati district`s facilities. The shielding requirements for the operator console to prevent unnecessary radiation exposure were not sufficient for all facilities. In addition, other protective tool at each facility such as lead glass for window shielding are almost available. The lead apron holder was present in the majority of the facilities that were inspected, but it wasn't always used. Each facility's mobile X-ray machine storage and security were verified to be in good working order. It's critical to note that none of the facilities we inspected had gonad shields or leaded screens as protective barriers. Overall, the examined facilities show moderately good and sufficient shielding conditions based on radiation the NSRC rules-1997 and safety standards (13, 14, 21). In the present report indicated that about 55% of the inspected facilities except Rajshahi district do not have any personal radiation dosimeter such as a thermoluminescent dosimeter (TLD) and most of those facilities do not keep a record for the personal dosimeter reading at their facilities. Only 17-30% of the inspected facilities in the four districts have standard sized room for radiological operations. For the purpose of performing radiation safety and maintenance at those facilities, approximately 55% of the facilities under inspection have radiation control personnel on hand. The majority of technologists are trained through their professional work. For some of them, basic radiation protection training has been offered by the Bangladesh Atomic Energy Regulatory Authority (BAERA). Finally, more than 50% of the examined facilities do not have any warning sign or alarm warning light at their entrance to the room. Despite being present at certain sites, radiation-warning signs were not used by the bulk of the facilities. Following the previous inspections, the radiation technicians or operators in all X-ray facilities generally shown a good awareness of the fundamental guidelines and safety directives in the medical and diagnostic area. According to the data analysis, about one-third of the facilities meet the required radiological safety standards.

6. CONCERNS ON RADIATION PROTECTION AND RECOMMENDATIONS

The primary duty and responsibility of the regulatory body are to conduct inspections for nuclear and radiation-related activities, including the radiological facility in the state (15). According to the United Nations Scientific Committee on the Effects of Atomic Radiation (UNSCEAR), 4.2 billion diagnostic radiographs are produced annually by the X-ray machines that are inspected globally, which makes the radiological survey essential for the inspection of diagnostic radiology equipment (22).

The majority (more than 95%) of the radiation dosage that humans are exposed to comes from medical exposures. Radiation protection is a crucial element of good medical practice. The three radiation protection principles of justification, optimization and dose limitation are enshrined in the IAEA Fundamental Safety Principles (SF-1) and apply to all medical and radiological facilities and activities that give rise to radiation risks (14, 23, 24). The foundations of radiation safety practice are an understanding of external radiation protection measures as well as technical aspects of operating the X-ray system. The three fundamentals of radiation safety to an operator include i.

time, ii. distance, and iii. shielding and dosimeter monitoring (21, 25). Radiation exposure can be accumulated over the time of exposure. The physician must improve his interventional skills, and the radiographer must verify the X-ray at the proper site and time without smudged images in order to reduce the usage time. Operators must maximize their distance from the X-ray source as radiation intensity follows the inverse square law: if an operator maintains a distance twice as far from the source as necessary, they can minimize their radiation exposure not to half but to one-fourth (21, 26). Shielding can be applied externally, personally, or both. The degree of lead equivalence in each form determines how much radiation protection it provides. A lead apron with or without shoulder coverings for breast shielding, lead glasses, thyroid protectors, radiation-reducing gloves, and caps are all examples of personal shielding. Attenuating 95–96% of the scatter radiation, the lead apron should be at least 0.35 mm thick (21, 27). The key principles of protection systems and fundamentals radiation safety for human exposure are summarized in the illustration, as shown in Fig. 9.

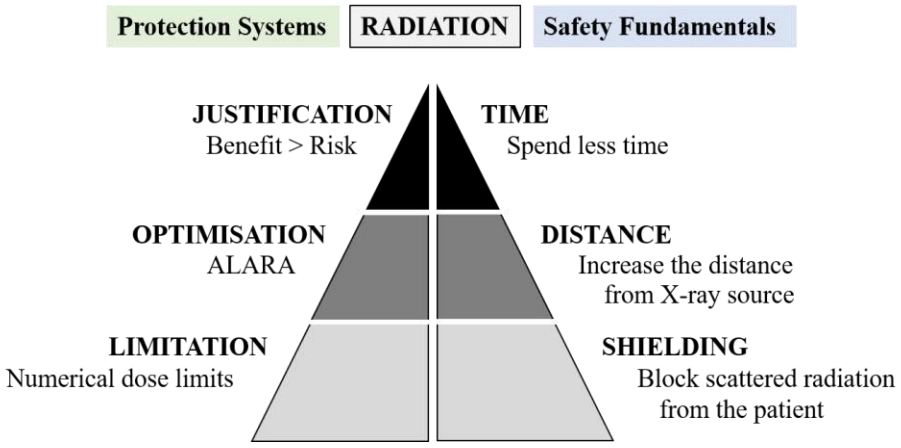

Fig. 9 Illustration of the systems of radiological protection and fundamental rules of radiation safety.

To maintain optimal diagnostic image quality with the least amount of risks and discomfort to patients, every diagnostic X-ray facility is required to have a basic quality assurance (QA) program in place. The executive authority should regularly review this program to evaluate the outcomes of each QA action. Also, it is advisable to identify and include in the quality control (QC) manual all of the various significant components of the monitoring and maintenance tasks.

The medical and diagnostic facilities, with assistance from the Ministry of Health or Directorate General of Health Services (DGHS), Bangladesh, should work with BAERA to ensure complete compliance. Following the complete implementation of the regulations governing radiation protection, a follow-up study should be conducted to evaluate regulatory compliance and the different stakeholders' (administrators, clinicians and other healthcare staff, and the public) awareness of radiation protection and safety. A study that will evaluate room design and the installation of equipment to meet required radiation safety standards is recommended. The provision of additional training opportunities for radiologists or technicians through RCO trainings and workshops run by BAERA should also be taken into account, so they can adequately comprehend the regulations.

7. LIMITATIONS

Out of a possible 350 facilities in the inspected districts, only 230 were visited by the BAERA regulators, making it impossible to confirm the veracity of all respondents' claims regarding the availability of tools and resources. The technologists or technicians could have been biased when reflecting on radiation safety and placing blame on management of the facility. More thorough investigation of the management of the facilities and the maintenance of X-ray generating equipment could be beneficial for future guidelines on the implementation of radiation safety in the radiological facilities.

8. SIGNIFICANCE OF THE RESULTS AND IMPLICATIONS FOR FUTURE WORK

The findings of this study highlight the progress and ongoing challenges in radiation protection within radiological facilities in Bangladesh. The significant reduction in leakage radiation dose rates demonstrates the effectiveness of regulatory inspections and the adoption of safe practices. However, the persistent gap in compliance with licensing requirements underscores the need for more stringent enforcement and greater awareness among stakeholders.

Future directions:

Future work should focus on several key areas to strengthen radiation safety further:

- **Regular inspections:** Increasing the frequency and thoroughness of inspections to ensure continuous compliance and address any emerging safety issues promptly.
- **Enhanced training programs:** Regular, mandatory training sessions for all personnel involved in radiological practices to reinforce the principles of radiation protection and ensure adherence to safety protocols.
- **Technological upgrades:** Investment in modern, safer radiological equipment with better shielding and automated safety features.
- **Public awareness campaigns:** Educating the general public about radiation safety to ensure community support and compliance with safety measures.
- **Policy development:** Revisiting and updating national policies to incorporate the latest international guidelines and best practices in radiation safety.

By addressing these areas, Bangladesh can significantly enhance its radiation safety infrastructure, ensuring the protection of both the public and radiation workers while maintaining the benefits of ionizing radiation in various fields.

9. CONCLUSION

Ionizing radiation, such as X-ray has many beneficial applications in medicine, diagnosis, research, etc. With the increased use of ionizing radiation, safe use policies and practices are required. The lower percentage of leakage radiation dose rate in the examined facilities in the current study indicates comprehension of the concept of justification. A solid understanding of the ALARA principle is indicated by the higher percentage of personnel who maintain the advised safe distance from the radiation generating machine to them. Together with the routine control and

inspection carried out by the executive regulatory authority, radiation protection in this context should also be strengthened by ongoing training, educational procedures, and pertinent information. The majority of medical and diagnostic facilities are currently authorized by BAERA, however despite repeated reminders from the regulatory body to the stakeholders, compliance levels fall short of the standards for license renewal. The radiation safety conditions of the facilities were found to be below the level demanded by national and international standards at the beginning of regulatory functions. If the BAER Act-2012 and the NSRC rules-1997 are correctly put into practice, it will be able to enhance the radiation protection infrastructure in X-ray facilities in the future. These studies provide valuable insights and guidance to enhance radiation safety regulations, ultimately ensuring safer practices and better protection for both the public and occupational workers in medical and diagnostic environments.

ACKNOWLEDGEMENT

The authors would like to thank Atomic Energy Regulatory Authority (BAERA) for providing logistics during the study.

AUTHOR CONTRIBUTIONS

Conceptualization: Md. Kabir Ahamed and Meherun Nahar
Data curation: Md. Kabir Ahamed, Md. Akramuzzaman, and Nadia Akter Mokta
Formal analysis: Md. Kabir Ahamed, Meherun Nahar, and Md. Akramuzzaman
Investigation: Md. Kabir Ahamed and Meherun Nahar
Methodology: Md. Kabir Ahamed, Meherun Nahar, and Md. Akramuzzaman
Project administration: Meherun Nahar
Resources: Md. Kabir Ahamed, Md. Akramuzzaman, and Nadia Akter Mokta
Software: Md. Kabir Ahamed
Supervision: Meherun Nahar
Validation: Md. Kabir Ahamed, Meherun Nahar, and Md. Akramuzzaman
Visualization: Md. Kabir Ahamed and Md. Akramuzzaman
Writing ± original draft: Md. Kabir Ahamed
Writing ± review & editing: Md. Kabir Ahamed, Meherun Nahar, and Md. Akramuzzaman

AVAILABILITY OF DATA AND MATERIALS

The datasets generated and/or analyzed during the current study are not publicly available because they contain materials from unpublished manuscripts but are available from the corresponding authors upon reasonable request.

CONFLICT OF INTEREST STATEMENT

The authors declare that they have no known competing financial interests or personal relationships that could have appeared to influence the work reported in this paper.

REFERENCES:

Burgio, E., Piscitelli, P. and Migliore, L., (2018), Ionizing Radiation and Human Health: Reviewing Models of Exposure and Mechanisms of Cellular Damage. An Epigenetic Perspective, *Int. J. Environ. Res. Public. Health,* vol. 15(9):1971.

Chang, Y. J., Kim, A. N., Oh, I. S., Woo, N. S., Kim, H. K. and Kim, J. H., (2014) The Radiation Exposure of Radiographer Related to the Location in C-arm Fluoroscopy-guided Pain Interventions, *Korean J. Pain.* 27(2):162-167.

Chalkia, M., Arkoudis, N. A., Maragkoudakis, E., Rallis, S., Tremi, I., Georgakilas, A. G., Kouloulias, V., Efstathopoulos, E. and Platoni, K., (2022), The Role of Ionizing Radiation for Diagnosis and Treatment against COVID-19: Evidence and Considerations, *Cells*. 11(3), 467.

Crow, E. L. and Shimizu, Eds., K., (1987), *Lognormal Distributions: Theory and Applications* (1st ed.) New York: CRC Press.

Do, K. H., (2016), General Principles of Radiation Protection in Fields of Diagnostic Medical Exposure, *J. Korean Med. Sci*. 31(1):S6-S9.

Engel-Hills, P., (2006), Radiation protection in medical imaging, *Radiography* (London 1995), 12(2), 153-160.

Heidbuchel, H., Wittkampf, F. H., Vano, E., Ernst, S., Schilling, R., Picano, E., Mont, L., Jais, P., de Bono, J., Piorkowski, C., Saad, E. and Femenia, F., (2014), Practical ways to reduce radiation dose for patients and staff during device implantations and electrophysiological procedures, *EP Eur*. 16(7):946–964.

IAEA, (1996), *International Basic Safety Standards for Protection Against Ionizing Radiation and For The Safety of Radiation Sources*. Saf. Ser. No. 115, Vienna, Austria.

IAEA, (2001), *Radiological Protection of Patients in Diagnostic and Interventional Radiology, Nuclear Medicine and Radiotherapy*. Proceedings Series, Vienna, Austria.

IAEA, (2014), *Radiation Protection and Safety of Radiation Sources: International Basic Safety Standards*. IAEA Safety Standards Series No. GSR Part 3, Vienna, Austria.

IAEA, (2004), *Regulatory Control of Radiation Sources*. IAEA Safety Standards Series No. GS-G-1.5, Vienna, Austria.

IAEA, (2014), *Diagnostic Radiology Physics: A Handbook for Teachers and Students.* Non-serial Publications, Vienna, Austria.

IAEA, (2018), *Establishing the Infrastructure for Radiation Safety*. IAEA Safety Standards Series No. SSG-44, Vienna, Austria.

IAEA, (2018), *Occupational Radiation Protection.* IAEA Safety Standards Series No. GSG-7, Vienna, Austria.

IAEA, (2006), *Fundamental Safety Principles*. IAEA Safety Standards Series No. SF-1, Vienna, Austria.

IAEA, (2018*), Radiation Protection and Safety in Medical Uses of Ionizing Radiation*. IAEA Safety Standards Series No. SSG-46, Vienna, Austria.

IARC Working Group on the Evaluation of Carcinogenic Risks to Humans and World Health Organization and International Agency for Research on Cancer, (2000), *IARC Monographs on the Evaluation of Carcinogenic Risks to Humans.* Ionizing radiation. Part 1, X- and gamma (γ)-radiation, and neutrons, IARC 1999:75 Lyon, France.

ICRP, (1991), *1990 Recommendations of the International Commission on Radiological Protection*. Ann. ICRP, 21(1-3):1-201.

Khamtuikrua, C. and Suksompong, S., (2020) Awareness about radiation hazards and knowledge about radiation protection among healthcare personnel: A quaternary care academic center–based study, *SAGE Open Med.* 8:2050312120901733.

Kim, J. H., (2018), Three principles for radiation safety: time, distance, and shielding, *Korean J. Pain.* 31(3):145–146.

McColl, N., Auvinen, A., Kesminiene, A., Espina, C., Erdmann, F., de Vries, E., Greinert, R., Harrison, J. and Schüz, J., (2015), European Code against Cancer 4th Edition: Ionising and non-ionising radiation and cancer, *Cancer Epidemiol*. 39(1): S93–S100.

Reed, W. J. and Jorgensen, M., (2004), The Double Pareto-Lognormal Distribution—A New Parametric Model for Size Distributions, *Commun. Stat. - Theory Methods*, 33(8):1733–1753.

Republic of Bangladesh Government. Bangladesh Atomic Energy Regulatory Act 2012 No. 19 Bangladesh Gazette (2012).

Republic of Bangladesh Government. Nuclear Safety and Radiation Control Act 1993 No. 21. Bangladesh Gazette (1993).

Republic of Bangladesh Government. Nuclear Safety and Radiation Control Rules-1997 (SRO No. 205-Law/97). Bangladesh Gazette (1997).

Ryu, J. S., Baek, S. W., Jung, C. H., Cho, S. J., Jung, E. G., Kim, H. K. and Kim, J. H., (2013) The Survey about the Degree of Damage of Radiation-Protective Shields in Operation Room, *Korean J. Pain.* 26(2):142-147.

United Nation Scientific Committee on the Effects of Atomic Radiation (UNSCEAR), (2021) *Sources Effects of Ionizing Radiation: Report to the General Assembly*, with Scientific Annexes; United Nation Publications, (A/76/46), 1.

Jurnal Sains Nuklear Malaysia, 2024, 36(No. 1): 62 – 80
ISSN: 2232-0946

DOSE RATE PREDICTIVE MODEL OF TERRESTRIAL GAMMA RADIATION BASED ON SUPERFICIAL-WEATHERED SOIL AND ROCKS: CASE STUDY IN SARAWAK, MALAYSIA

Hairul Nizam Idris[1,2], Mohamad Syazwan Mohd Sanusi[2], Ahmad Termizi Ramli[2], Wan Muhamad Saridan Bin Wan Hassan[2], Mohd Rafi Mohd Solleh[3], Faizal Yahaya[4], Mohd Zaini Ya'cob[3] and Wee Boon Siong[5]

[1]Waste Technology & Environment, Division,
Malaysian Nuclear Agency, Kajang, Bangi, Malaysia
[2]Department of Physics, Faculty of Science,
University Teknologi Malaysia, Skudai, Johor, Malaysia
[3]Faculty of Engineering and Life Sciences,
Department of Science and Biotechnology, University of Selangor, Malaysia
[4]Faculty of Education and Social Sciences,
Departmnet of Social Sciences, University of Selangor, Malaysia
[5]Faculty of Resource Science and Technology,
Universiti Malaysia Sarawak, Kota Samarahan, Sarawak, Malaysia
Correspondence author: hairul_nizam@nuclearmalaysia.gov.my

ABSTRACT

Estimating terrestrial gamma radiation (TGR) levels is crucial for assessing the annual effective dose received by the public due to natural radiation exposure. Cumulative doses from various sources can become significant, warranting a spatial understanding of TGR distribution. Few countries have comprehensively mapped TGR on a national scale, often facing challenges due to remote or inaccessible regions. This study explores the feasibility of estimating TGR dose rates using a linear regression model based on surface-weathered soils and rocks in Sarawak, Borneo, Malaysia. Geological studies reported that a rich diversity of rock types shaped by complex tectonic history can be found in Sarawak, predominantly sedimentary rocks covering 93% of the region, while igneous and metamorphic rocks constitute the remaining 7%. In this study, a total of 1044 TGR dose rate measurements were collected. The measurement ranges from 7 to 320 nGy h-1, with a mean of 100 nGy h-1.. Non-parametric statistical analyses of variance have validated the notable dissimilarities among six categories of superficial-weathered soil and distinguished the two distinct groupings of sedimentary and igneous rocks. The regression analysis produced a model for predicting TGR dose rates (nGy h^{-1}) = 0.992Dsoil – 0.816Drock + 109. The model showed a sufficient linear correlation, with spatial maps generated from in-situ measurements and the regression model displaying similar regional dose rate contours. Semivariogram analysis supported the model's reliability for predicting TGR dose rates in areas with similar geological backgrounds. In conclusion, this study has successfully developed a predictive model for TGR dose rates in Sarawak, based on superficial-weathered soil and rock data. While the model is specific to the Sundaland-Borneo tectonic block, it provides a valuable tool for spatial inference of TGR dose rates in unsampled locations with similar geological characteristics, aiding in radiation exposure assessment and environmental monitoring.

Keywords:Terrestrial gamma radiation, spatial dose mapping, background radiation, soil-rock gamma dose rate.

INTRODUCTION

Baseline data pertaining to regional terrestrial gamma radiation (TGR) levels is vital for estimating the annual effective dose accrued by the public due to natural radiation exposure. Although TGR-induced radiation exposure is typically low, the cumulative dose from various sources, such as medical radiation procedures, impacting the public can be substantial. In this context, the development of a spatial representation of TGR distribution is expected to provide valuable insights for assessing the potential regional public dose stemming from both anthropogenic sources, like nuclear fallout events resulting from accidents or increased nuclear weapon tests (Quindos et al., 1994; Pálsson et al., 2013; Kleinschmidt & Watson, 2015), and terrestrial contaminations associated with technologically enhanced naturally occurring radioactive materials (TENORM) linked to mining industries (AELB, 1991). Moreover, this information about regional populations exposed to radiation also plays a pivotal role in epidemiological risk assessments of diseases with hereditary links to cancer, as well as evaluating health risks associated with heightened background radiation exposure (BEIR VII, 2006; ICRP 103).

Only a handful of countries have successfully executed comprehensive TGR mapping on a national scale. For instance, Canada and the United States have undertaken such mapping endeavors under the guidance of Grasty and LaMarre (2004), Croatia through Mora et al. (2007), Spain as documented by Suarez et al. (2000), Portugal by Batista et al. (2013), Great Britain in the work of Chernyavskiy et al. (2016), Iran through Kardan et al. (2017), European countries as documented in the European Atlas of Radiation Map by Cinelli et al. (2019), China by Feng et al. (2020), and Switzerland through studies conducted by Rybach et al. (2002) and Folly et al. (2021). However, generating a comprehensive TGR distribution map necessitates an extensive in-situ gamma survey conducted on the ground, incurring substantial costs and occasionally proving time-consuming, particularly for geographically inaccessible regions (Ramli et al., 2003; Sanusi et al., 2014). The current study delves into the feasibility of estimating TGR dose rates through a linear regression model based on data from dose rates obtained from surface-weathered soils and rocks in Sarawak, Borneo, Malaysia.

According to the scientific review paper authored by Ahmad et al. (2015), all studies on terrestrial natural radioactivity in Malaysia focused solely on study locations located in Peninsular Malaysia. Meanwhile, Dodge-Wan et al. (2020) stated that previous studies conducted in Borneo were constrained to urban areas. Therefore, a research effort was initiated to carry out a more extensive study on terrestrial natural radioactivity throughout the entirety of the Borneo region in Malaysia, covering Sarawak and Sabah. This paper presents the findings of a study conducted in the state of Sarawak. Another scientific article will be devoted to the region of Sabah.

Sarawak, situated in the northwest of Borneo, constitutes one of the two states comprising East Malaysia, along with Sabah. It encompasses an area of 125,206 km^2, featuring a coastal plain and dissected uplands that can reach elevations of up to 2400 meters. The urbanization zone in Sarawak is predominantly concentrated along the coastlines, where cities and towns have burgeoned as hubs of economic and social activity. However, a significant portion of the region is characterized by vast expanses of dense jungles, highland terrain, and other challenging landscapes that remain largely untouched and shrouded in wilderness. These natural attributes contribute to the diverse and intricate geographical fabric of Sarawak, with urbanization primarily hugging the coastlines while extensive tracts of rugged terrain remain relatively pristine and cloaked in impenetrable wilderness (Agriculture Department Sarawak, 2000).

Jurnal Sains Nuklear Malaysia, 2024, 36(No. 1): 62 – 80
ISSN: 2232-0946

Sarawak has a wide array of rock formation types molded by its intricate tectonic history and diverse types of great soil group, as illustrated in Fig. 1 (a) and Fig. 1 (b) respectively. Most of the region (constituting 93% of the total area) is dominated by sedimentary rocks (116,676 km^2), forming a substantial part of the landscape. These sedimentary rocks, encompassing sandstones, mudstones, and shales, were deposited during various geological epochs, spanning from the Mesozoic to Cenozoic eras. Minor rock formation types (constituting approximately 7% of the total area) in Sarawak include igneous and metamorphic rocks (spanning approximately 8530 km2), contributing to the geological diversity of the region with varieties such as granite, gneisses, and schists. These rock formations were shaped during tectonic events in the Late Mesozoic and Early Cenozoic periods (Department of Mineral and Geosciences Malaysia, 1992).

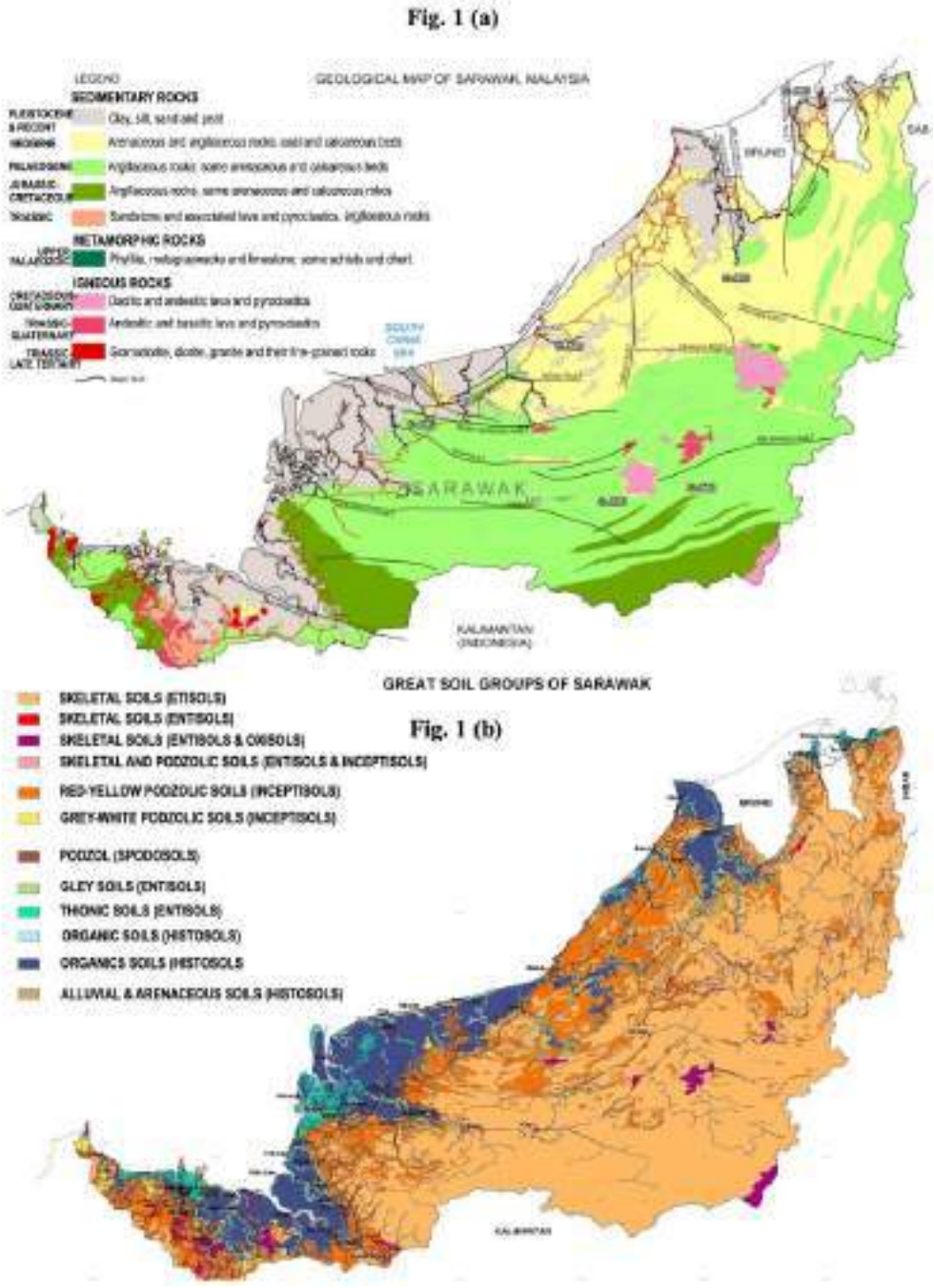

Figure 1 (a) Geological map and **(b)** soil group of Sarawak Borneo (Department of Mineral and Geosciences Malaysia, 1992; Agriculture Department Sarawak, 2000).

MATERIALS AND METHODS

Selection of the TGR survey sites

For the current study, the determination of TGR dose rate survey locations were based on two main sources of information: geological map (Department of Mineral and Geosciences Malaysia, 1992) and soil distribution maps of the Sarawak state (Agriculture Department Sarawak, 2000), as shown in Figure 1. To begin with, all the maps were digitized using ArcGIS ESRI Version 10.5 (Esri, 2017). Subsequently, approximately 1250 survey points were randomly generated, with one survey point per each 100 km², using the digitized tectonic and pedogenesis distribution maps. This procedure was carried out to ensure that the projected TGR survey points adequately covered all the weathered-soil and rock groups. For skeletal-oxisols, podzolic, and sedimentary rock groups, achieving a homogeneous distribution of survey point projections across each block was easily accomplished due to their expansive areas. Conversely, for the igneous group, gley, thionic, alluvial, and organic groups, additional survey points were plotted to ensure a sufficient sample size (above 30 sites) due to their scattered locations and limited coverage. With the assistance of topographic maps, the survey points were aligned with nearby and accessible roads. The proposed points underwent a double-check to remove survey points that may have been incorrectly located in mountainous terrain, dense forests, lakes, or inaccessible areas.

Instrument calibration

The gamma survey meter used was the Ludlum Measurement, Inc. Model 19 Micro R Meter, a scintillation survey meter manufactured in Texas, USA (Ludlum, 1993). This meter's energy detection range encompasses a wide spectrum of primordial gamma (γ) radiation emitters, including the anthropogenic γ emitter ^{137}Cs (Ludlum, 1993). With a low energy detection limit of approximately 60 keV and a typical quantum efficiency of 20–30%, the instrument's energy calibration utilized standard multi-nuclides such as ^{241}Am, ^{57}Co, ^{133}Ba, ^{137}Cs, and ^{60}Co (Ludlum, 1993), resulting in a non-linear energy response curve spanning from 59.54 keV to 1.17 MeV. The performance calibration of the instruments was carried out at the Secondary Standard Dosimetry Laboratory (SSDL) of the Malaysian Nuclear Agency, following the IEC 1017-1:1990 standards (IEC 1017, 1990), the National Physical Laboratory's dose rate meter calibration technique (BCRU, 1981), as well as IAEA Safety Standard Series No. GSG-10 (IAEA, 2018). Calibrations were performed across three exposure ranges: 0–250 μR h^{-1}, 250–500 μR h^{-1}, and 500–5000 μR h^{-1}. The calibration results were expressed in terms of dose rate using a linear equation (Eq. 1) (Sanusi et al., 2017):

$$D = B \times J \times C_f \times 8.7 \text{ nGy } \mu R^{-1} \text{ h}^{-1} \quad (1)$$

In this context, D represents the calibrated dose rate in nGy h^{-1}, B denotes the output reading (μR h^{-1}), and J represents the correction factors for each respective exposure rate range (1.00, 1.03, and 0.96). C_f is the averaged calibration factor derived from the ratio of the true value of the primary standard source to the dose rate of the uncalibrated instrument. In this study, we utilized a ^{137}Cs source emitting at 662 keV and a ^{60}Co source emitting γ energies at 1173 and 1332 keV (with an effective quantum energy of 1250 keV for ^{60}Co). For calibrating the energy dependence of the dose rate meter from environmental γ radiation sources, the British Calibration Service Publication 0811 (BCRU, 1981) has recommended the use of ^{137}Cs (662 keV) and ^{60}Co (1250 keV) as reference gamma sources. In our research, the calculated C_f values using ^{137}Cs and ^{60}Co sources were 0.95 ± 0.05 and 1.49 ± 0.03, respectively, resulting in an average calculated C_f of 1.22 ± 0.27. The acceptable C_f range for dose rate meters, as specified by ISO and IEC standards, lies between 0.8 and 1.2 (Alamares and Caseria, 1995).

To validate against internal background contributions stemming from radioactive contamination within instrument compartments or electronic noise, dose rate responses of survey meters were examined within an underground lead bunker at the Department of Physics, Universiti Teknologi Malaysia. The instruments exhibited zero-dose rate responses from internal background sources. On the cosmic response validation, the survey meters were tested on a fiberglass boat located 3 kilometers off the mainland in the middle of the sea based on technical report by British Calibration Service Publication 0811 (BCRU, 1981). The instruments displayed an inconsistent response, ranging from zero to half of the lowest scale (0 – 1.25 μR^{-1} h^{-1}), indicating weak cosmic photon components and zero response from hadronic muon showers. During fieldwork, manual stripping of the cosmic background was performed to correct the measured TGR dose rates. The measured cosmic radiation contributions (~1.25 μR^{-1} h^{-1}) absorbed dose rate in air at sea level) aligned with the measured cosmic dose rate at sea level in mid-northern latitude areas (3.67 μR^{-1} h^{-1}) (BCRU, 1981; UNSCEAR, 2000). Additionally, some of this background response might stem from gamma radiation emitted by silica material in the fiberglass boat and traces of U and Th series in seawater.

TGR dose rate measurement technique

The TGR dose rate surveys were conducted based on selected survey points during several series of fieldwork. Two instrument units were utilized to measure the TGR dose rates. Four measurements were taken at each survey point using two identical γ survey meters, positioned 1 meter above the flat, well-drained, and open soil surface, away from embankment areas, trees, outcrops, roads, pavements, and concrete foundations. The chosen site area needed to be open and free from tree canopies to avoid sites with a substantial thickness (up to 2–3 inches from the surface) of organic and humus horizon layers (based on USDA taxonomy). Measurements were performed at different spots approximately 5–10 meters apart to capture local variability in the measurements before averaging all the measured dose rate values. The fieldwork surveys were conducted during the dry seasons (March – October in 2016 and 2017) to avoid rainy days. Measurements were primarily taken from midday onwards to allow moist subsurface soil to evaporate (from morning dews) and ensure there was no self-absorption of *h* radiation in moist and wet soil, which could lead to reduced dose rate readings.

Dose rate corrections

The instrument utilized was a NaI-based detector doped with a micromole of thallium, which exhibits an overresponse to scattered and low-energy photons, effectively capturing nearly all photons passing through its crystal geometry. To address the issue of overestimated output generated by the scintillation crystal detector in this study, a correction was applied using an in situ-to-calculated dose rate ratio of 0.86. The calculated dose rates were determined by employing soil-to-air dose conversion factors (DCFs) based on soil activities of the ^{238}U and ^{232}Th series, ^{40}K, and ^{137}Cs at the locations where the in-situ dose rates were measured. These soil-to-air DCFs (measured in nGy h^{-1} per Bq kg^{-1}) were sourced from the study conducted by Sanusi et al. (2021), which utilized the MCNP5 radiation transport package for soil-to-air gamma dose simulations using a large volume of soil source. The values of soil-to-air gamma dose conversion factors used in this study are 0.349, 0.465, 0.034 and 0.067 nGy h^{-1} per Bq kg^{-1} for ^{238}U and ^{232}Th series, ^{40}K, and ^{137}Cs, respectively. In order to obtain a reliable correction factor in terms of statistics, a large sample, including both in-situ and calculated dose rates, is required. This study was conducted in conjunction with three series of fieldwork: 1) Peninsular Malaysia, Borneo region; 2) Sabah; and 3) Sarawak. A total of 468 soil samples were collected and analyzed for their activity levels of ^{238}U and ^{232}Th series, ^{40}K, and ^{137}Cs in the soils using an HPGe gamma spectroscopy system.

A large number of samples is also necessary to ensure a broad range of dose rates, from a few nGy h^{-1} up to 1200 nGy h^{-1}, thus ensuring correction across the full gamma intensity spectrum. The samples were collected randomly with the goal of covering a grid of 1000 km^2 per soil sample, and only one sample was collected at each location. Although Malaysia's total area is 330,345 km^2, this study managed to collect additional samples, especially in anomaly areas, for further study. Each sample, approximately 1.0 – 1.3 kg bulk soil, was collected at a depth of 1 – 2 ft to ensure that the calculated dose rate gives a representative value of the location. Additionally, samples were dug out in flat, well-drained, and open soil surfaces, away from embankment areas, trees, and outcrops, to ensure similar soil types and geological zones that represent an averaged in-situ TGR values of four measurements carried out at the sampling locations. The energy and efficiency calibration of the HPGe was performed using gamma emitters of precisely known energy from mix-multinuclides: ^{210}Pb, ^{241}Am, ^{109}Cd, ^{57}Co, ^{123m}Te, ^{51}Cr, ^{113}Sn, ^{85}Sr, ^{137}Cs, ^{88}Y, and ^{60}Co (Eckert & Ziegler Isotope product, 1232-2).

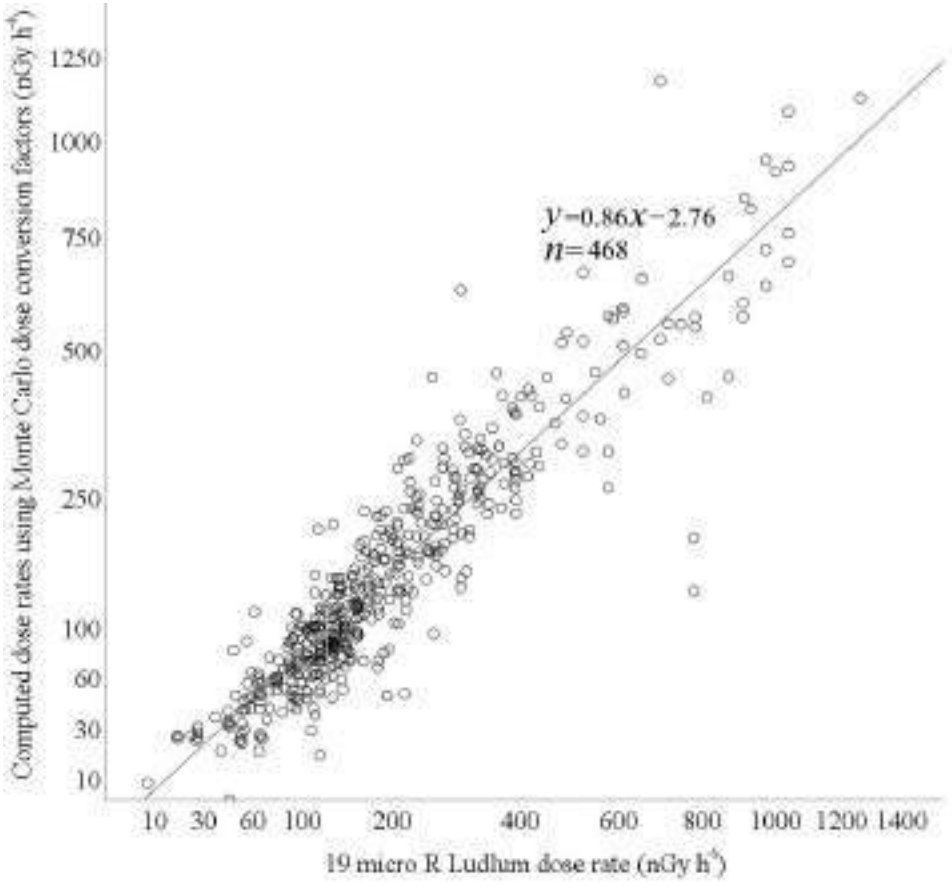

Figure 2 Survey meter dose rate correction factor of 0.86 derived from plots of Ludlum dose rates against the computed dose rates.

Figure 2 illustrates the fitted-line plots ($y = 0.86x + 2.76$ nGy h^{-1}) for instrument correction dose rates, based on computed dose rate plots compared to measurements from a Ludlum survey meter with a range of 19 micro-R. The fitted equation was employed to correct the previously overestimated dose rate readings from the Ludlum survey meter, thereby validating the gamma survey meter's suitability for assessing the high-energy range of 1332 keV to 2614 keV emanating from the ^{238}U and ^{232}Th series and ^{40}K present in the soils.

Statistical test and linear regression mode

Normality and hypothesis tests

In this study, both the Kolmogorov-Smirnov (K-S test) and the Shapiro-Wilk test (W test) were employed to numerically assess the normality distribution of the measured TGR data. Note that statistical hypothesis tests such as ANOVA-F cannot be conducted on data that does not adhere to the principles of a normal Gaussian distribution and homogeneity of data variance. Therefore, in such cases, only non-parametric tests are applicable for hypothesis testing. In this research, the statistical hypothesis tests of Welch-ANOVA, Brown-Forsythe, and Kruskal Wallis were used to examine the significant differences between each weathered soil group and geological rock groups.

Linear regression analysis

This study employed regression analysis to explore a linear model for TGR based on soil and rocks information, with the aim of quantifying the strength of the correlation between these two variables. The results obtained from this model will be used for predicting values at unsampled points. The general multiple linear regression model used is as follows:

$$y = \beta_0 x_0 + \beta_1 x_1 + \ldots\ldots\ldots + \beta_p x_p + \varepsilon = \sum_{j=0}^{p} \beta_0 x_0 + \varepsilon \quad (2)$$

where y is the dependent variable (the predicted dose rates). The regression coefficient (β_0, β_1,…..,β_p) in equation 2 are estimated from;

$$D = X\,\beta \pm \varepsilon \quad (3)$$

where β represent the slopes of the linear relationships between the independent variables x_o, x_1, ……, x_p (in this study, the mean dose rates for soil, D_{soil} and rock groups, D_{rock}) and the dependent variable y. D is the vector of observed dependent variable values (in this case, the measured dose rates) with a residual ε of a random error. X is the 2 × 2 matrices of independent variables, where each column represents a different survey point and each row represents a different independent variable (i.e. D_{soil} and D_{rock}) as follows (de Smith et al., 2007);

$$X = \begin{pmatrix} Dsoil_1 & Dsoil_2 & Dsoil_3 \ldots\ldots & Dsoil_{1044} \\ Drock_1 & Drock_2 & Drock_3 \ldots\ldots & Drock_{1044} \end{pmatrix} \quad (4)$$

where $D_{soil\ i}$ represents the scalar value of mean dose rate of any soil group at survey point i while $D_{rock\ I}$ represents the scalar value of mean dose rate of any geological rocks at survey point i. This matrix represents the mean doses contributed by soil and rock (from Table 1) at each of the 1044 survey points. The goal of fitting the linear regression model is to estimate the regression coefficients β that minimize the sum of squared differences between the predicted values of y (based on X and β) and the actual observed values of D (Abdullah, 1994). The percent contributions of the obtained prediction regression factors β for soil and rock impacts are calculated as follows:

$$\text{Percent contribution } \beta = \left(\frac{SS_i}{\sum SS}\right) \times 100\% \quad (5)$$

where, SS represents the squares term.

Spatial mapping of TGR

To assess the reliability of the developed dose rate predictive model, this study employed geospatial analysis through the semivariogram from the Kriging technique, comparing it with the spatial mapping of TGR dose rates obtained through in-situ measurements. The Ordinary Kriging (OK)

technique was utilized using the ESRI GIS mapping software ArcGIS to map both sets of data: (a) in-situ TGR dose rates and (b) estimated dose rates based on the developed predictive model. The Universiti Teknologi Malaysia (UTM) holds a perpetual license for ESRI ArcGIS Desktop version 10.5 (Esri, 2017). In essence, the core concept of OK involves predicting values at unsampled points by calculating a Kriging weighted average of nearby measured values, utilizing spatial autocorrelation analysis among the sampled data points. In this study, the Kriging process encompassed two key steps: a spatial covariance analysis of the sampled points was conducted by fitting a variogram, and subsequently, the weights derived from this covariance analysis were applied to interpolate dose rates at unsampled locations across the study areas. All TGR data, both observed in-situ and predicted, underwent a log transformation using the Geostatistical Wizard tool in ArcGIS. The Approximation Method option was employed to enhance the accuracy of dose rate calculations and simplify the modelling process, addressing the skewed nature of the data distribution. The ordinary Kriging was initiated with a Multiplicative Skewing Modifier set to 1, and the Base Distribution was configured as Lognormal.

RESULTS AND DISCUSSION

As shown in Fig. 3, a total of 1044 TGR dose rates were measured in this study. The TGR measurements ranges from 7 to 320 nGy h^{-1} with a mean dose rate of 100 nGy h^{-1}. Notably, the lowest TGR dose rate was observed in the peaty and organic soil zone as indicated by the blue color in the soil profile on the map (Fig. 1b), while the highest recorded dose rate, (>300 nGy h^{-1}), was associated with skeletal soil (orange colour of soil profile in (Fig. 1b). The descriptive statistics results were tabulated in Tables 1 for both variables. As shown in Table 1, the mean dose rates of measured TGR in the sedimentary and igneous are 133 ± 8 and 99 ± 1 nGy h^{-1}, respectively, whereas the mean dose rates for the weathered soil groups; skeletal (entisols), podzolic, gley, thionic, alluvial, and organic are 126±1, 96±1, 77±2, 70±4, 65±4, 40±3 nGy h^{-1}, respectively.

Table 1 Descriptive statistics of measured TGR dose rate (nGy h^{-1}) based on weathered soil group and geological rock information.

Descriptive stats.	Soil groups						Geology	
	skeletal soils (entisols)	podzolic soils	gley soils (gleysols)	thionic soils	alluvial soils	organic soils	Sedimentary	Igneous
n	448	317	130	36	30	83	1007	37
Mean ± SE	126±1	96±1	77±2	70±4	65±4	40±3	133±8	99±1
C.I. mean (95%)	123–129	94–99	73–81	61–78	57–73	34–46	116–150	97–102
Min – max	50–320	40–210	15–170	17–165	37–150	7–105	50–200	7–320
Std. deviation	30	26	22	25	21	27	51	37
Kurtosis	4	1	2	6	8	-1	4	-0.4
Skewness	0	0	0	2	2	1	1	-0.2

SE is standard error.
CI is confidence interval.

The results of TGR dose rate measurements from this study are comparable with the TGR measurements conducted by Lai et al. (1999) in Brunei, a neighboring country located to the north-east of Sarawak state. Lai et al. (1999) found that the TGR dose rates were in the range of 15–45 nGy h^{-1} for recent development soils (alluvial and organic soils) and in the range of 45 nGy h^{-1} and higher than 60 nGy h^{-1} for the sedimentary region (skeletal soil). The results from numerical tests of Kolmogorov-Smirnov and Shapiro-Wilk (P-sig.=.000) confirm that the distribution of data sampling for most groups does not follow the Gaussian normality curve. As shown in Table 2, the results from all non-parametric ANOVA (Welch-ANOVA, Brown-Forsythe, and Kruskal Wallis) indicated that the hypotheses of having similarity in mean values of TGR dose rates for each pair of weathered soil groups and 1 pair in geological rock group are rejected. The P-sig. values of 0.000 mean less than 1 in 1,000 chances of observing the identical mean rank between two different groups.

Table 2 Non-parametric ANOVA tests for statistical verification of TGR dose difference for geological and soil influence.

Hypothesis test	Geology / Soil types	Statistic[a]	Sig.
Welch	Igneous-Sedimentary	15.604	.000
	Skeletal Soils &Oxixsols - Red-Yellow/Grey-White Podzolic Soils & Podzols-Gley Soils - Thionic Soils - Alluvial and Arenaceous Soils- Organic Soils	202.858	.000
Brown-Forsythe	Igneous-Sedimentary	15.604	.000
	Skeletal Soils &Oxisols - Red-Yellow/Grey-White Podzolic Soils & Podzols-Gley Soils - Thionic Soils - Alluvial and Arenaceous Soils- Organic Soils	244.751	.000
Kruskal Wallis	Igneous-Sedimentary	16.549	.000
	Skeletal Soils &Oxisols - Red-Yellow/Grey-White Podzolic Soils & Podzols-Gley Soils - Thionic Soils - Alluvial and Arenaceous Soils- Organic Soils.	517.626	.000

a. Asymptotically F distributed

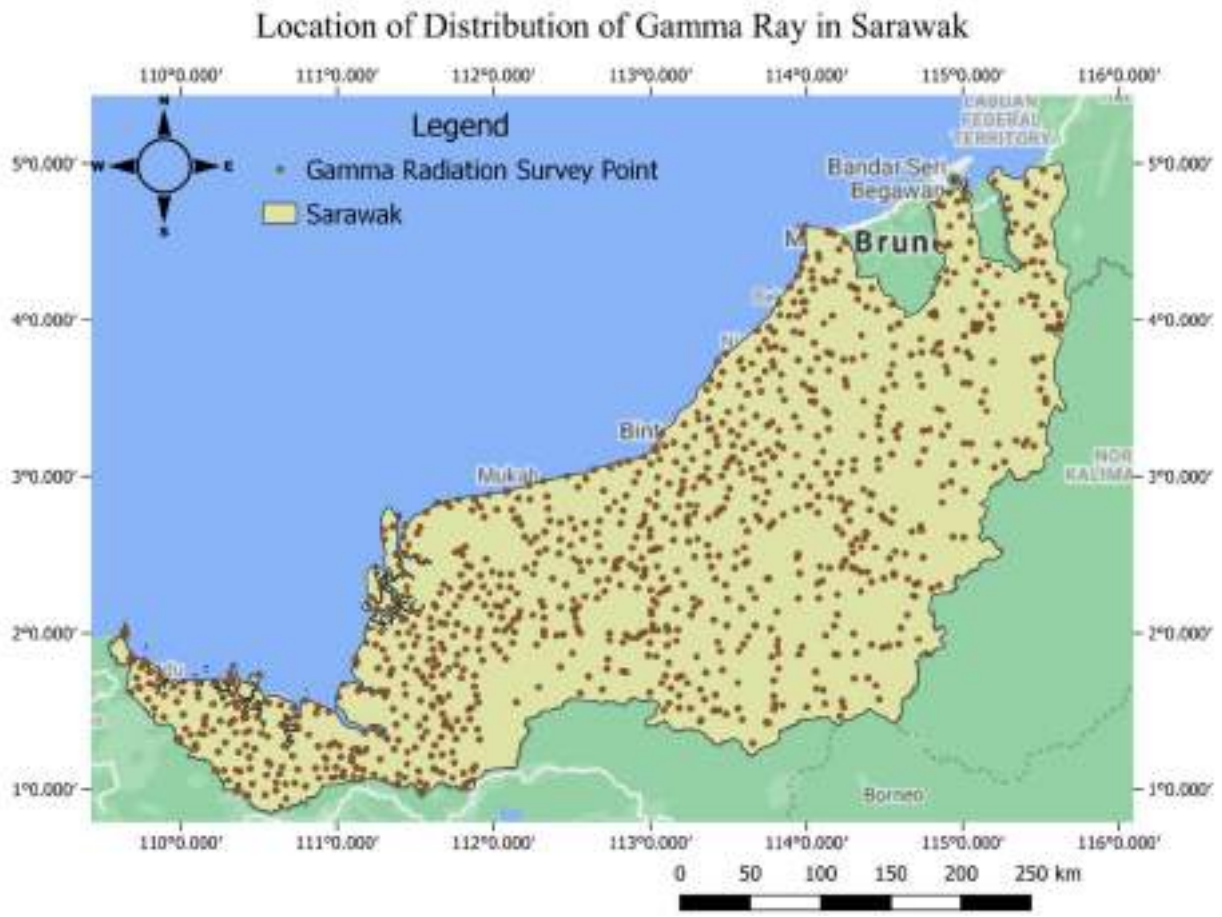

Figure 3 Distribution of TGR survey points (dots) in Borneo Sarawak.

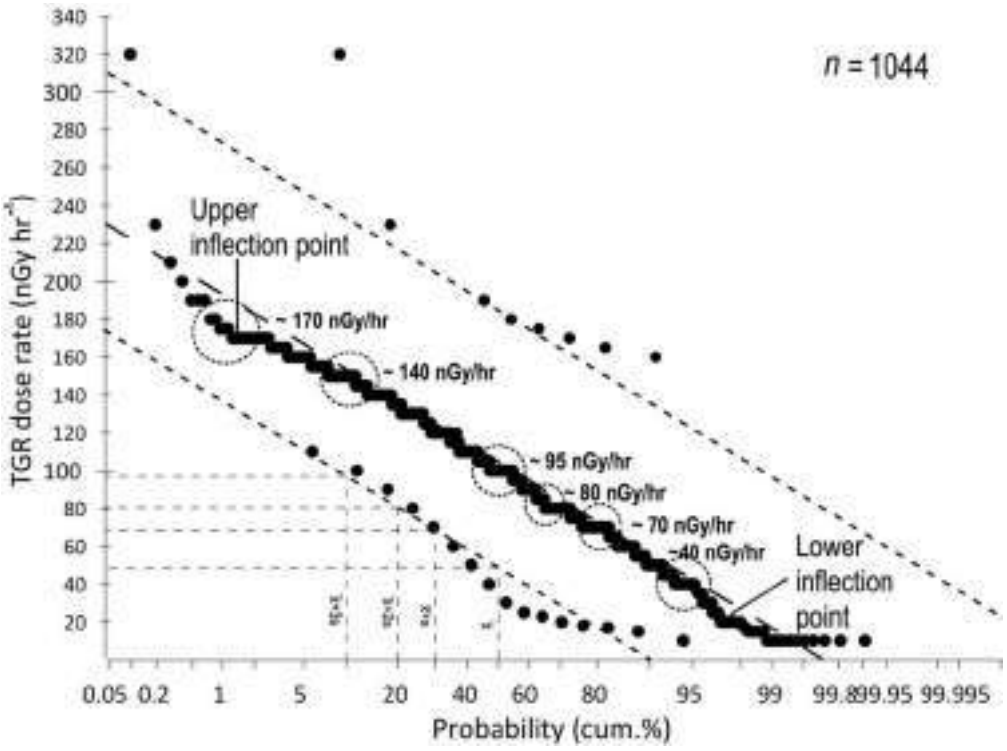

Figure 4 Sinclair's technique for cumulative probability plots of measured TGR surveys.

Figure 4 shows the graphical analysis using Sinclair's technique to examine a cumulative plot using Sinclair's technique was employed to examine the distribution of TGR dose rates across the study area. The Sinclair cumulative plot is a method commonly used in geochemistry (rare earth element, REE and other element geo-explorations) to visualize the cumulative frequency distribution of a variable (e.g. concentration of REE in sediments), in this case, TGR dose rates. The plot displays the cumulative percentage of measurements below a certain dose rate threshold on the y-axis, plotted against the dose rate threshold on the x-axis. Ideally, in a Sinclair cumulative plot, the data points would fall along a straight line, indicating a uniform distribution of dose rates. However, deviations from this straight line, as observed in our plot, suggest the presence of distinct TGR ranges at specific dose rate intervals. In our study, deviations were noted at intervals corresponding to 40, 70, 80, 95, 140, and 170 nGy h^{-1}, indicating the presence of distinct geological or environmental factors influencing TGR levels at these points. Furthermore, deviations beyond 170 nGy h^{-1} may suggest anomalous TGR readings, which could be attributed to extreme weathering processes or the accumulation of uranium-thorium-bearing heavy minerals such as zircon, ilmenite, monazite, and cassiterite, as reported in previous studies (Teh and Julius, 2002; Yokoyama et al., 2015; Hall and Breitfeld, 2018).

The differences in the mean values and variance distributions from the statistical results have numerically verified the impacts of superficial-weathered soils and geological rocks on TGR dose levels. The mean CIs in Table 1 shows that the sedimentary (116–150 nGy h^{-1}) has a higher dose rate compared to igneous (97–102 nGy h^{-1}). Unlike the igneous granitic batholiths of Peninsular Malaysia (Banjaran Titiwangsa), the Borneo's igneous existed in isolated zones primarily consisting of extrusive types i.e., dacitic, andesitic, basalts, granodiorite, and diorite. The existence of these extrusive volcanic rocks, including mafic plutonic types (e.g., granodiorite and diorites), has been identified to contain lower radioactivity compared to plutonic rocks due to their moderate acidic geochemical properties, low density, low SiO_2 content, and physical darkness in color (NCRP, 1987; Schlumberger, 1982; Azman, 2005).

Skeletal soil (entisols) shows the highest mean dose rate and CI (123–129 nGy h^{-1}) owing to its limited development and weathered products. The layers comprise unweathered parent material, such as rocks and gravel of sedimentary rocks with little or no organic matter accumulation (Agriculture Department, Sarawak 2000). This preserved the most abundant uranium (U) and thorium (Th) in the soil body compared to other weathered soil groups. The mean C.I of 123–129 nGy h^{-1} is slightly lower than the mean CI dose rate of sedimentary and metamorphic soil found in Peninsular Malaysia (152–162 nGy h^{-1}) (Sanusi et al., 2017) owing to its sedimentary content (arenaceous and calcareous) of the continental crust of Sundaland whereas the latter are from the terrane blocks derived from Gondwana which is associated with voluminous S-type granitic batholiths and belts.

Podzolic soils show the second-highest mean dose rate and CI (94 – 99 nGy h^{-1}) due to its partial association of parent materials. The soil is characterized by its moderate weathering processes and leaching process of upper horizon layers. The soil sometimes remains undifferentiated from the entisols or skeletal soils due to their similar lithological setting and the degree of parent material association (Agriculture Department, Sarawak 2000). Similarly, gleysols and thionic soils share comparable means (77 and 70 nGy h^{-1}, respectively) and CI of dose rates (73–81 and 61–78 nGy h^{-1}, respectively) due to their similarities in terms of high waterlogged conditions and anaerobic environments (FAO-UNESCO, 1974; Agriculture Department, Sarawak 2000).

These characteristics promote continuous and alternating mineral leaching conditions, including the U and Th nuclides and K from the soil bodies. As expected, the alluvial and organic soils indicate low dose rate ranges (CI range 34–73 nGy h^{-1} for both groups) owing to their rapid hydrolysis

weathering process, leading to the breakdown of NORM minerals and various physicochemical changes, alterations in texture, and porosity. Contrastingly, the transported soil bodies (alluvial or riverine soils) usually show high dose rates owing to the U and Th sedimentation process by a transported agent of water (watercourse or river) from the uphill granitic ranges to the downhill alluvial soil zones (Sanusi et al., 2014, 2017). However, due to lower U and Th nuclide series and K activities in the uphill sedimentary (skeletal) parent materials compared to the Peninsula's uphill granitoids, the impact of U and Th sedimentation is insignificant for the study area. The organic soils (CI range 34–46 nGy h^{-1}) are expected to have insignificant contribution to high doses owing to the soil's decomposed organic materials mainly from plants, which continuously degraded and solidified by heat and wind. Since most of these organic soil settings are located along the coastal plains, estuaries, and floodplains, the U and Th are expected to be diluted and dispersed by the water bodies.

Table 3 The linear regression model of TGR dose rate based on weathered soil groups and geological rock groups.

Model		Unstandardized Coefficients		Standardized Coefficients		
		B	Std. Error	Beta	*t*	Sig.
1	(Constant)	108.576	17.915		6.061	.000
	rock	-.816	.132	-.133	-6.161	.000
	soil	.992	.031	.697	32.219	.000

a. Dependent Variable: dose

As shown in Table 3, we chose the unstandardized regression coefficients (β coefficients) to represent the prediction model or direct change based on raw values (or original units) instead of standardized coefficients, which express the relative effects in terms of standard deviations or regardless of original units. The TGR dose rate predictor model consisted of one positive predictor variable (0.992 for weathered soil) and one negative predictor variable (-0.816 for geological rocks). A negative beta coefficient is observed suggests an inverse relationship between the predictor (geological rocks) and response variables (TGR dose rate), holding soil variable constant. The developed linear independent variable model based on the estimator coefficients (dependent variables) can be expressed as;

$$\text{TGR dose rate (nGy h}^{-1}) = 0.992D\text{soil} - 0.816D\text{rock} + 109 \quad (5)$$

where 109 nGy h^{-1} is a constant.

Table 4 Residual analysis of the linear model using Pearson's test (*R*) and Durbin-Watson's autocorrelation test

Model	R	R Square	Adjusted R Square	Std. Error of the Estimate	Change Statistics					
					R Square Change	F Change	df1	df2	Sig. F Change	Durbin-Watson
1	.717[a]	.514	.513	26.516	.514	550.281	2	1041	.000	1.340

a. Predictors: (Constant), soil, geo
b. Dependent Variable: dose

To assess the precision of the linear model, the auto-correlation tests based on Durbin-Watson's and Pearson's R tests were performed using the model residuals (errors). The results in Table 4 show that the calculated R-value is 0.717 whereas Durbin-Watson's statistic is 1.34. R is a multipole correlation coefficient and represents the strength of the association between the two variables. Weathered soil and rock variables shared values of 0.717, thus indicating a sufficient linear correlation. Meanwhile, Durbin-Watson value 1.34 indicated a positive correlation among residuals, thus exhibiting a systematic pattern of positive relationships.

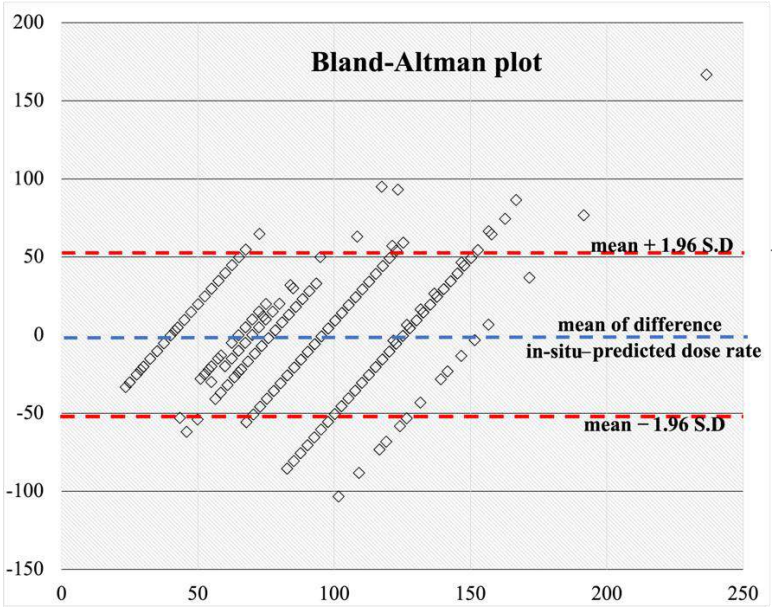

Figure 5 A Bland-Altman plot presents a direct comparison based on the mean differences of in-situ dose rates (in-situ - predicted) against the average values.

For a more direct comparison of in-situ dose rates against the predicted dose rates based on the developed regression model, a Bland-Altman plot was presented in Fig. 5. This plot illustrates the mean differences of in-situ dose rates (in-situ - predicted) against the average values between in-situ and predicted dose rates. For this purpose, all data were log-transformed to achieve a more normally distributed distribution. As depicted in Fig. 5, the average difference (or bias) obtained is -0.49 (indicated by the blue dashed line), with upper and lower limits of agreement (LOA) of 51.43 and -52.42, respectively. Most of the plots demonstrate good agreement, with approximately 95% falling within ±2 standard deviations (σ). In regions below the lower LOA, where negative values occur, the predicted dose rates appear to be overpredicted compared to the measured in-situ dose rates. Conversely, outliers above the upper LOA suggest that the predicted dose rates are underestimated compared to the in-situ dose rates. Based on this comparison, it is expected that approximately 95% of the differences between in-situ and predicted dose rates will fall within the limits of agreement.

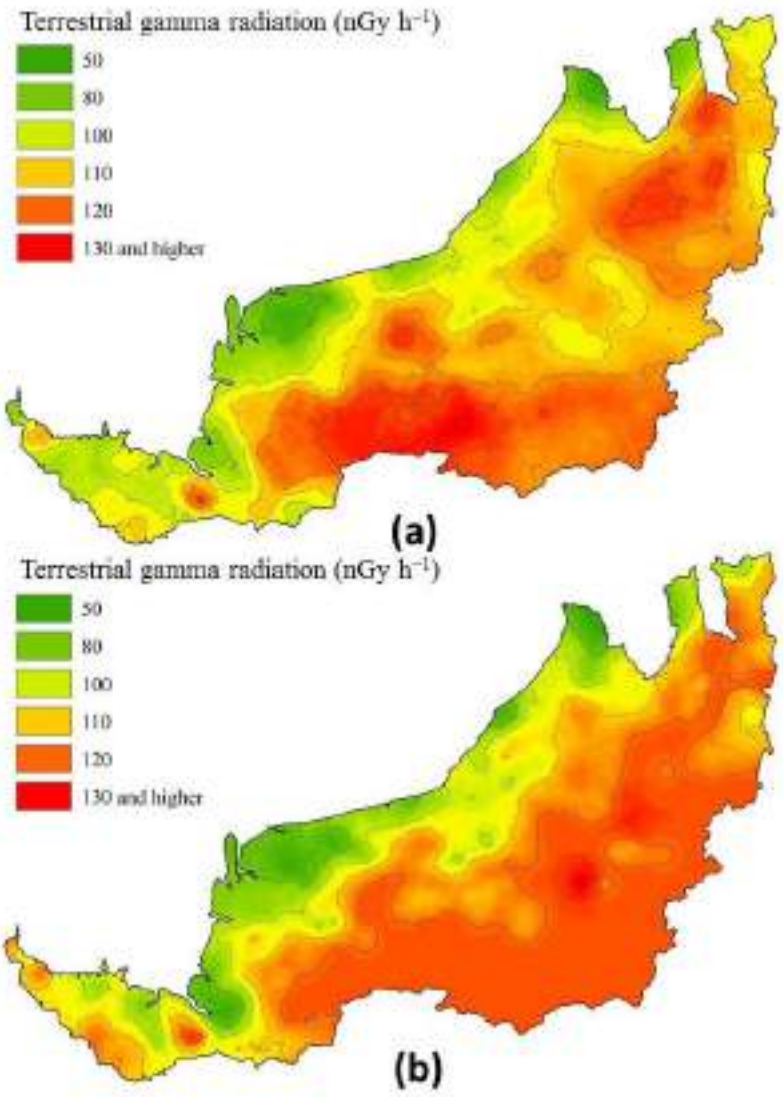

Figure 6 Distribution of TGR dose rates in Borneo Sarawak based Ordinary Kriging of (a) in-situ TGR dose rate and (b) linear regression dose predictive model.

Figure 6 shows two spatial maps of TGR dose rates developed based on: (a) in-situ TGR dose rate and (b) linear regression dose predictive model. Graphically, the maps showed similarities in terms of regional dose rate contour, where50 nGy h^{-1} to 100 nGy h^{-1} dose rate dominated the coastal and recent rock developments i.e. Quaternary and Pleistocene age of rock regions (gleysols, thionic, alluvial, and organic), whereas the upper dose rate range 110 – 320 nGy h^{-1} dominated the sedentary formation (e.g., skeletal and podzolic). To analyze the variability of these spatial maps, two semivariogram plots analysis were given in Fig. 7.

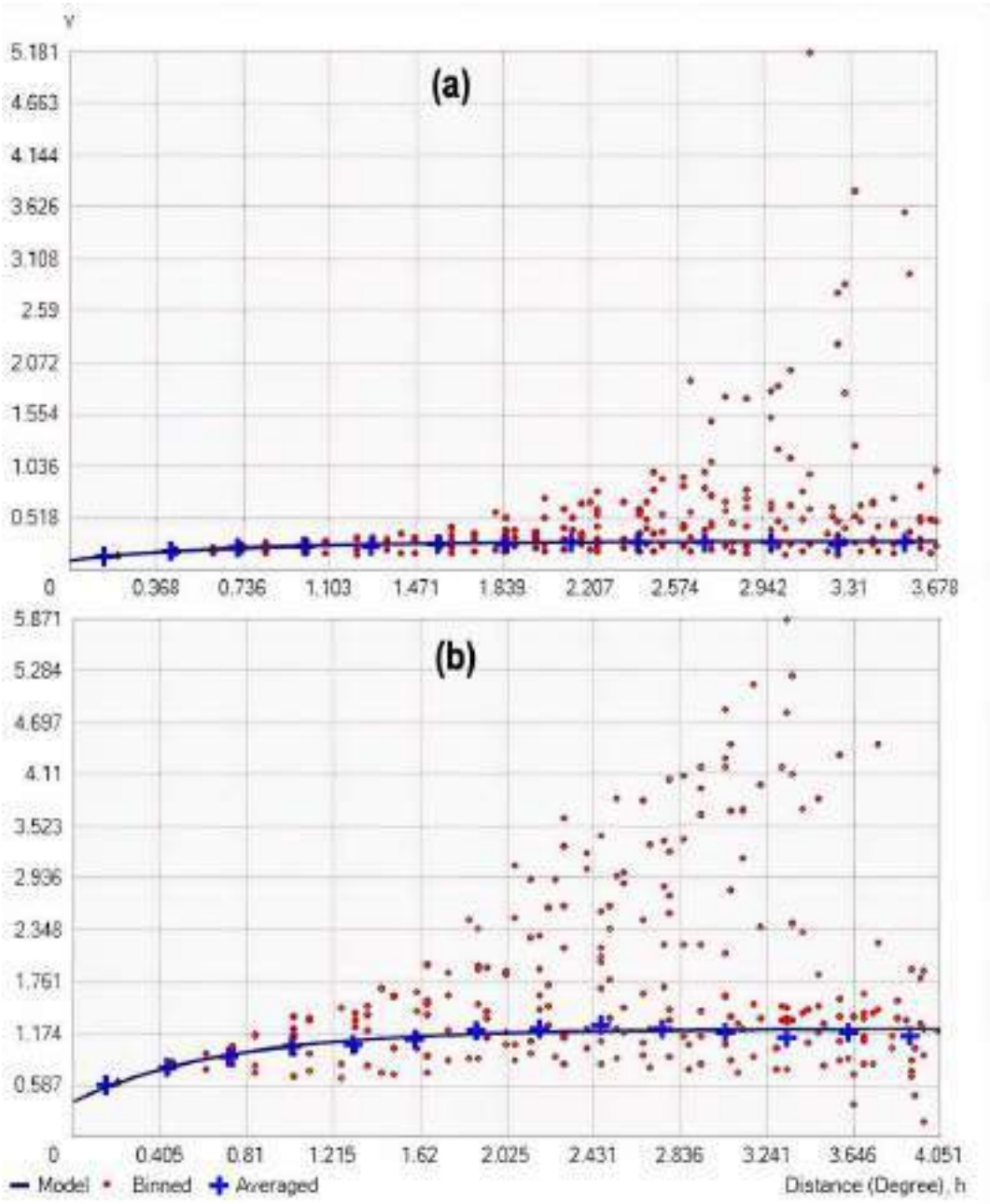

Figure 7 Semivariogram model of Kriging interpolation for comparison between (a) in-situ and (b) predicted TGR dose rates.

The semivariogram model based on a linear regression predictive model suggests that the correlation between data points decreases and eventually becomes flat (i.e., no longer correlated) at a distance of approximately 1.62 degrees. In contrast, the in-situ data indicates that the correlation between data points decreases and becomes flat at a distance of around 1.47 degrees. Comparable sill and nugget values indicated from both semivariogram plots suggest that the developed regression prediction model provides an adequate estimator for TGR dose rate prediction. Such prediction and its consistent variation are considered acceptable at environmental levels, allowing one to build an empirical, methodological basis for spatial inference. The presented model also applicable for long-term use and will not be affected by heavy rainfall and flood. For tropical climates, soil develops slowly over millions of years, and the weathering process by rain, flood, and climates may require a long time to alter the U, Th, and K distribution in soil bodies (Sanusi et al., 2017).

CONCLUSION

The study has successfully developed a regional predictive model for TGR dose rate based on information of superficial-weathered soil and rocks using linear regression model. Statistical non-parametric analyses of variance confirmed that 6 groups of weathered soils are significantly different to each other as well as two distinctive groups of sedimentary and igneous rocks. The model expressed as TGR dose rate (nGy h^{-1}) = $0.992D_{soil} - 0.816D_{rock} + 109$ only applicable for TGR dose rate for similar rock and soil types of Sundaland-Borneo. tectonic blocks of Sundaland-Borneo. Even though the model predicting the unsampled values based on the random process of sampled or nearby points (this is somehow not certainly true for any random sampled environmental data), however, it is somewhat acceptable and permits one to build an empirical methodological basis and insights for the spatial inference of TGR dose rate levels in unmeasured locations based on similar weathered soil and rock types.

ACKNOWLEDGEMENTS

This research received support from the e-Science Fund (03-01-06-SF1277) by the Ministry of Science, Technology, and Innovation, Malaysia, as well as the Fundamental Research Grant Scheme (FRGS) FRGS/1/2019/STG02/UNISEL/03/1 from the Malaysian Ministry of Higher Education. We would like to extend our sincere gratitude to the Department of Mineral and Geosciences Malaysia, Nuclear Agency Malaysia, and Universiti Teknologi Malaysia for their invaluable facilities and support. Special thanks are also due to Mr. Arbaani Akum for his assistance during fieldwork.

REFERENCES

Abdullah, M., 1994. Regression Analysis, 1st Edition. Dewan Bahasa dan Pustaka, Kuala Lumpur

AELB, 1991. Radiological hazards assessment at mineral processing plants in Malaysia. Atomic Energy Licensing Board of Malaysia. LEM/LST/ I6, Internal Report [In Malay].

Agriculture Department Sarawak, 2000. Great soil groups of Sarawak. Agriculture Department Sarawak, Kuching, Sarawak.

Ahmad, N., Jaafar, M. S., Bakhash, M., & Rahim, M., 2015. An overview on measurements of natural radioactivity in Malaysia. Journal of radiation research and applied sciences, 8(1), 136-141.

Alamares and Caseria (1995). Proceeding of the IAEA/CRA workshop on calibration of dosimeters & survey instrument for photons. Japan Atomic Energy Research Institute, 28 November – 2 December 1994, Tokai, Japan.

Azman, A.G. 2005. Geochemical characteristics of S- and I-Type Granites: Example from Peninsular Malaysia granites. Geological Society of Malaysia Bulletin 51, 123–134.

Batista, M.J., Torres, L., Leote, J., Prazeres, C., Saraiva, J., Carvalho, J. 2013. Carta Radiométrica de Portugal (1:500 000) 978-989-675-027-5, Laboratório Nacional de Energia e Geologia Governor de Portugal.

BCRU, 1981. A Guide to the Measurement of Environmental Gamma-ray Dose Rate. British Committee on Radiation Units and Measurements. National Physical Laboratory, United Kingdom, 7, 9, 0.

BEIR VII, 2006. The Biological Effects of Ionizing Radiation VII. *Health risks from exposure to low levels of ionizing radiation*. Washington, D.C.: The National Academy of Sciences.

Chernyavskiy, Kendall, G.M., Wakeford, R., Little, M.P., 2016. Spatial prediction of naturally occurring gamma radiation in Great Britain. J. Environ. Radioact.,164, 300-311.

Cinelli, G., Tollefsen, T., Bossew, P., Gruber, V., Bogucarskis, K., De Felice, L., De Corta, M., 2019. Digital version of the European Atlas of natural radiation. J. Environ. Radioact 196, 240–252

De Smith, M. J., Goodchild, M.F. dan Longley, P.A. 2007. Geospatial analysis: a comprehensive guide to principles, techniques and software tools; regressions method in Chapter 5; data exploration and spatial distribution. pp 239-241. Leicester: The Winchelsea press.

Department of Mineral and Geosciences Malaysia, 1992. Geological map of Sarawak. Department of Mineral and Geosciences Malaysia, Kuala Lumpur, Malaysia.

Dodge-Wan, D., & Mohan Viswanathan, P., 2021. Terrestrial gamma radiation dose rate mapping and influence of building materials: case study at Curtin University campus (Miri, Sarawak, Malaysia). Journal of Radioanalytical and Nuclear Chemistry, 328(1), 163-180.

Esri, 2017. ArcGIS Desktop: Release 10.5. Redlands, CA: Environmental Systems Research Institute.

FAO-UNESCO, 1974. United Nations Educational, Scientific and Cultural Organization. FAO/UNESCO Soil map of the world. Paris: UNESCO.

Feng,W., Zhang, Y., Li, Y., Wang, P., Zhu, C., Shi, L., Hou, X., Qie, X., 2020. Spatial distribution, risk assessment and influence factors of terrestrial gamma radiation dose in China. J. Environ. Radioact 222, 106325.

Folly, C.L., Konstantinoudis, G., Mazzei-Abba, A., Kreis, C., Bucher, B., Furrer, R., Spycher, B.D., 2021. Bayesian spatial modelling of terrestrial radiation in Switzerland. J. Environ. Radioact 233, 106571.

Grasty, R.L., LaMarre J.R., 2004. The annual effective dose from natural sources of ionising radiation in Canada. Radiation Protection Dosimetry. 108 (3):215 – 26.

Hall, R and Breitfeld, H.T., (2018). The eastern Sundaland margin in the latest Cretaceous to Late Eocene: Sediment provenance and depositional setting of the Kuching and Sibu Zones of Borneo. Gondwana Research 63, pp. 34 – 64.

IAEA GSG-10 2018. Prospective Radiological Environmental Impact Assessment for Facilities and Activities. IAEA Safety Standards Series No. GSG-10. International Atomic Energy Agency, Vienna.

ICRP 103, 2007. Recommendations of the international commission on radiological protection. In: International Commission on Radiological Protection ICRP Publication 103, Annals of the ICRP 37. Pergamon Press, Oxford.

IEC 1017 (1990), International Electrotechnical Commission. Portable, transportable, or installed X or gamma radiation ratemeters for environmental monitoring. Part 1: Ratemeters. IEC Standard 1017, Geneva (1990).

Kardan, M.R., Fathabdi, N., Attarilar, A., Esmaeili-Gheshlaghi, M.T., Karimi, M., Najafi, A., Hosseini, S.S., 2017. A national survey of natural radionuclides in soils and terrestrial radiation exposure in Iran. J. Environ. Radioact. 178–179, 168–176.

Kleinschmidt, R., and Watson, D., 2016. Terrestrial gamma radiation baseline mapping using ultra low-density sampling methods. J. Environ. Radioact.,151 (3), 609-622.

Lai, K.K., Hu, S.J., Minato, S., Kodaira, K., and Tan, K.S. (1999). Terrestrial gamma ray dose rates of Brunei Darussalam. Applied Radiation and Isotopes. 50 (3), 599-608

Ludlum, 1993. Instruction Manual of Ludlum Model 19 Micro R Meter. Ludlum Measurements, Inc, Texas.

Mora P., Picado, E., Minato S. 2007. Natural radiation doses for cosmic and terrestrial components in Costa Rica. App. Radiat. Isot. 65 (1), 79-84.

NCRP. National Council on Radiation Protection and Measurements 1987. Exposure of the Population in the United States and Canada from Natural Background Radiation. NCRP Report No. 45.

Pálsson, S.E., Howard, B.J., Bergan, T.D., Paatero, J. Isaksson, M. dan Nielsen, S.P. 2013. A simple model to estimate deposition based on a statistical reassessment of global fallout data. J. Environ. Radioact., 121, 75 – 86.

Quindós, L.S., Fernández, P.L., Soto, J., Ródenas, C., dan Gómez, A.J. (1994). Natural radioactivity in Spanish soils. Health Phys. 66 (2), 194–200.

Ramli, A.T., Abdul Rahman, A.T., Lee, H.M., 2003. Statistical prediction of terrestrial gamma radiation dose rate based on geological features and soil types in Kota Tinggi district, Malaysia. Appl. Radiat. Isot. 59 (6) 393 – 405.

Rybach, L., B¨achler, D., Bucher, B., Schwarz, G., 2002. Radiation doses of Swiss population from external sources. J. Environ. Radioact. 62 (3), 277–286.

Sanusi, M.S.M, Ramli, A.T., Said, M.N., Izham, A., Lee, M.H., Heryanshah, A., dan Wagiran, H. 2017. Assessment of impact of urbanisation on background radiation exposure and human health risk estimation in Kuala Lumpur, Malaysia. Environ. Int. 109, 91 – 101.

Sanusi, M.S.M., Ramli, A.T., Gabdo, H.T., Garba, N.N., Heryanshah, A., Wagiran, H., Said, M.N., 2014. Isodose mapping of terrestrial gamma radiation dose rate of Selangor state, Kuala Lumpur and Putrajaya, Malaysia. J. Environ. Radioact. 135, 67 – 74.

Sanusi, M.S.M, Hassan, W.M.S.W., Hashim, S., Ramli, A.T. (2021). Tabulation of organ dose conversion factors for terrestrial radioactivity monitoring program. Appl. Radiat. Isot. 174, 109791.

Schlumberger, 1982. Natural Gamma Ray Spectroscopy: Essentials of N.G.S. Interpretation. (unspecified).

Suarez, E., Fernandez, J. A., Baeza, A., Moro, M. A., Garcı´a, D., Pozo, J. M. and Lanaja, J. M. (2000). Proyecto MARNA. Mapa de radiacio´n gamma natural. INT-04.02 (Madrid:CSN).

Teh, G.H., and Julius, D.O.A. (2002). EPMA study of heavy minerals in the Annah Rais-Bayur area, Sarawak. Bulletin of the Geological Society of Malaysia 45. Geological Society of Malaysia Annual Geological Conference 2002.

UNSCEAR, 2000. United Nations Scientific Committee on the Effects of Atomic Radiation. Report to the general assembly. Annex B: exposures from natural radiation sources. (NY: UNSCEAR), ISBN-10: 9211422388 (2000).

Yokoyama, K., Tsusumi, Y., Bong, W.S.K., (2015). Age distributions of monazites in the Late Cretaceous to Late Eocene turbidite from northwestern Borneo and its tectonic setting, Bull. Natl. Mus. Nat. Sci., Ser. C, 41, pp. 29–43.

Jurnal Sains Nuklear Malaysia, 2024, 36(No. 1): 81 – 98
ISSN: 2232-0946

MODIFICATION OF SILANE-MODIFIED TIO_2 NANOPARTICLES WITH APO-NANOPARTICLES AS AN ANTIMICROBIAL ADDITIVE FOR PALM OIL-BASED SURFACE COATINGS

Rida Tajau[1]*, Mohd Sofian Alias[1], Nurul Huda Mudri[1], Farah Fadzehah Hilmi[1], Sharilla M. Faisal[1], Rosley C. Ismail[1], Abdul Muizz Mohd Sani[1], Cik Rohaida Che Hak[2], Wilfred Sylvester Paulus[2], Jong Bor Chyan[3], Pauline Liew Woan Ying[3], Hing Jan Nie[3], Nur Nasuha Mat Rapi[4] and Nur Nabila Halipah[5]

[1]Synthesis and Radiation Curing Group (KSPS),
Radiation Processing Technology Division (BTS),
[2]Material Technology Group (MTEG), Industry Technology Division (BTI),
[3]Agrotechnology and Biosciences Division (BAB), Malaysia Nuclear Agency
(Nuklear Malaysia), Bangi, 43000 Kajang, Selangor.
[4]Faculty of Science and Technology,
Universiti Sains Islam Malaysia (USIM), 71800, Nilai, Negeri Sembilan.
[5]Faculty of Applied Sciences, Universiti Teknologi MARA (UiTM),
Cawangan Perlis, Kampus Arau, 02600 Arau, Perlis.
*Correspondence author: rida@nm.gov.my

ABSTRACT

The resources for palm oil in Malaysia are readily available, renewable, and have lower operating costs than any petrochemical oil resource. In this work, silane-modified anatase titanium dioxide (TiO_2) nanoparticles (NPs) were hybridized with acrylated palm olein (APO) (NPs) synthesized by ionizing acrylic palm oil resin to develop an antimicrobial additive for surface coating applications. The effects of their incorporation on the palm oil film coating's layer as well as the physicochemical characteristics of the hybrid APO and TiO_2 organic-inorganic NPs composites were investigated. The results included compatibility, chemical properties, morphology, roughness, water contact angle, thermal stability, transmittance, hardness, crosslinking and anti-scratch effects on coating surfaces. The test coating sample, POBUA-IPDI, presented a slightly higher adhesion and good crosslinking density, which improved hydrophobicity, thermal stability, and anti-scratch properties. This could be ascribed to a greater surface tension between the molecular forces of an object and the composite resin in the presence of TiO_2-APO NPs compared to other coatings. Antimicrobial features were minimal due to the coating sample's TiO_2 low content of 1%. On the other hand, the microbial inhibition zone can be detected due to the natural hydrophobic nature of palm oil and the chemical cross-linking capabilities of coating products after exposure to UV radiation that limit growth or do not allow microbial attachment surrounding the coating layer's surface. The study's findings demonstrated that a palm oil composite coating product by using TiO_2 as a nanofiller can improve the product's thermal, mechanical, and antimicrobial properties and has the potential to be employed as a surface protective layer.

Keywords: APO nanoparticles, EPOLA, POBUA, radiation curing, TiO_2 nanoparticles

INTRODUCTION

Research studies on the development of palm oil-based materials are being conducted to accommodate the country's varied industrial sectors. Inter-industry nuclear technology that advances palm oil resin research through the use of radiation technology, such as gamma, electron beam (EB), and ultraviolet (UV) for the production of multi-functional products, particularly in the field of surface coating.

Over the last two decades of research, it has been discovered that the effect of irradiation on palm oil materials can improve the physiochemical, thermal, and mechanical properties of these new products in order to meet their specifications and applications in industrial and healthcare demands. Indeed, its value as a renewable material compared petrochemical-based products makes it one of the primary plant oil sources for advanced research (Stavila, 2023). Furthermore, as compared to thermal or other conventional processes, nuclear technology utilized as an advanced material processing technique is more environmentally friendly, resulting in lower greenhouse gas (GHG) emissions.

On the other hand, titanium dioxide (TiO_2) nanoparticles (NPs) also known as titania is one of the nanofillers that are biocides and widely employed in the industrial sector, including the production of nanocomposite materials that guarantee to improve the original physiochemical, thermal, and mechanical properties of the material. Many studies reveal that the presence of TiO_2 NPs in a material can endow it with antimicrobial property. In addition, TiO_2 NPs also has unique features, such as non-toxicity, easy UV-activation, chemical stability, environmental friendliness, inertness, corrosion resistance and, low cost harvesting which has made it one of the choices as an antimicrobial agent.

Medical, food and beverage, building and construction, textile, and other industries have the highest demand for antimicrobial coatings (Zhao, 2011; Mamat Rokhmat, 2017; Abbas, 2018; falco, 2018; Kartini, 2018; Baig, 2020; Tran, 2020; Tudu, 2020; Chuang, 2021; Kumaravel, 2021). Anti-microbial coatings are classified into two types: biocides (which include silver, copper, titania and zinc compounds) and resin (which includes acrylic, polyurethane, epoxy, polyester, and others). Anti-microbial additives or biocides can enhance qualities that includes dimensional stability, heat and chemical resistance, and chemical stability while preventing the growth of microbes in finished products or polymers.

The pitfalls and challenges in this current sector are the potentials for the development of antibiotic resistance, strict regulations, and health concerns with biocide use. The better choice is to use natural polymers with the conjunction with radiation curing technologies. The palm oil-based resins, such as acrylic- and polyurethane-types are actively being developed for surface coatings of wood, paper, and metal applications because they are environmentally friendly and less harmful. Whereas, radiation curing technology is a green technology because it can offer less or zero volatile organic compounds (VOCs) release to the environment as compared to traditional methods (Salih, 2012; Tajau, 2013; Tajau, 2014; Salleh, 2016). Figure 1 represents the various type of resin-coated substrates, such as glass, paper, and wood.

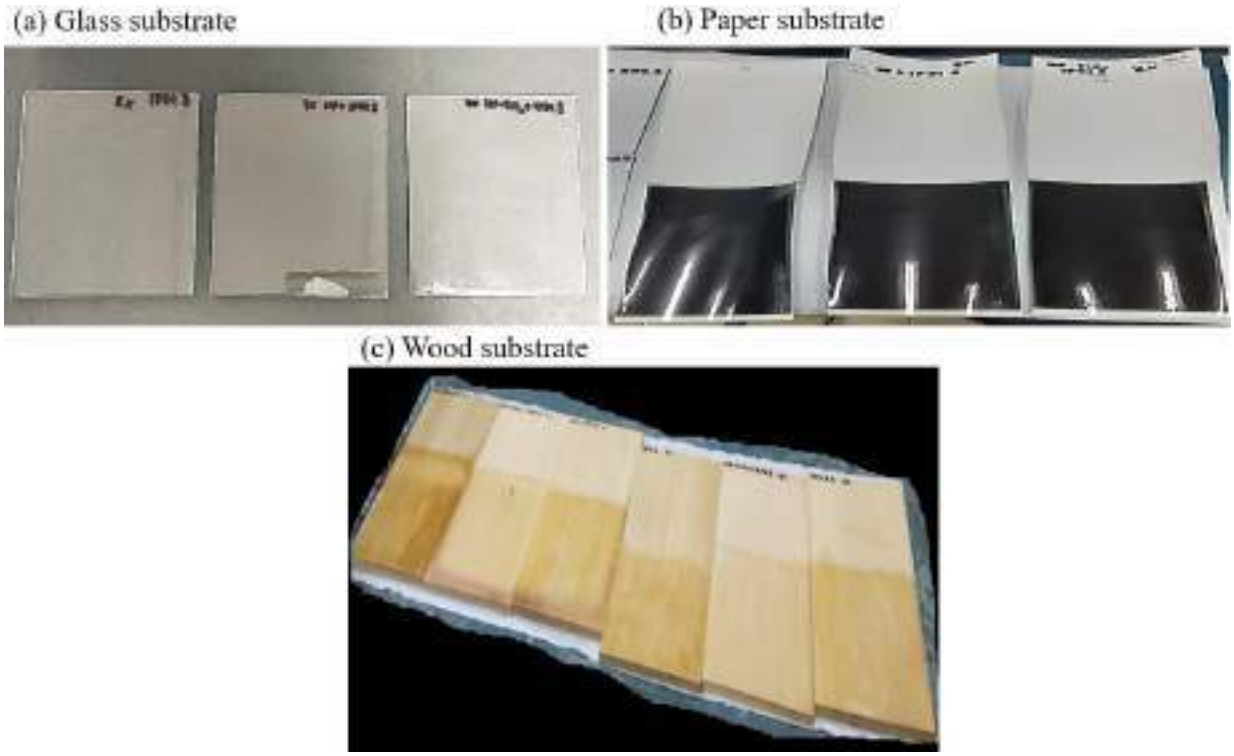

Figure 1 The potential application of coating products on various surfaces: **(a)** glass **(b)** paper and **(c)** wood substrates

The study aimed to develop anti-microbial additives for use in surface coatings. The work focuses on the encapsulation of titanium oxide (TiO_2) with NPs made of acrylated palm oil (APO), which also serves as nanocarriers for anti-microbial agents (Chouirfa, 2019; Tajau, 2021). These NPs will be integrated with palm oil-based resins for use as an antimicrobial additive in surface coatings by using radiation curing technology (Li, 2006; Ingrosso, 2015; Vuong, 2020).

METHODOLOGY

Preparation of UV Curable Organic/Inorganic Hybrid Coating

The sol-gel method was used to prepare the hybrid coatings. APO NPs of 5 mg with titanium dioxide (TiO_2-APO NPs) were each weighed in a 20 mL flask. Ethanol of 5 mL were added to each flask. The TiO_2-APO NPs solution was sonicated for 2 h. After that, 5 mL of resins respectively from the acrylic, i.e., EPOLA (Mw = approximately 2,000 Dalton) and the polyurethanes (Mw = approximately 5,000 Dalton) i.e., POBUA-IPDI, POBUA-IPDI-PETIA and POBUA-TDI-HEA were prepared in four different flasks. Two set of samples for each resin were prepared. About 1 wt% of TiO_2-APO NPs solution was added to the first set of each resin and the another set of resin was prepared without addition of a nanofiller for comparison purposes. Then, all samples were sonicated for 1 h.

Radiation curing process

The formulated resin was cured by using UV irradiation with a medium pressure mercury vapor lamp of IST-UV Dryer (Switzerland) about 7.0 mA and 10 m/min per pass with 0.72 J/cm^2. The sample was coated on the glass, wood and paper substrate by using 40 μm thickness hand bar coater for product evaluation.

Characterization of UV Curable Organic/Inorganic Hybrid Coating

Physical and chemical properties testing

The coating films performance was tested by using the Byk labotron pendulum hardness tester (Konig Method) in accordance with DN 53157 for hardness test. The coating films underwent scratch resistance test by using Erichsen universal scratch tester (model 413) according to DIN 53799 and the cracking property of the film were analyzed by an optical microscope (Zeiss Primo Star) for examining the surface of the films. The direct tape test method was used in this study for adhesion testing on the paper substrate according to the ASTM D3359-09 Test Method B Cross Cut Tape Test. The optical contact angle (Biolin Scientific, TL 100) was utilized to determine the hydrophobicity of the coating. The transmittance of the coating films was analyzed by using Byk Haze-Gard I Haze Meter according to the ASTM D1003; D1044. An FTIR spectrophotometer (Bruker's Tensor II) was used to analyze the chemical functions. The gel content test also was conducted by using soxhlet extractor method (Salih, 2012). The X-ray diffraction (XRD) spectra were obtained using a PANalytical PW3040/60 X'Pert PRO (Netherlands). The TiO_2 NPs chemical composition was characterized using FESEM equipped with an energy dispersive X-ray (EDX) (Oxford instrument).

Thermal testing

The thermal decomposition property of the designated NPs was analyzed by using the thermogravimetric analysis (TGA) analyzer (model NETZSCH) (German) at a temperature range of 35 °C to 900 °C and heated at a rate of 10 °C/min in a nitrogen gas atmosphere.

Morphology analysis

The FESEM images were captured by using a Zeiss microscope (model Philips XL40) and analyzed at the voltage range of 1 kV. The surface roughness was analyzed by using the atomic force microscopy (Nanowizard II).

Antimicrobial testing
The coating film was contaminated with standard strains of gram-negative bacteria (Escherichia *coli* –code of ATCC 25992) provided. ATCC 25922 is a recommended reference strain for antibiotic susceptibility testing. Inhibition zones were analyzed after 24 h incubation of plates at 37 °C.

RESULTS AND DISCUSSION

Physicochemical Properties

Chemical interaction

The study's raw materials were EPOLA and POBUA resins, which were later modified to create EPOLA and polyurethane coatings (Figure 2, a-b). The surface of the TiO_2 nanoparticles was altered by using silane precursors via the sol-gel process before being encapsulated by the APO NPs (Horkavcová, 2021; Mahltig, 2018; Cotolan, 2016). Figure 2a shows the reaction mechanism of the sol-gel approach for silane-modified TiO_2 modification and the interactions between organic-inorganic hybrid coatings between those particles and APO nanoparticles (Figure 2, c-d).

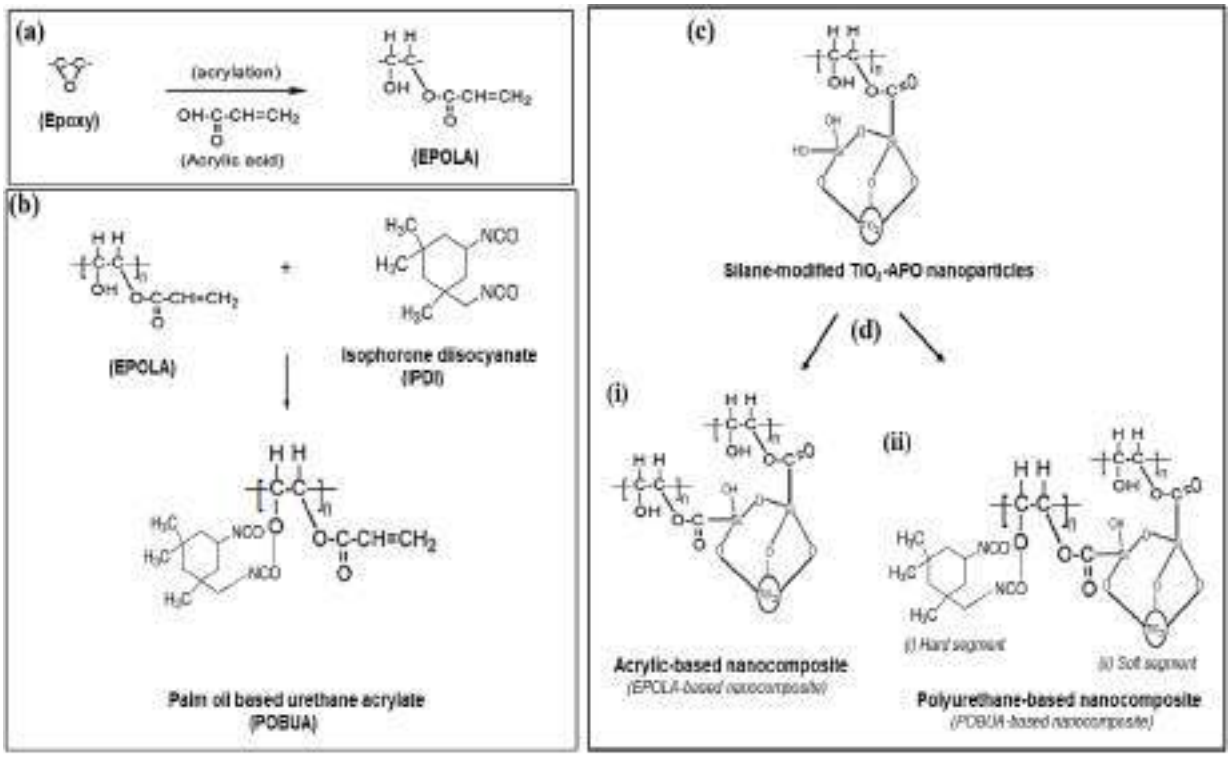

Figure 2. Chemical synthesis route for the production of palm oil-based resins based on the patent innovation registration number: **(a)** EPOLA production (PI2016704907) and **(b)** POBUA production (MY-142814-A), and schematic diagram of chemical structure interaction for development of TiO_2-APO NPs and the acrylic-type composite resin: **(c)** Silane-modified TiO_2-APO nanoparticles and **(d)** organic-inorganic hybrid composite of the TiO_2-APO NPs with the coatings: **(i)** acrylic-based nanocomposite and **(ii)** polyurethane-based nanocomposite

FTIR analysis and Nano-TiO_2 content evaluation

The chemical functional group of carbonyl and ester (C=O), carbon double bond (C=C), ester (-C-O), hydrocarbon (-C-H), and TEOS are the key indicators used to evaluate the curing process in coatings. The infrared tests results showed the resolution of ATR FTIR of the resins and films/ coatings as displayed in Figure 3, and the results are summarized in Table 1. The reaction between the -OH group of silane-modified TiO_2-APO NPs with the acrylic and urethane ester groups respectively showed a decrease in peak intensity at carbonyl 1,720 cm^{-1} and 1,722 cm^{-1} (Figure 2d, i-ii and Figure 3, a-b). Furthermore, as demonstrated in Table 1, the occurrence of cross-linking reactions has resulted in a decrease in the peak intensity of the active functional groups.

Meanwhile, the FTIR spectra showed the presence of anatase TiO_2 NPs in the coating films. The functional group spectra of Ti-O and Ti-O-Ti were at 669 cm^{-1} and 806 cm^{-1} for the acrylic film, and at 656 cm^{-1} and 808 cm^{-1} for the polyurethane composite film (Figure 3, a-b). A comparable analysis of the FTIR spectrum of anatase TiO_2 NPs revealed these relative functional groups, as reported by Praveen et al. (2014). The TiO_2 NPs characterization of anatase type was also proven using XRD as shown in Figure 4.

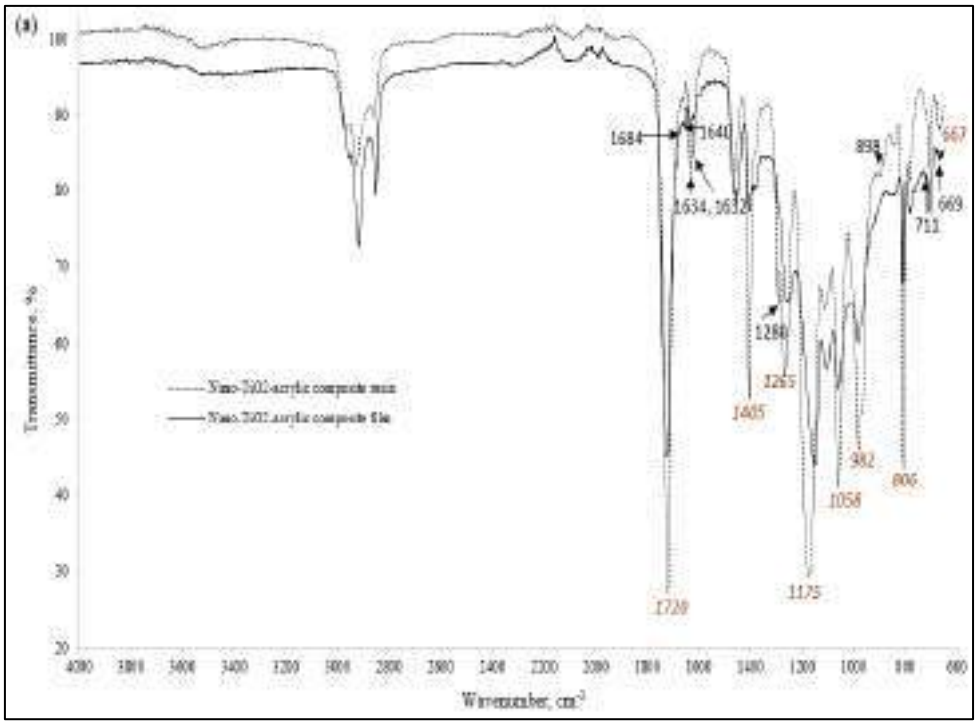

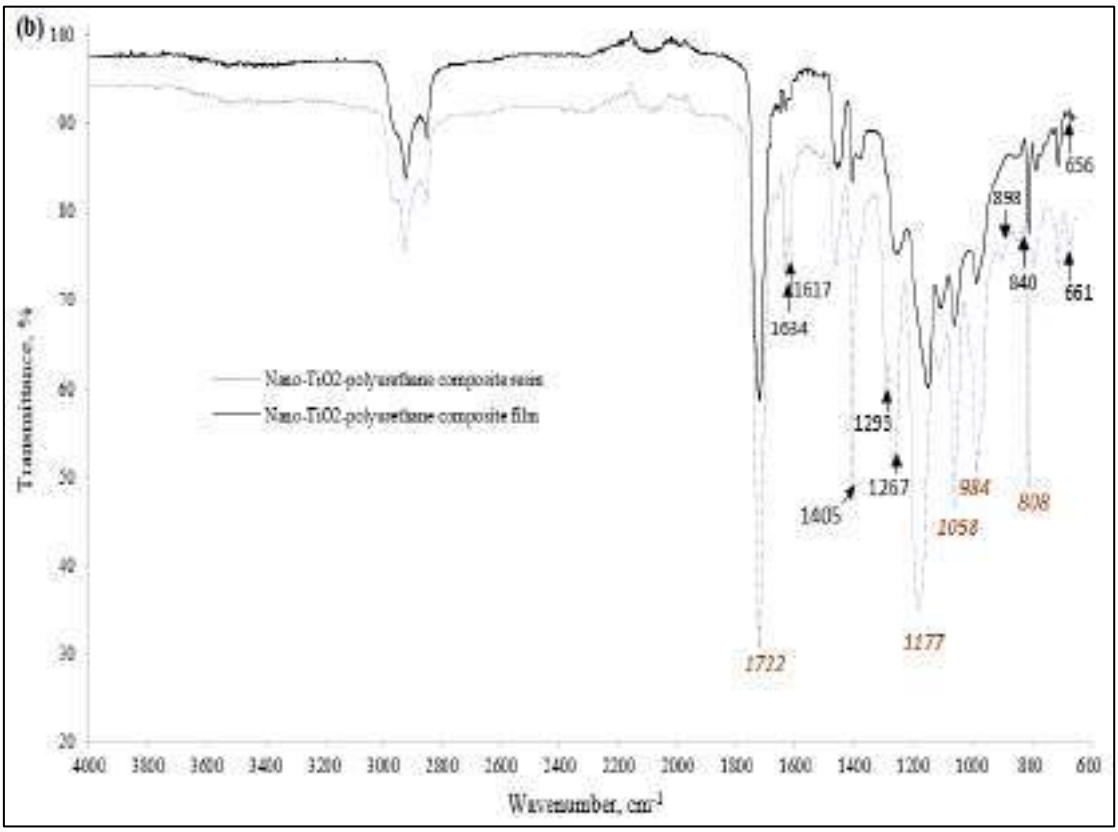

Figure 3 FTIR spectra of the resin composites after curing: **(a)** nano-TiO_2-acrylic composite film; **(b)** nano-TiO_2-IPDI-polyurethane composite film

Table 1 FTIR frequency range and functional groups in the sample after curing process

Wavenumber, cm^{-1}	Decreases of peak after curing	
	(a) Acrylic	(b) Polyurethane
C=O carbonyl	1720	1722
C=O ester	1684, 1640	-
-C=C-	1634, 1632	1634, 1617
-C-O	1280	1267, 1293
-C-H	898	898
TEOS	711	840
Ti-O, Ti-O-Ti	669, 806	656, 808

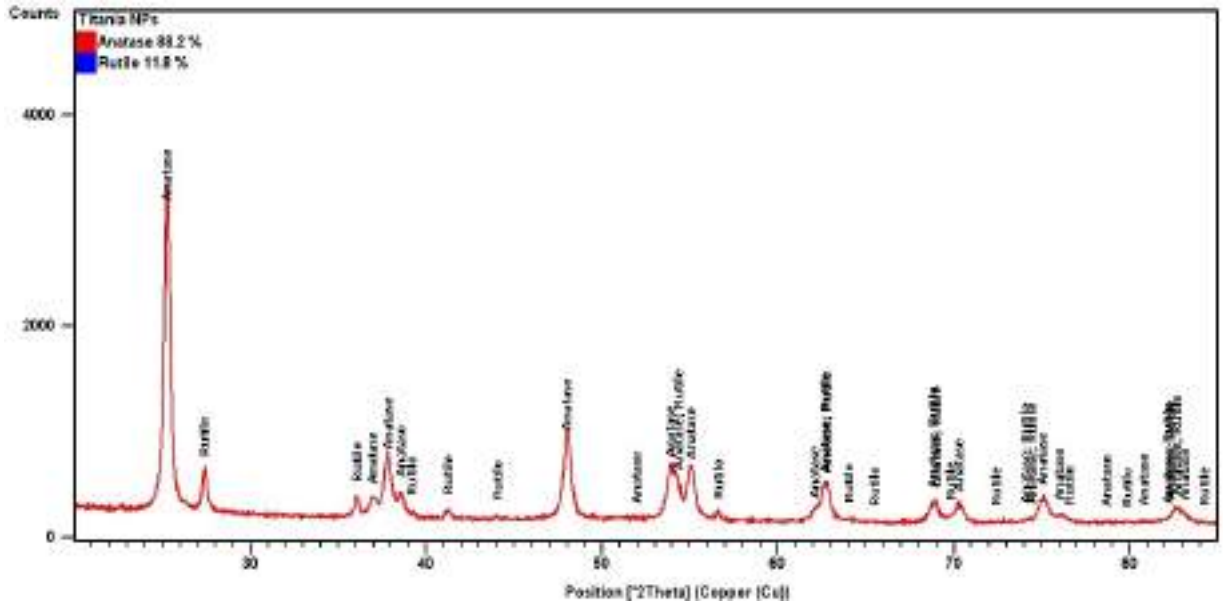

Figure 4 XRD spectrum of anatase TiO_2 NPs

Furthermore, the EDX analysis of composite films was depicted in Figure 5a and Figure 5b. The findings revealed the presence of nano-TiO_2 chemical elements in nano-TiO_2-acrylic composite film and nano-TiO_2-IPDI-polyurethane composite film were 0.52% and 6.89%, respectively. Furthermore, the addition of nano-TiO_2 in acrylic composite film and polyurethane composite film calculated by using UV-Vis spectrophotometer were 6.42 mg/L and 6.98 mg/L, respectively (Figure 5c), whereby the percentage value is corresponding to the EDX's element percentage, especially the nano-TiO_2-IPDI-polyurethane composite film.

Therefore, the effects of key reaction parameters, such as type of soft and hard segments of the polymer bonds influence the physical properties of coatings. The soft segment of polymer is responsible for facilitating the incorporation of the nanofiller mixture into the polymer chain (Figure 2d). Similarly, a higher molecular weight (Mw) of polyurethane allows for a greater uptake of nanofiller volume than the smaller size Mw of acrylic.

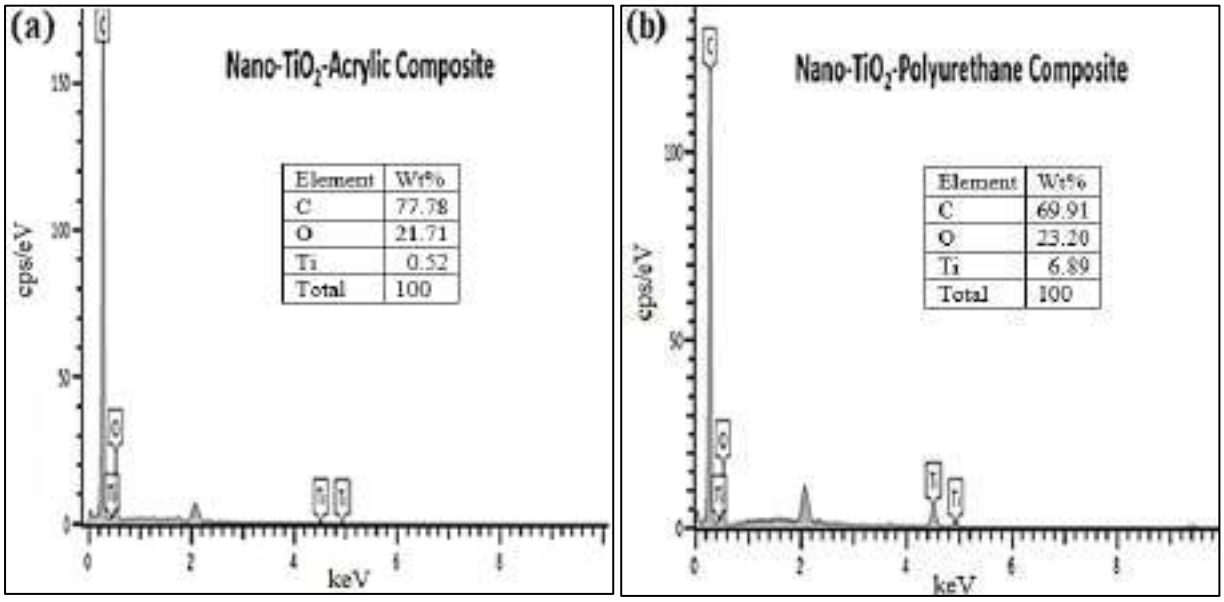

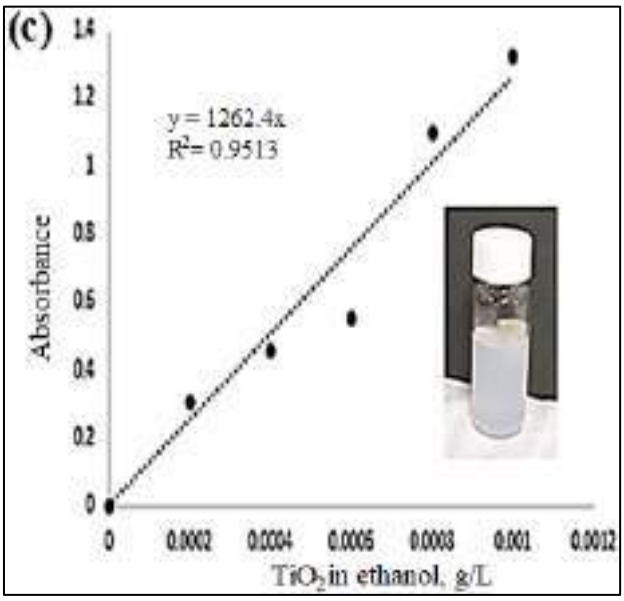

Figure 5 EDX elemental mapping of the nano-TiO_2: **(a)** nano-TiO_2 acrylic composite and **(b)** nano TiO_2-IPDI polyurethane composite, **(c)** Calibration curve of TiO_2 in ethanol solution by using UV-Vis spectrophotometer

Surface characterization and hydrophobicity

The FESEM images showed that the TiO_2-APO NPs were less than 150 nm in size and were spherical shape (Figure 6). Vuong (2020) also found a similar result with TiO_2 NPs in the acrylate urethane coating. Nanocoatings that containing the TiO_2-APO NPs produced a high-water contact angle. The present findings demonstrated the hydrophobic behavior by showing that the inclusion of TiO_2 NPs raised the contact angle for both acrylic- and polyurethane-type composite coatings, with a value greater than 90^o (Figure 6e). The addition of NPs such as graphite to the palm oil-based coating produced a similar effect, as reported by Alias in 2022(b).

The polyurethane- and acrylic-based films that showed hydrophilic properties had turned to hydrophobic by the presence of TiO_2 NPs as a composite film (Figure 6e). Furthermore, a small roughness surface of acrylic composite coating at 77.83 nm was proposed to be the reason for the higher hydrophobicity rate (Figure 6 d-e). The composite coating film of acrylic-type exhibited substantially higher rate of water contact angle although the polyurethane-IPDI composite coating resulted a higher value of water contact angle (Figure 6e ii, iv).

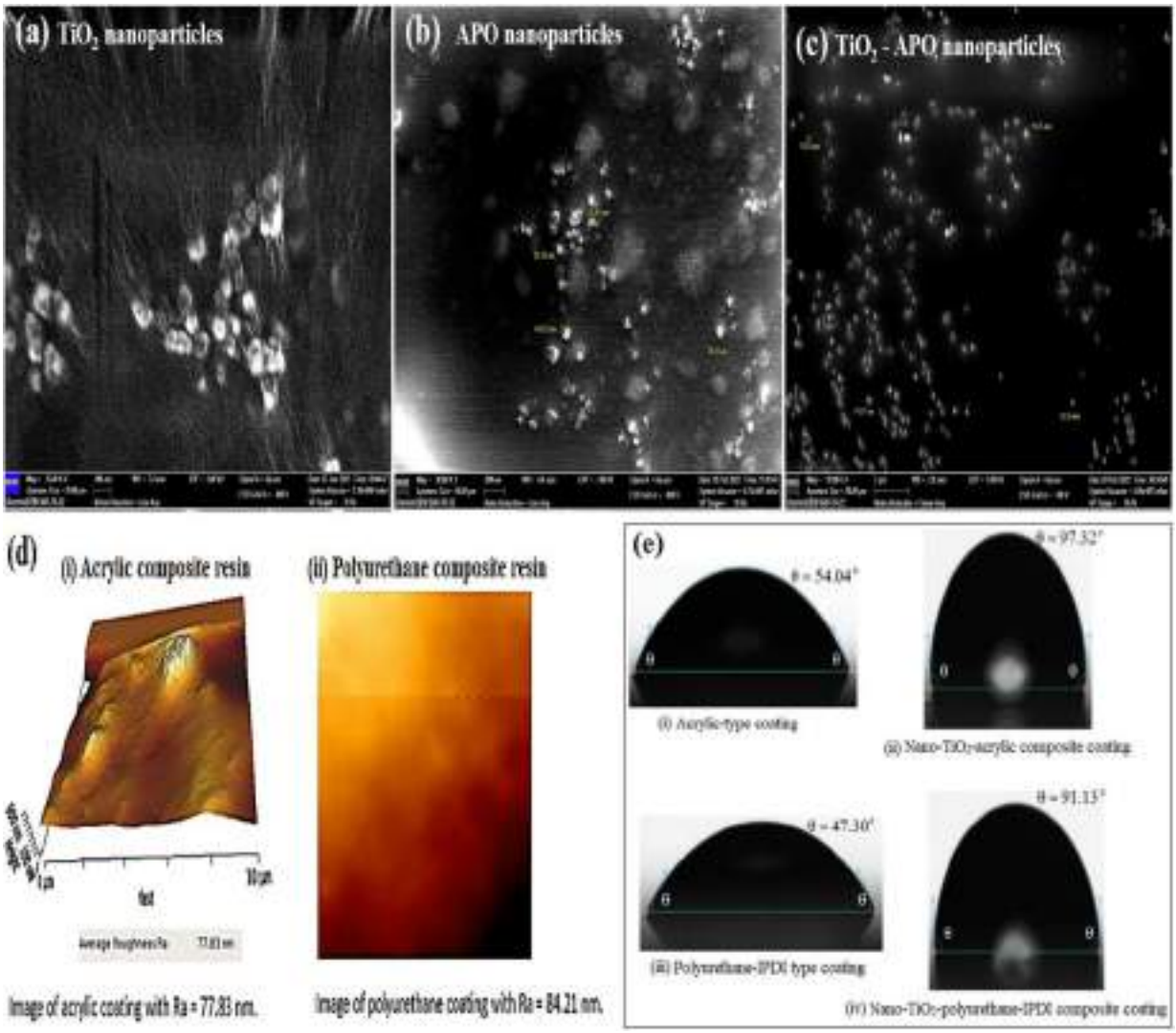

Figure 6 FESEM image of nanoparticles: **(a)** TiO_2 NPS, **(b)** APO NPs, **(c)** TiO_2-APO NPs, **(d)** AFM image of acrylic- and polyurethane composite coatings comprising TiO_2-APO NPs and **(e)** Water contact angle measurement of acrylic- and polyurethane-type coatings

Thermal and Mechanical Properties

Plots of the thermogravimetric (TG) reduction rate versus the temperature measured under a N_2 atmosphere are displayed in Figure 7, and the results are summarized in Table 2. The acrylic and polyurethane films underwent a three-step thermal degradation profile while the composites bond underwent a four-step thermal degradation profile (Figure 7).

In the present work, synthesis revealed the influence of TiO_2-APO NPs on the thermal performance of composite coatings. The thermal stability of the polymer composite coatings doped with TiO_2-APO NPs increases. TGA results showed that the presence of TiO_2 NPs practically decelerated the decomposition of composites backbone by means of a significant improvement in thermal property for surface coating applications. A comparable result was produced using TiO_2 NPs in the thermoplastic polypropylene nanocomposites coating, as studied by Bendaoued et al. (2022).

The polyurethane-IPDI type coating containing TiO_2-APO NPs demonstrated superior thermal properties as compared to the acrylic-based type coatings and common polyurethane film, with degradation profile started at peak temperatures of 197 ^oC (Li, 2006). The degradation of the acrylic and polyurethane films started at 130 ^oC and 157 ^oC, respectively while the acrylic-composite bond started at peak temperature of 133 ^oC. Figure 2d (ii) shows that the presence of a hard segment network and TiO_2-APO NPs made polyurethane-IPDI-based coating films more stable.

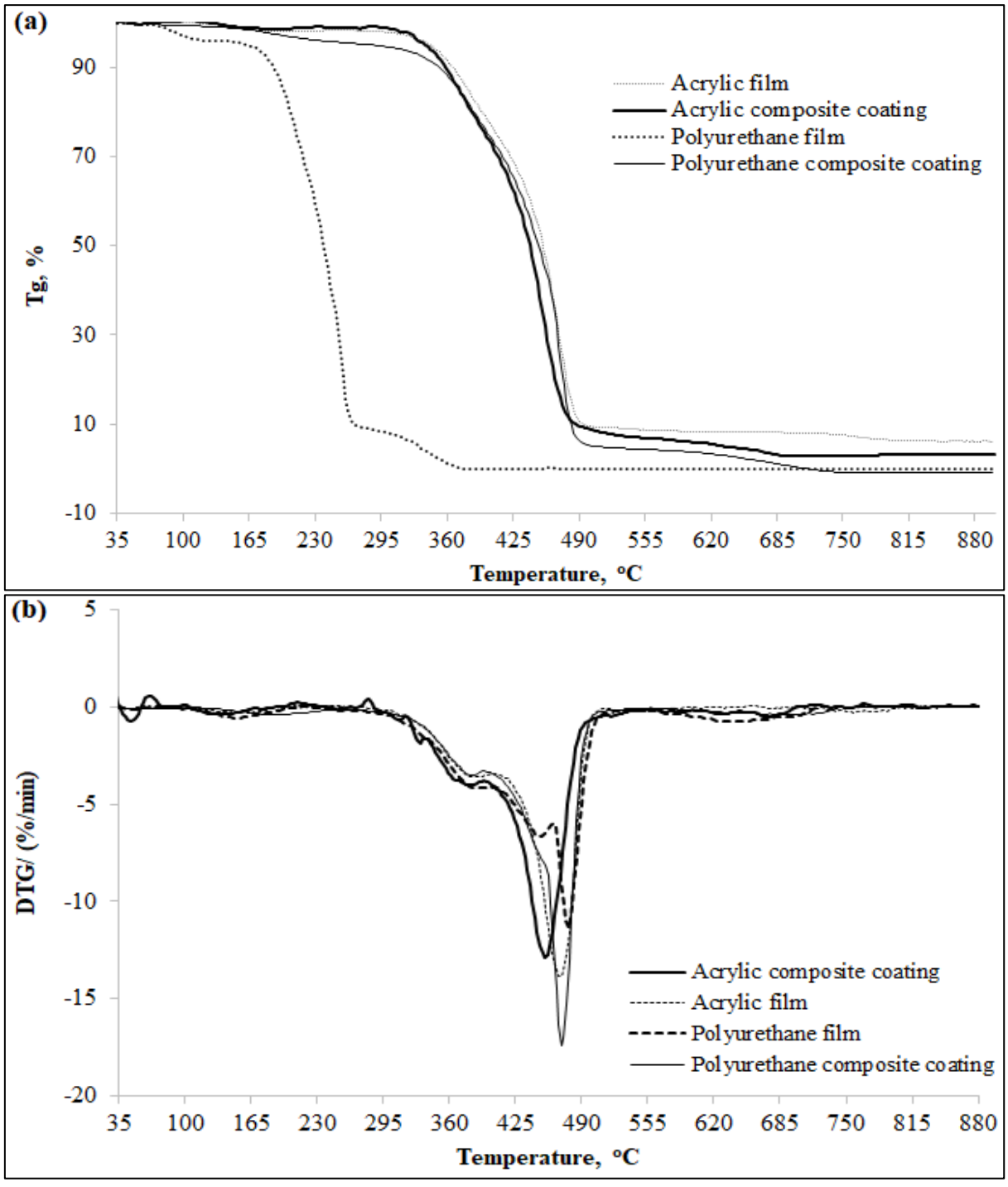

Figure 7 TGA curves of the polymer coatings: **(a)** TG curve and **(b)** Derivative thermogravimetry (DTG) curve

Table 2 Thermal degradation temperatures of coatings obtained with thermogravimetric analysis (TGA) (N_2)

Coatings	First-step thermal temperature (°C)	Second-step thermal temperature (°C)	Three-step thermal temperature (°C)	Four-step thermal temperature (°C)
Acrylic film	130	382	469	-
Acrylic composite coating	133	384	454	673
Polyurethane film	157	387	477	-
Polyurethane composite coating	197	385	470	672

Table 3 reveals the mechanical properties of coatings under various testing conditions. The incorporation of TiO_2-APO NPs into the coatings increased the gel content property. Increased gel content means increased crosslinking, thermal and several mechanical strengths, as evidenced by the polyurethane-IPDI type coating, which has improved thermal, anti-scratch, and adhesion properties (Shahnooshi, 2019)

Table 3 Mechanical property of coatings at different preparation conditions

Coatings	Acrylic-based resin		Polyurethane-based resins					
	EPOLA		POBUA-IPDI		POBUA-IPDI-PETIA		POBUA-TDI-HEA	
	Control	With NPs	Control	With NPs	Control	With NPs	Control	With NPs
Gel content (%)	66.75	96.31	90.66	97.88	85.58	97.69	72.92	100
Scratch test, N	2.0	3.0	1.0	4.0	3.0	2.5	5.0	4.0
Adhesion, Percent area remained, % (on white paper surface)	72	92	84	100	92	52	98	100
Hardness, %	92.67	8.77	90.66	27.98	93	42.72	89.67	59.88
Transmittance, %	85.70	86.3	89.4	86.3	88.80	86.4	85.83	86.5

The addition of TiO_2-APO NPs to the coatings resulted in increased anti-scratch properties (Table 3). For polyurethane, the anti-scratch property of IPDI-based aliphatic diisocyanate increased while the end-capped type, such as the IPDI-PETIA-aliphatic diisocyanate and the TDI-HEA-aromatic isocyanate decreased, respectively (Table 4). Figure 8 shows the diisocyanates and monomers commonly used for polyurethane synthesis. Type of diisocyanate and monomer influenced the polyurethane property. The anti-scratch property of acrylic and polyurethane-IPDI type composites increased due to its rigid crosslinking network as compared to the other coatings (Page, 2007; Ingrosso, 2015; Verma, 2018; Alias, 2022 a,b) (Table 2). According to the findings of a study conducted by Alias et al. (2022, a,b) cross-linked polyurethane (POBUA) surfaces have the ability to function as a barrier coating that protects mild steel surfaces from corrosive substances.

Table 4 Scratch test of coatings at different preparation conditions

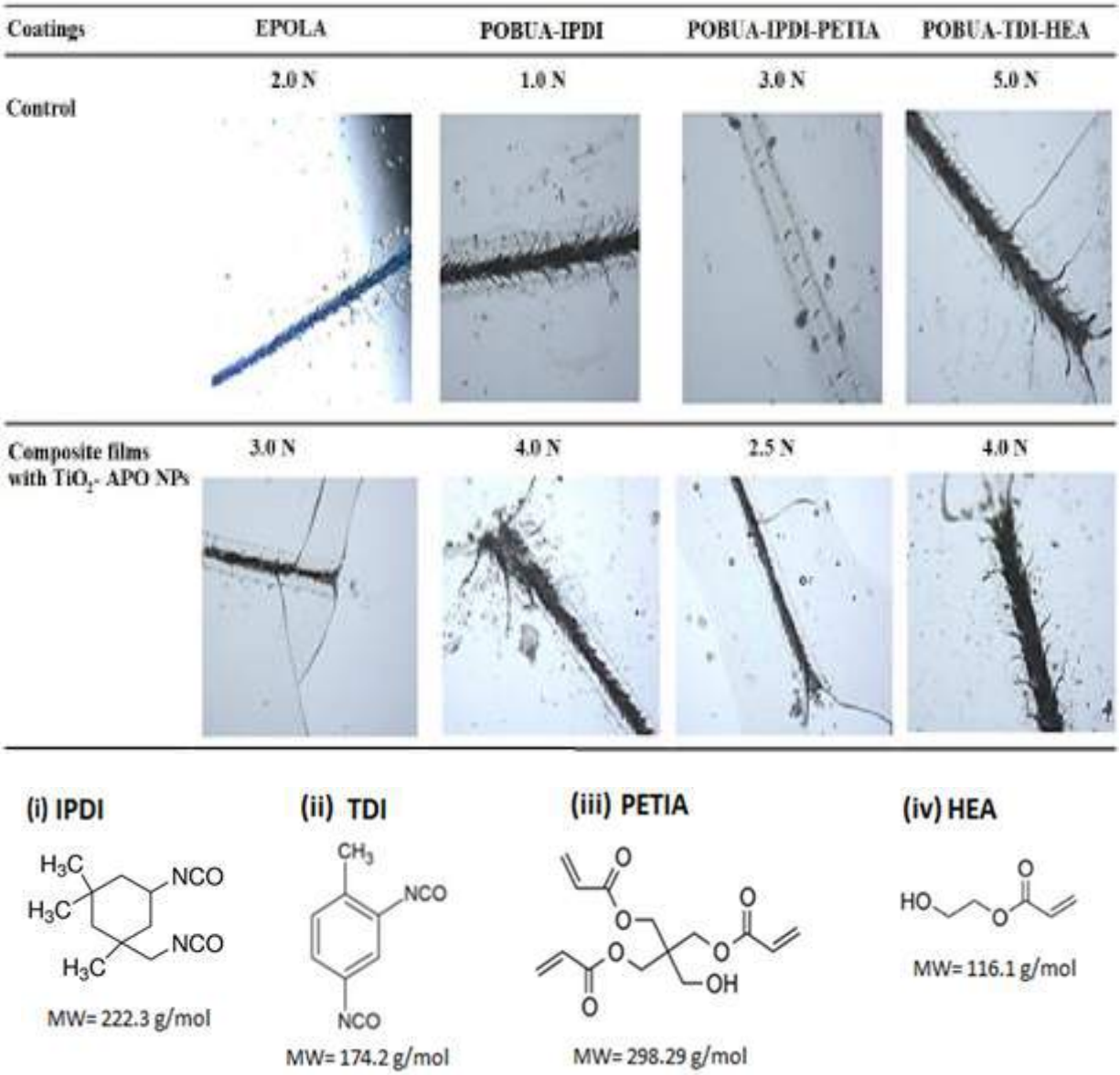

Figure 8 The diisocyanates: (i) IPDI (Isophorone diisocyanate), (ii) TDI (Toluene diisocyanate) and the monomers: (iii) PETIA (Pentaerythritol triacrylate), (iv) HEA (2-Hydroxyethyl acrylate) used in polyurethanes synthesis

The coating sample exhibited an increased adhesion property after the addition of TiO_2-APO NPs, which attributed to improved surface tension between the molecular forces of the object and the composite resin (Winnicki, 2021) (Table 3). However, hardness did not increase indefinitely with increasing crosslink density. The TiO_2-APO NPs had a larger influence on hardness because the coating hardness had decreased with addition of 1wt% of NP-TiO_2 content in the blend. The result presented that as the soft and hard segments of the polymer chain gets irregular by TiO_2-APO NPs, the hardness property of the coating decreases (Figure 2, d2). Previous studies have shown that TiO_2 NPs is distributed on the soft segment of the polyurethane which involves the interaction of -OH groups of TiO_2 NPs and the ester groups of polymers (Salahshoori, 2023). A high crosslinking density but a low hardness feature may arise from the typical termination processes of free radical polymerization on the dead polymers/ monomers,

given the needless side reactions that lead to non-active polymers/ monomers (Yamago & Nakamura, 2013). Similarly, the transmittance results showed almost no significant progress in the transmittance properties of the coatings (Table 3).

Polymeric coatings with antimicrobial activity

The antimicrobial assessment showed that no antimicrobial zone had formed (Figure 9). The slight presence of 1wt% of NP-TiO_2 seemed had no influence on the antimicrobial activity detected on top and bottom surfaces of the film. However, the center zone potentially revealed a clear zone that was unoccupied by E-coli in comparison to the surrounding area that was occupied by E. coli (Figure 9). The composite coatings and polyurethane film, displayed antimicrobial effect on the central zone as compared to the control acrylic film. The composite coatings and polyurethane film in this study showed a qualitative inhibitory effect.

On the other hand, the hydrophobic nature of the coating due to the chemical cross-linking effect could improve its antimicrobial properties on both surfaces, which can potentially be explained by the lack of adhesion and microbial growth (Arango-Santander, 2018). The coating's internal cross-linking features most likely cause no pores to exist between the polymer network due to the durable three-dimensional network that potentially prevents microbes or dirt from growing on the surface.

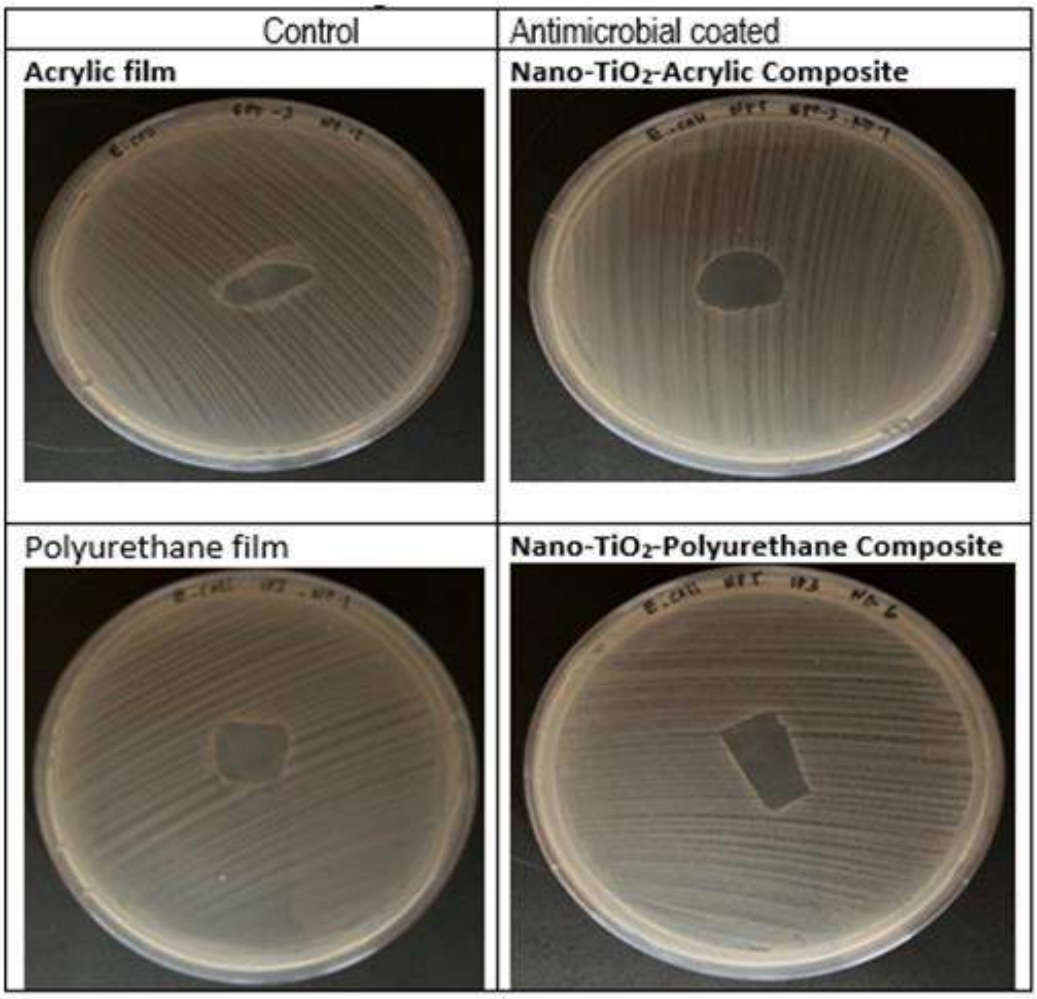

Figure 9 Comparative assessment of antimicrobial activity of palm oil-based coatings against E. coli (Gram-negative bacteria)

CONCLUSION

A variety of unique materials can be functionalized by using the sol-gel technique, which is notably useful for creating inorganic-organic coating materials. The presence of TiO_2-APO improves the properties of the gel content and anti-microbes. Acrylic and polyurethane composite films containing nano-TiO_2 have a high potential for antimicrobial coating applications, such as improving the safety of coated surfaces against microbes by increasing the volume of TiO_2 NPs above 1%. The study also demonstrated that polyurethane-IPDI composite has better thermal, anti-scratch, and several mechanical properties for surface coating applications than acrylic-based and common polyurethane coatings.

ACKNOWLEDGEMENTS

Acknowledgments were attributed to those who directly and continuously contribute to and promote this research, including all of the Synthesis and Radiation Curing Group (KSPS) staff at the Malaysian Nuclear Agency's Radiation Processing Technology Division (BTS). The authors would like to thank the Malaysian Nuclear Agency for the research support (NM-R&D-20-52).

REFERENCES

Abbas, M.; Iftikhar, H.; Malik, M.H.; Nazir, A. (2018). Surface Coatings of TiO_2 Nanoparticles onto the Designed Fabrics for Enhanced Self-Cleaning Properties. *Coatings*, *8*: 35.

Alias, M.S, Othman N., Kamarudin S., Harun M.H., Mohamed M., Mohamad S.F., Saidin N., Tajau R., and Abdul Halim K.A. (2022a). Green corrosion coating using palm oil based urethane acrylate (POBUA) on mild steels in 3.5 NaCl solution, *Materials Today: Proceedings*. 66.

Alias, M.S, Othman N., Kamarudin S., Harun M.H., Mohamed M., Mohamad S.F., Samsu, Z. (2022b). Influence of graphite particles in UV-curable corrosion protection coating from palm oil based urethane acrylate (POBUA), Industrial Crops and Products, 187(B): 115436.

Arango-Santander, S., Pelaez-Vargas, A., Freitas, S.C. and García, C. (2018). A novel approach to create an antibacterial surface using titanium dioxide and a combination of dippen nanolithography and soft lithography. Scientific Reports, 8:15818.

Baig, U., Uddin, M.K., Sajid, M. (2020). Surface Modification of TiO2 nanoparticles using Conducting Polymer Coating: Spectroscopic, Structural, Morphological Characterization and Interaction with Dye Molecules, Materials Today Communications, ISSN 2352-4928, 25: 101534.

Bendaoued, A., Messaoud, M., Harzallah, O., Bistac,S. and Salhi, R. (2022). Nano-TiO2 effect on thermal, rheological and structural properties of thermoplastic polypropylene nanocomposites, *Journal of Materials Research and Technology*, 17: 2313-2325.

Chouirfa, H., Bouloussa, H., Migonney, V., Falentin-Daudré, C. (2019). Review of titanium surface modification techniques and coatings for antibacterial applications. Acta Biomaterialia, Elsevier, 83: 37- 54

Chuang, Y., Wang, L., Feng, K., Subramanian, A., Chang, C., Simon, M., Nam, C. and Rafailovich, M. (2021), The Role of Titania Surface Coating by Atomic Layer Deposition in Improving Osteogenic Differentiation and Hard Tissue Formation of Dental Pulp Stem Cells. Adv. Eng. Mater., 23: 2100097.

Cotolan, N., Rak, M., Bele, M., Cör, A., Muresan, L.M. and Milošev, I. (2016). Sol-gel synthesis, characterization and properties of TiO2 and Ag-TiO2 coatings on titanium substrate, Surface and Coatings Technology, ISSN 0257-8972, 307 (A):790-799.

Falco, G.D., Ciardiello, R., Commodo, M., Gaudio, P.D., Minutolo, P., Porta, A., D'Anna, A. (2018). TIO2 nanoparticle coatings with advanced antibacterial and hydrophilic properties prepared by flame aerosol synthesis and thermophoretic deposition, Surface and Coatings Technology, ISSN 0257-8972, 349: 830-837.

Horkavcová, D.; Doubet, Q.; Lecomte-Nana, G.L.; Jablonská, E.; Helebrant, A. (2021). Development of Adhesive, Bioactive and Antibacterial Titania Sol-Gel Coating on Titanium Substrate by Dip-Coating Technique. Coatings, 11: 243. https://doi. org/10.3390/coatings11020243

Ingrosso, C., Ca Corcione, C.E., Striani, R., Comparelli, R., Striccoli, M., Agostiano, A., Lucia Curri, M. and Frigione, M. (2015). UV-Curable Nanocomposite Based on Methacrylic-Siloxane Resin and Surface-Modified TiO_2 Nanocrystals. *ACS Applied Materials & Interfaces*, *7*(28):15494-15505.

Kartini, I., Khairani, I. Y. , Chotimah, C., & Wahyuni, K. T. S. (2018). Nanostructured Titanium Dioxide for Functional Coatings. In (Ed.), Titanium Dioxide - Material for a Sustainable Environment. IntechOpen.

Kumaravel, V., Nair, K.M., Mathew, S., Bartlett, J., Kennedy, J.E., Manning, H.G., Whelan, B.J., Leyland, N.S., Pillai, S.C. (2021). Antimicrobial TiO2 nanocomposite coatings for surfaces, dental and orthopaedic implants, Chemical Engineering Journal, ISSN 1385-8947, 416: 129071.

Li, F., Zhou, S., Gu, G., and Wu, L. (2006). UV-curable coatings with nano-TiO_2. Polymer Engineering and Science - POLYM ENG SCI. 46. 1402-1410.

Mahltig, B., Grethe, T., Haase, H. (2018). Antimicrobial Coatings Obtained by Sol-Gel Method. In: Klein, L., Aparicio, M., Jitianu, A. (eds) Handbook of Sol-Gel Science and Technology. Springer, Cham.

Mamat Rokhmat, S., Wibowo, E. and Mikrajuddin Abdullah, K. (2017). Coating TiO2 nanoparticles on the surface of transparent plastic granules using combined electrostatic and heating methods for the photocatalytic degradation of organic pollutants in water, Environmental Nanotechnology, Monitoring & Management, ISSN 2215-1532, 8:1-10.

Page, K., Palgrave, R.G., Parkin, I.P., Wilson, M., Savin, S.L.P. and Chadwick, A.V. (2007). Titania and silver–titania composite films on glass—potent antimicrobial coatings. *J. Mater. Chem.***,** 17: 95-104.

Praveen, P., G. Viruthagiri G., Mugundan, S., and Shanmugam, N. (2014). Structural, optical and morphological analyses of pristine titanium di-oxide nanoparticles – Synthesized via sol–gel route. *Spectrochimica Acta Part A: Molecular and Biomolecular Spectroscopy*, 117: 622–629.

Salahshoori, I., Asghari, M., Jorabchi, M.N., Wohlrab, S., Rabiei, M., Raji, M., Afsari, M. (2023). Methylene diisocyanate - aided tailoring of nanotitania for dispersion engineering through polyurethane mixed matrix membranes: Experimental investigations, *Arabian Journal of Chemistry*, 16(6): 104792.

Salih, A.M., Wan Yunus, W.M.Z., Mohd Dahlan, K.Z. and Ahmad, M. (2012). UV-Curable Palm Oil Based-Urethane Acrylate/Clay Nanocomposites, *Pertanika J. Sci. & Technol.*, 20(2), 435-444.

Salleh, M.Z., Tajau, R. and Mudri, N.H. (2016). The evolution of palm oil acrylates within 20 years in Nuclear Malaysia, Nuclear Malaysia R&D Seminar 2016, IAEA, Vienna, 1-6.

Shahnooshi, M., Eshaghi, A. and Aghaei, A.A. (2019). Transparent anti-fogging and anti-scratch SiO_2/SiO_2–TiO_2 thin film on polycarbonate substrate, *Mater. Res. Express* 6 086447.

Stavila, E., Yuliati, F., Adharis, A., Laksmono, J.A. and Iqbal, M. (2023). Recent advances in synthesis of polymers based on palm oil and its fatty acids, RSC Adv.**,** 13**:** 14747-14775.

Tajau, R., Hilmi, M.H., Salleh, M.Z., Mohd Dahlan, K.Z., M.D. Che Ismail, R., Muhammad Faisal, S., Sheikh Abdul Rahman, S.M.Z. (2013). Production of uv-curable palm oil resins/oligomers using laboratory scale and pilot scale systems, Sains Malaysiana, 42: 459-467.

Tajau, R., Ibrahim, M.I., Mohd Yunus, N., Mahmood, M.H., Salleh, M.Z. and Nik Salleh, N.G. (2014). Development of palm oil-based UV-curable epoxy acrylate and urethane acrylate resins for wood coating application, AIP Conference Proceedings 1584, 164. Doi: 10.1063/1.4866125.

Tajau, R.; Rohani, R.; Alias, M.S.; Mudri, N.H.; Abdul Halim, K.A.; Harun, M.H.; Mat Isa, N.; Che Ismail, R.; Muhammad Faisal, S.; Talib, M.; Rawi Mohamed Zin, M.; Izni Yusoff, I.; Khairul Zaman, N.; Asyila Ilias, I. (2021). Emergence of Polymeric Material Utilising Sustainable Radiation Curable Palm Oil-Based Products for Advanced Technology Applications. *Polymers*, *13*, 1865

Tran, M.L., Fu, C.C., Wei, T.H., Hsieh, C.T., Juang, R.S. (2020). Surface coating of titania and graphene oxide onto plasma-activated polymer membranes as efficient photocatalysts for organics removal from water, Journal of Water Process Engineering, ISSN 2214-7144, 37:101488.

Tudu, B.K., Sinhamahapatra, A. and Kumar, A. (2020). Surface Modification of Cotton Fabric Using TiO_2 Nanoparticles for Self-Cleaning, Oil–Water Separation, Anti-stain, Anti-Water Absorption, and Anti-bacterial Properties, *ACS Omega*, *5*(14): 7850-7860.

Verma, J., Nigam, S., Sinha, S. and Bhattacharya, A. (2018). Development of polyurethane based anti-scratch and anti-algal coating formulation with silica-titania core-shell nanoparticles,Vacuum 153: 24-34,ISSN 0042-207X.

Vuong, N.T. (2020), The role of rutile TiO_2 nanoparticles on weathering resistance of photocurable acrylate urethane coating. Vietnam Journal of Chemistry, 58: 314-320.

Winnicki, M., Łatka, L. Jasiorski, M., Baszczuk, A. (2021). Mechanical properties of TiO2 coatings deposited by low pressure cold spraying, Surface and Coatings Technology, ISSN 0257-8972, 405, 126516.

Yamago, S., and Nakamura, Y. (2013). Recent progress in the use of photoirradiation in living radical polymerization, Polymer, 54(3): 981-994.

Zhao, L., Wang, H., Huo, K., Cui, L., Zhang, W., Ni, H., Zhang, Y., Wu, Z., and Chu, P. (2011). Antibacterial nano-structured titania coating incorporated with silver nanoparticles. Biomaterials. 32, 5706-16.

Jurnal Sains Nuklear Malaysia, 2024, 36(No. 1): 99 – 110
ISSN: 2232-0946

MECHANICAL PROPERTIES OF BIO-BASED SELF-HEALING COATING WITH EMBEDDED MICROCAPSULES

N. H. Mudri, [1*] L. C. Abdullah,[2,3] M. M. Aung,[3,4] D. R. A Biak,[2,5] K. A. A. Halim[1] & F. F. Hilmi[1]

[1]*Radiation Processing Technology Division, Malaysian Nuclear Agency, Kajang 43000, Selangor, Malaysia;*
[2]*Department of Chemical and Environmental Engineering, Faculty of Engineering, Universiti Putra Malaysia, Serdang 43400, Selangor, Malaysia;*
[3]*Institute of Tropical Forestry and Forest Products (INTROP), Universiti Putra Malaysia, Serdang 43400, Selangor, Malaysia;*
[4]*Centre of Foundation Studies for Agricultural Science, Universiti Putra Malaysia, Serdang 43400, Selangor, Malaysia;*
[5]*Institute of Advanced Technology, Universiti Putra Malaysia, Serdang 43400, Selangor, Malaysia;*
*Corresponding author: nurul_huda@nm.gov.my

Abstract

Self-healing coating is one of the smart coatings that can restore physical appearance and performance after exposure to damage such as scratches and weathering. Self-healing coatings have several benefits, including extending material life and lowering operating costs by reducing the need for planned maintenance, especially in situations involving remote locations. Microcapsule is one of the techniques that are widely used in the preparation of self-healing coating. This approach used an active healing agent to be stored in the microcapsule. In the previous work, pure jatropha oil (JO) and its derivatives known as jatropha oil-based polyurethane acrylate (JPUA) were encapsulated into a polyurea formaldehyde (PUF) microcapsule. In this study, JO and JPUA-IPDI-based microcapsules were loaded into the JPUA-TDI-based coating. 5 wt% and 10 wt% loading of microcapsules were dispersed using a mechanical stirrer in the coating formulation until a homogenous mixture was obtained. The self-healing coating formulation was coated on a steel plate (100 mm x 100 mm x 1.5 mm) using a bar applicator with a thickness of 50 µm,100 µm, 150 µm and 200 µm. Then, the wet film was irradiated under UV light until fully cured. Mechanical tests such as Pendulum Hardness Test (ASTM D4366), Cross-cut Adhesion Test (ASTM D3359-09), Transmittance Test (ASTM E1348), and Haze Test (ASTM D1003) were performed on the cured self-healing coating. The mechanical properties of the self-healing coating were compared with the coating without microcapsule loading as a control. It was found that the hardness value was reduced as the microcapsules were incorporated into the coating formulation in 5% JPUA and 10% JPUA. This trend continuously declined as the coating was thickened from 50 µm to 100 µm, 150 µm and 200 µm in the self-healing coating containing microcapsules. For the adhesion test, Control samples at all of the testing thicknesses showed a 4B adhesion score where less than 5% of the area was removed. A similar grade was displayed by 5% JPUA at 50 µm. The remaining samples indicated deteriorated adhesion properties as the film thickness increased and microcapsule loading increased. The 10% JPUA at a thickness of 200 µm showed the worst adhesion property with 15% to 35% of the removed area. As a conclusion, self-healing coating with 5 wt% loading of JO and JPUA-IPDI-based microcapsule with thickness of 50 µm has maintained the hardness, adhesion, haze, and transmittance properties when compared with the control sample.

Keywords: self-healing; microcapsule; mechanical properties; thickness; hardness

INTRODUCTION

The coating industry has witnessed a transformative shift with the advent of smart materials, particularly in the area of self-healing coatings. Self-healing coatings, also known as self-repairing coatings, have gained significant attention in recent years due to their ability to autonomously repair damage (Paquet et al., 2020). These coatings have the potential to revolutionize various industries, including marine, aerospace, and automotive, by increasing the durability and longevity of coated materials. By incorporating self-healing technology into coatings, materials can regain their structural integrity and functionality after being exposed to external forces or damage. This innovation solves the challenges faced by traditional coatings, such as limited product lifespan and susceptibility to corrosion (Liu et al., 2021). Furthermore, self-healing coatings have the potential to reduce maintenance and repair costs, as they can autonomously repair minor damages before they escalate into major issues that require costly repairs or replacements (Cheng et al., 2022). To develop effective self-healing coatings, researchers have employed various approaches such as microcapsule, vascular, and intrinsic systems. The microcapsule-based self-healing coating is one of the popular options and is nearly being commercialized (Ouarga et al., 2022). Via this approach, selective healing agent was encapsulated in a microcapsule followed by simply mixing procedure with the coating matrix. These microcapsules are designed to rupture upon damage such as scratch and crack on the coating surface. Subsequently, healing agents are released from the microcapsule to fill and repair the damages surface (Kothari & Iroh, 2023). The healing agents are hardened via polymerization process that induced either by catalyst or environmental factors such as UV light (Chen et al., 2019; Wang et al., 2019), oxygen (Song et al., 2022) and moisture(Alizadegan et al., 2018).

Currently, vegetable oils have been broadly used not only in food application but also in the industrial sectors such as paints, plasticizers, lubricants, and hardeners preparation and modification (Ataei et al., 2019; Karami et al., 2019). In order to reduce the carbon footprint, vegetable oils were also explored to be the healing agent (core content) for the microcapsule-based system. Tung (Li et al., 2018) and linseed (Çömlekçi & Ulutan, 2018; Wang & Zhou, 2018) oils are among popular oils that encapsulated directly without chemical modification. This is due to the high content of Iodine Value (IV) of these oils that allows them being polymerize when react with oxygen in the atmosphere (Li et al., 2018; Song et al., 2022). However, vegetable oils with low IV require chemical modification to tailor with the mechanism reaction during the repairing action. For example, palm (Saman et al., 2018) and coconut oil (Khorasani et al., 2017) have been reported to be converted to alkyd functionality before being encapsulated. Apart of that, Shisode and his team has reported the utilisation of pure soy oil with addition of cobalt drying agent (Shisode et al., 2018). To date, no study has been reported on utilisation of jatropha oil (JO) either in its pure or modified form for microcapsule-based self-healing coating purpose. JO is extracted from seed of *jatropha curcas* fruit. Apart of being locally available in Malaysia and South East Asia, JO (94 to 120 mg/g) has higher IV compared to palm oil (44 to 58 mg/g) that make it more reactive to chemical reaction particularly during the repairing mode (Amri et al., 2021).

Mechanical properties are crucial in determining the performance and durability of self- healing coating. However, the report on mechanical properties of microcapsule-based system is still limited to certain properties such as adhesion, hardness and bending and compression test (Jiang et al., 2021; Pongmuksuwan et al., 2023). For instance, a study on a microcapsule's wall made from melamine-formaldehyde was conducted whilst the core content was made from a mixture of carbonyl iron powder and multiwalled carbon nanotubes. The study revealed that as the addition of microcapsules increased, the gloss and adhesion of the coatings decreased. The addition of microcapsules to the coatings exhibited a tendency to increase the hardness, impact resistance and tensile properties, but followed by a decreasing trend (Wu et al., 2023). Despite the studies conducted in previous years,

the scope of transmittance and haze properties on self-healing coating are still unexplored in existing studies. Therefore, it is important to study these properties especially when referring to self-healing coating that applied on glass and clear surface.

This work focuses on investigating the mechanical properties of a self-healing coating formulated with pure jatropha oil and the modified form; jatropha oil-based polyurethane acrylate as a healing agent into PUF microcapsule. The research examines key parameters such as microcapsule loading and coating thickness in relation to mechanical properties, including pendulum hardness, adhesion, transmittance, and haze. These mechanical properties are considered as a good guideline on product application and its durability.

MATERIALS AND METHOD

Materials

Pure jatropha oil was purchased from from Biofuel Bionas Malaysia Sdn. Bhd., Malaysia. Trimethylolpropane triacrylate (TMPTA) was procured from Sigma-Aldrich, Germany whilst benzophenone was supplied from Acros Organic (Belgium). Two series of jatropha polyurethane acrylate; JPUA-TDI and JPUA-IPDI were synthesized from crude jatropha oil and were based on different diisocyanate. The details of the procedure were explained in previous studies (Mudri et al., 2020, 2021). The microcapsules were prepared based on procedure reported by (Baharom et al., 2023). The properties of each microcapsule are tabulated in Table 1.

Table 1 Properties of JO 400 and IPDI 400

Microcapsule	Physical appearance	Schematic diagram
JO 400		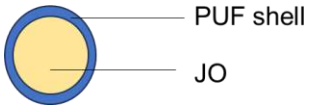
IPDI 400		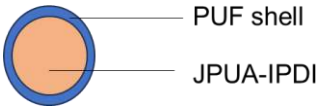

Preparation of Self-Healing Coating

Table 2 shows the components of the coating formulation for self-healing coating. Using the mechanical stirrer, JPUA-TDI, TMPTA and benzophenone were mixed until homogeneous. Subsequently, 5% and 10% of the microcapsules were dispersed in the coating formulation until a homogeneous mixture was obtained. Using a bar applicator, the film thickness was varied at 50 µm, 100 µm, 150 µm and 200 µm respectively on a glass plate (100 mm x 100 mm x 1.5 mm) and irradiated with UV light (UV-IST, Germany) for the curing process. Formulation without microcapsule was used as a control to determine the mechanical test for the self-healing coating. All

films were then directly tested for their mechanical properties to determine the best combination of microcapsule loading and film thickness for the self-healing test.

Table 2 Components of self-healing coating formulation

Code	Self-healing coating			Microcapsule Loading	
	JPUA-TDI (%)	**TMPTA (%)**	**Benzophenone (%)**	**JO 400 (%)**	**IPDI 400 (%)**
Control	65	35	4	–	–
5% JO	65	35	4	5	–
10% JO	65	35	4	10	–
5% IPDI	65	35	4	–	5
10% IPDI	65	35	4	–	10

Mechanical Test

Pendulum Hardness Test

In accordance with ASTM D4366, the hardness of the UV-cured film was measured using a pendulum hardness tester (TQC, Netherlands) in Koenig damping mode. The readings (in seconds) were taken in triplicate for each sample during the damping time of the pendulum until the pendulum came to a complete stop. The average of the measured values was calculated.

Cross-Cut Adhesion Test

A cross-cut adhesion test (Biuged, China) was performed based on ASTM D3359-09. The purchased kit included a cutter blade, adhesive tape, brush and a magnifying glass. Based on the coating thickness for making the grid pattern, a 1 mm wide cutter blade was selected. The transparent 3M Scotch tape on the grid was peeled off at an angle of 180°. The brush was used to carefully remove the dirt and the magnifying glass was used to examine the surface.

Transmittance and Haze Tests

Haze Illuminant Tester (BYK-Gardner, Geretsried, Germany) was used to test the transmittance (ASTM E1348) and haze (ASTM D1003) for self-healing coating cured films. The tester measured both properties simultaneously as percentages. All measurements were performed in triplicate and the average value was calculated.

Morphology Observation

An optical microscope (Zeiss Primotech, Germany) was used to determine the morphology of the microcapsule shape in a coating film after UV curing.

RESULT AND DISCUSSION

Pendulum Hardness

Pendulum damping tests were performed to assess the flexibility and hardness of the coatings containing microcapsules, as presented in Figure 1. For Control, the hardness value has increased proportionally with the increasing thickness of the coating. The high number of oscillations reflects the good hardness but low flexibility in the Control coating. In radiation curing, acrylate functionality acts as active sites for crosslinking. The amount of acrylate functionality increased proportionally with the thickness of the film. Therefore, the hardness property increased as the possibility of crosslinking increased (Fu et al., 2021).

However, the hardness value was reduced as the microcapsules were incorporated into the coating formulation in 5% JO, 10% JO, 5% IPDI and 10% IPDI. This trend was continuously declined as the coating was thickened from 50 µm to 100 µm, 150 µm and 200 µm in each coating containing microcapsules. This is due to the possibility of the microcapsules interfering with the curing process. In this study, microcapsule was added via physical mixing where it did not have any chemical bonding with the polyurethane network in the coating. The compatibility of the PUF-based microcapsule in the coating can be improved either by using epoxy-based coating (Pongmuksuwan et al., 2023). In addition, Paquet et al., (2020)has demonstrated that introducing hydrogen bonding between the microcapsule shell and coating matrix has improved the hardness of the self-healing coating material. The film of 5% JO and 5% IPDI with 50 µm has comparable hardness performance with the Control (around 80 seconds) when tested at 50 µm thickness correspondingly.

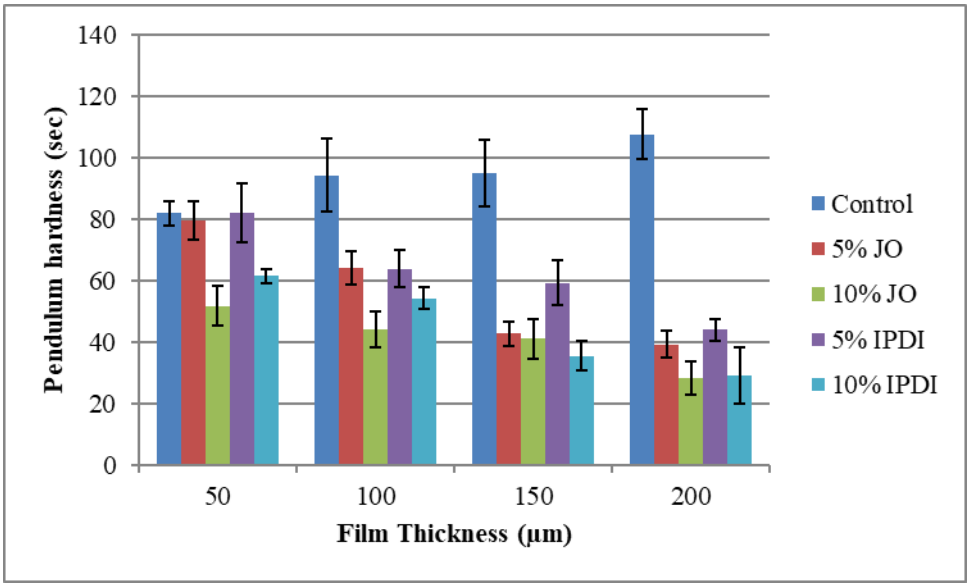

Figure 1: Pendulum hardness test for coating loaded with JO and JPUA-IPDI -based microcapsules

Adhesion Test

Cross-Cut Adhesion Test was conducted to investigate the effects of microcapsule embedment on the coating adhesion. The adhesion score of Control, 5% JO, 10% JO, 5% IPDI and 10% IPDI at thicknesses of 50 µm, 100 µm, 150 µm and 200 µm are tabulated in Table 3.

Table 3: Adhesion score of coating embedded with JO and JPUA-IPDI mixture-based microcapsules

Sample	Film Thickness (µm)	Adhesion Score
Control	50	4B
	100	4B
	150	4B
	200	4B
5% JO	50	4B
	100	3B
	150	3B
	200	3B
10% JO	50	3B
	100	3B
	150	2B
	200	2B
5% IPDI	50	4B
	100	3B
	150	3B
	200	3B
10% IPDI	50	3B
	100	3B
	150	2B
	200	2B

From Table 3, Control samples at all of the testing thicknesses showed a 4B adhesion score where less than 5% of the area was removed. A similar grade was displayed by 5% JO and 5% IPDI at 50 µm. The rest of the samples have deteriorated adhesion properties as the increased film thickness, and microcapsule loading increased. 10% JO and 10% IPDI at a thickness of 200 µm, respectively, showed the worst adhesion property with 15-35% of the removed area. The decline in mechanical properties in a coating with a high concentration of microcapsules might be due to non-uniform dispersion in the formulation. Therefore, the microcapsules also have restricted the mechanical bonding between the substrate and the coating matrix and caused poor performance in adhesion strength as the microcapsule loading was increased. Apart of that, the coating mixture becomes more viscous due to the additional loading of microcapsules. The high viscosity makes the coating formulation more difficult for to effectively penetrate and adhere to the substrate and led to the decrease in adhesion property (Pongmuksuwan et al., 2023). In this study, the formulation of 5% JO and 5% IPDI at a thickness of 50 µm were selected to be tested for self-healing test as the adhesion strength is comparable with the control where no microcapsule was added.

Transmittance Test

The effect of microcapsules loading at different film thicknesses is presented in Figure 2. All samples except 10% JO have a transmittance value of more than 85%, reflected a good transparency property (Adachi et al., 2018). This data indicated that the addition of microcapsules in 5% JO, 5% IPDI and 10% IPDI do not intervene in the transmittance property in the self-healing coating formulation.

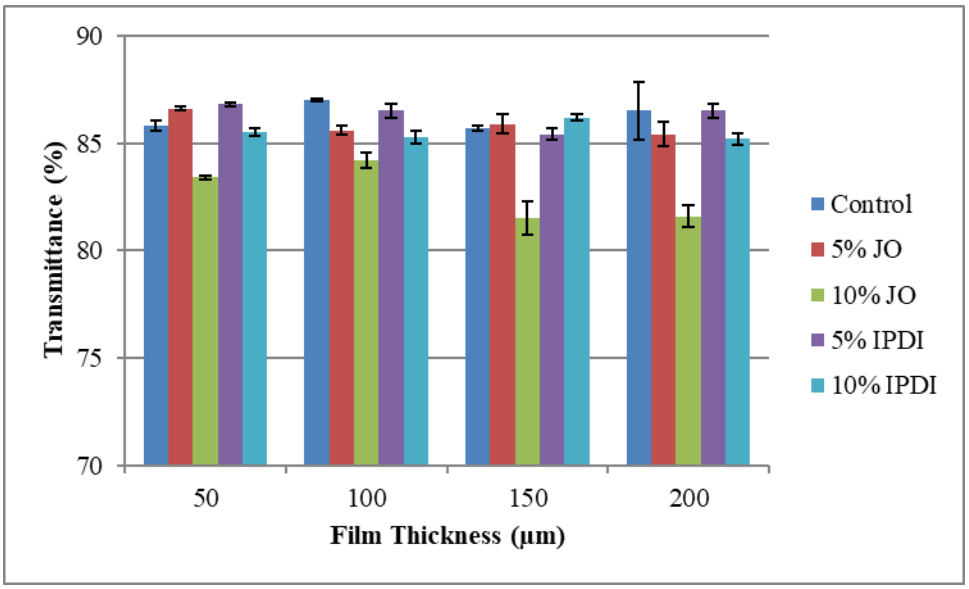

Figure 2 Transmittance value for jatropha oil-based self-healing coating with different thicknesses and concentrations of microcapsules

Haze Test

To examine the clarity of the film, a haze test was conducted. Figure 3 presents the haze property of self-healing coating containing microcapsules at different film thicknesses. The haze value increased as the film thickness increased in the for Control, 5% JO, 10% JO, 5% IPDI and 10% IPDI. Moreover, the increasing trend of haze was also observed with the increasing percentage of the microcapsule loading. This indicated that the higher film thickness and increasing number of microcapsules may cause poor dispersion in the coating formulation and led to surface roughness of the coating. The surface roughness is linked with poor haze (Adachi et al., 2018). Therefore, incorporating microcapsules is unsuitable for coating applications requiring transparent and clear surfaces such as glass, windows, and windscreens.

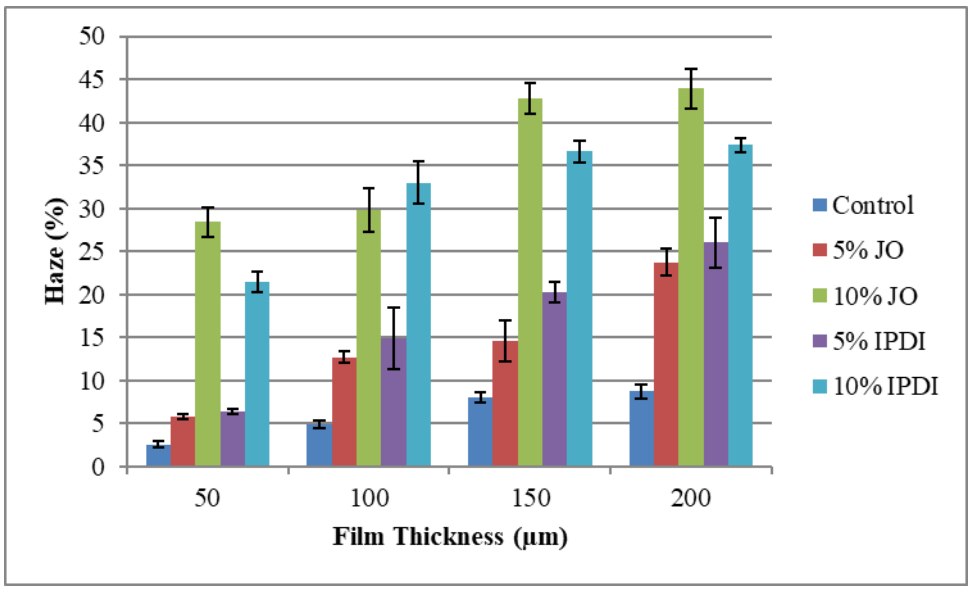

Figure 3 Haze property for jatropha oil-based self-healing coating at different film thicknesses and microcapsule loading

Morphology Observation

Considering all the mechanical tests that have been conducted, 5% JO and 5% IPDI with a thickness of 50 µm were selected to be evaluated for the self-healing test via scratch test in the future work. Figure 4 shows the overview of 5% JO and 5% IPDI coating with a thickness of 50 µm under an optical microscope at a magnification of 10x. It was found that both 5% JO and 5% IPDI coating have well-distributed microcapsule loading after being cured under UV light.

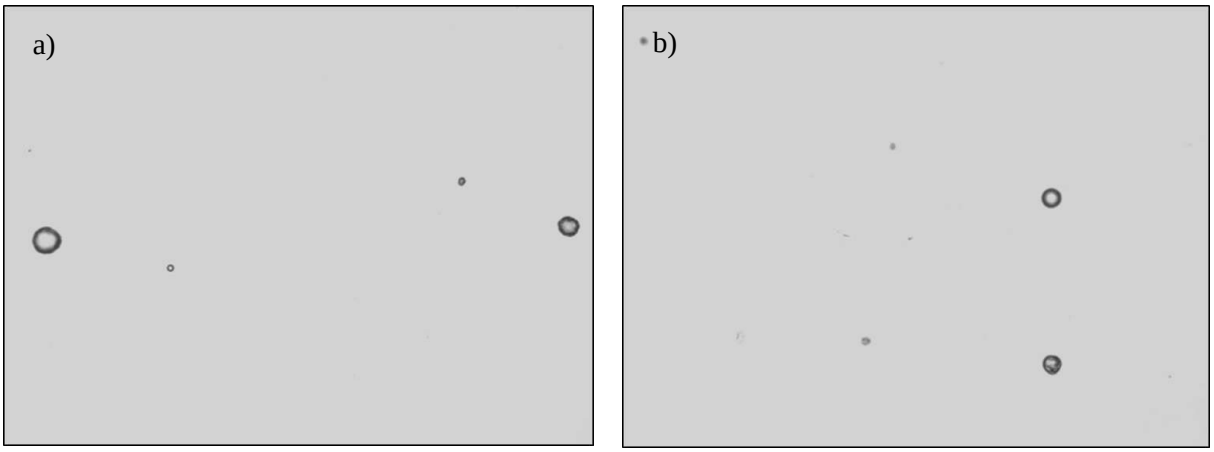

Figure 4 Optical micrograph of microcapsules distribution of a) 5% JO and b) 5% JPUA-IPDI at film thickness of 50 µm at 10x magnification after exposure to UV light

The observation was then zoomed in to 40x magnification to view the microcapsule morphology after being irradiated under UV light subjected to the curing process of the coating. From Figure 5, the microcapsules of both 5% JO and 5% IPDI were still intact, where no sign of PUF shell rupturing was detected when the microcapsule was irradiated under UV light. The thick and dark area was identified as the PUF shell whilst the core content was in the middle of the sphere with a light colour. This concluded that UV-curing technique is a suitable to be use for preparation of self-healing coating without any sign of damage on the microcapsule in the coating matrix.

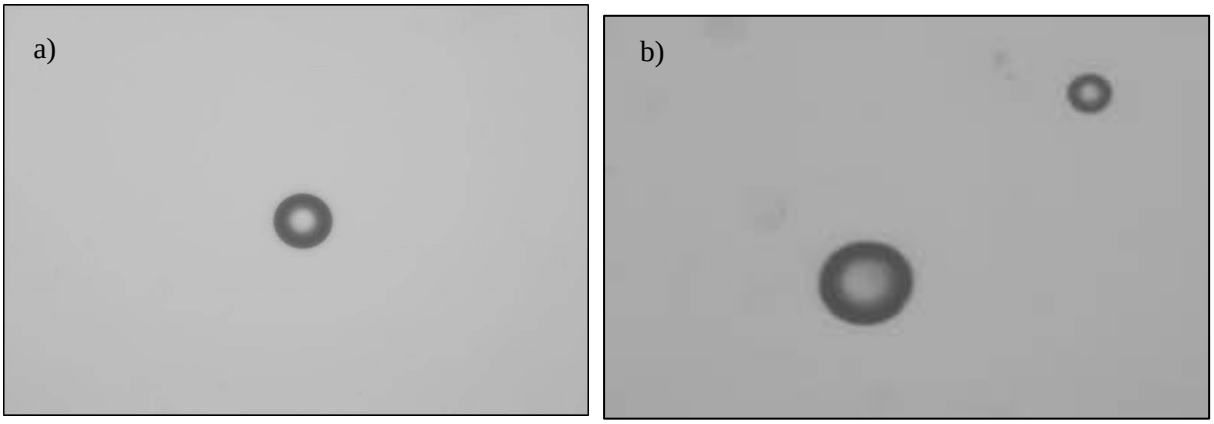

Figure 5 a) 5% JO and **b)** 5% IPDI under 40x magnification of an optical microscope after exposure to UV light at film thickness of 50 µm.

CONCLUSION

The addition of microcapsule loading and increasing coating thickness has declined the mechanical properties of the self-healing coating. The jatropha oil-based self-healing coating maintained their mechanical properties limited to 5 wt% microcapsule loading with film thickness of 50 µm when compared to the control sample. Under optical microscope, the 5% JO and 5% IPDI maintained spherical shape of the microcapsule after exposed to UV light prior to curing process where no sign of destruction was observed. A few recommendations are suggested for way forward to improve the mechanical properties such as (1) to study the microcapsule loading at below 5 wt%; (2) to prepare nano-size microcapsule; and (3) to examine the compatibility of the PUF microcapsule with epoxy-based coating.

ACKNOWLEDGEMENT

This project was funded by the Fundamental Research Grant Scheme (FRGS/1/2018/STG01/MOSTI/02/1) awarded by Malaysian Ministry of Higher Education (KPT). The authors also acknowledge the Department of Public Service (JPA), Malaysia for the scholarship to complete this work.

REFERENCES

Adachi, T., Latthe, S. S., Gosavi, S. W., Roy, N., Suzuki, N., Ikari, H., Kato, K., Katsumata, K. ichi, Nakata, K., Furudate, M., Inoue, T., Kondo, T., Yuasa, M., Fujishima, A., & Terashima, C. (2018). Photocatalytic, superhydrophilic, self-cleaning TiO 2 coating on cheap, light-weight, flexible polycarbonate substrates. *Applied Surface Science*, *458*(July), 917–923. https://doi.org/10.1016/j.apsusc.2018.07.172

Alizadegan, F., Mirabedini, S. M., Pazokifard, S., Goharshenas Moghadam, S., & Farnood, R. (2018). Improving self-healing performance of polyurethane coatings using PU microcapsules containing bulky-IPDI-BA and nano-clay. *Progress in Organic Coatings*, *123*, 350–361. https://doi.org/10.1016/j.porgcoat.2018.07.024

Amri, M. R., Al-Edrus, S. S. O., Guan, C. T., Yasin, F. M., & Hua, L. S. (2021). Jatropha Oil as a Substituent for Palm Oil in Biobased Polyurethane. *International Journal of Polymer Science*, *2021*(3), 1–12. https://doi.org/10.1155/2021/6655936

Ataei, S., Khorasani, S. N., & Neisiany, R. E. (2019). Biofriendly vegetable oil healing agents used for developing self-healing coatings: A review. In *Progress in Organic Coatings* (Vol. 129, Issue January, pp. 77–95). Elsevier. https://doi.org/10.1016/j.porgcoat.2019.01.012

Baharom, Z., Abdullah, H. Z., Idris, M. I., & Ismail, Z. M. M. (2023). High linoleic waste sunflower oil: A distinctive recycled source of self-healing agent for smart metal coatings. *Heliyon*, *9*(4), e15364. https://doi.org/10.1016/j.heliyon.2023.e15364

Cheng, M., Fu, Q., Tan, B., Ma, Y., Fang, L., Lu, C., & Xu, Z. (2022). Build a bridge from polymeric structure design to engineering application of self-healing coatings: A review. *Progress in Organic Coatings*, *167*, 106790. https://doi.org/10.1016/j.porgcoat.2022.106790

Chen, K., Zhou, J., Ge, F., Zhao, R., & Wang, C. (2019). Smart UV-curable fabric coatings with self-healing ability for durable self-cleaning and intelligent oil/water separation. *Colloids and Surfaces A: Physicochemical and Engineering Aspects*, *565*(October 2018), 86–96. https://doi.org/10.1016/j.colsurfa.2019.01.003

Fu, J., Yu, H., Wang, L., Liang, R., Zhang, C., & Jin, M. (2021). Preparation and properties of UV-curable polyurethane acrylate / SiO2 composite hard coatings. *Progress in Organic Coatings*, *153*. https://doi.org/10.1016/j.porgcoat.2020.106121

Jiang, S., Lin, Z., Tang, C., & Hao, W. (2021). Preparation and mechanical properties of microcapsule-based self-healing cementitious composites. *Materials*, *14*(17). https://doi.org/10.3390/ma14174866

Karami, Z., Zohuriaan-Mehr, M. J., Kabiri, K., & Ghasemi Rad, N. (2019). Bio-based thermoset alloys from epoxy acrylate, sesame oil- and castor oil-derived resins: Renewable alternatives to vinyl ester and unsaturated polyester resins. *Polymers from Renewable Resources*, *10*(1–3), 27–44. https://doi.org/10.1177/2041247919863633

Khorasani, S. N., Ataei, S., & Neisiany, R. E. (2017). Microencapsulation of a coconut oil-based alkyd resin into poly(melamine–urea–formaldehyde) as shell for self-healing purposes. *Progress in Organic Coatings*, *111*, 99–106. https://doi.org/10.1016/j.porgcoat.2017.05.014

Kothari, J., & Iroh, J. O. (2023). Self-Healing Poly (urea formaldehyde) Microcapsules: Synthesis and Characterization. *Polymers*, *15*(1668), 1–26.

Kurt Çömlekçi, G., & Ulutan, S. (2018). Encapsulation of linseed oil and linseed oil based alkyd resin by urea formaldehyde shell for self-healing systems. *Progress in Organic Coatings*, *121*(October 2017), 190–200. https://doi.org/10.1016/j.porgcoat.2018.04.027

Li, H., Cui, Y., Li, Z., Zhu, Y., & Wang, H. (2018). Fabrication of microcapsules containing dual-functional tung oil and properties suitable for self-healing and self-lubricating coatings. *Progress in Organic Coatings*, *115*, 164–171. https://doi.org/10.1016/j.porgcoat.2017.11.019

Liu, T., Ma, L., Wang, X., Wang, J., Qian, H., Zhang, D., & Li, X. (2021). Self-healing corrosion protective coatings based on micro/nanocarriers: A review. *Corrosion Communications*, *1*, 18–25. https://doi.org/10.1016/j.corcom.2021.05.004

Mudri, N. H., Abdullah, L. C., Aung, M. M., Biak, D. R. A., & Tajau, R. (2021). Structural and rheological properties of nonedible vegetable oil-based resin. *Polymers*, *13*(2490), 1–19. https://doi.org/10.3390/polym13152490

Mudri, N. H., Abdullah, L. C., Aung, M. M., Salleh, M. Z., Awang Biak, D. R., & Rayung, M. (2020). Comparative Study of Aromatic and Cycloaliphatic Isocyanate Effects on Physico-Chemical Properties of Bio-Based Polyurethane Acrylate Coatings. *Polymers*, *12*(7), 1494.

https://doi.org/10.3390/polym12071494

Ouarga, A., Lebaz, N., Tarhini, M., Noukrati, H., Barroug, A., Elaissari, A., & Ben Youcef, H. (2022). Towards smart self-healing coatings: Advances in micro/nano-encapsulation processes as carriers for anti-corrosion coatings development. *Journal of Molecular Liquids*, *354*, 118862. https://doi.org/10.1016/j.molliq.2022.118862

Paquet, C., Schmitt, T., Sapieha, J. E. K., Morin, J. F., & Landry, V. (2020). Self-healing UV curable acrylate coatings for wood on self-healing efficiency. *Coatings*, *10*(8), 770.

Pongmuksuwan, P., Jangmee, T., & Kitisatorn, W. (2023). Microencapsulated epoxidized palm oil: A self-healing coating solution. *Applied Surface Science Advances*, *18*. https://doi.org/10.1016/j.apsadv.2023.100458

Saman, N. M., Ang, D. T. C., Shahabudin, N., Gan, S. N., & Basirun, W. J. (2018). UV-curable alkyd coating with self-healing ability. *Journal of Coatings Technology and Research*. https://doi.org/10.1007/s11998-018-0124-x

Shisode, P. S., Patil, C. B., & Mahulikar, P. P. (2018). Preparation and characterization of microcapsules containing soybean oil and their application in self-healing anticorrosive coatings. *Polymer-Plastics Technology and Engineering*, *57*(13), 1334–1343. https://doi.org/10.1080/03602559.2017.1381248

Song, Y. K., Kim, H. W., & Chung, C. M. (2022). Repeatable Self-Healing of a Protective Coating Based on Vegetable-Oil-Loaded Microcapsules. *Polymers*, *14*(10), 2–4. https://doi.org/10.3390/polym14102013

Wang, H., & Zhou, Q. (2018). Evaluation and failure analysis of linseed oil encapsulated self-healing anticorrosive coating. *Progress in Organic Coatings*, *118*(January), 108–115. https://doi.org/10.1016/j.porgcoat.2018.01.024

Wang, Y., Liu, Q., Li, J., Ling, L., Zhang, G., Sun, R., & Wong, C. P. (2019). UV-triggered self-healing polyurethane with enhanced stretchability and elasticity. *Polymer*, *172*(November 2018), 187–195. https://doi.org/10.1016/j.polymer.2019.03.045

Wu, Q., Li, W., & Yan, X. (2023). Effect of Microcapsules on Mechanical, Optical, Self-Healing and Electromagnetic Wave Absorption in Waterborne Wood Paint Coatings. *Coatings*, *13*(9), 1478. https://doi.org/10.3390/coatings13091478